Analyzing Engineered Nanoparticles using Photothermal Infrared Spectroscopy

Yamada, Shoko

Publication date:
2016

Document Version
Publisher's PDF, also known as Version of record

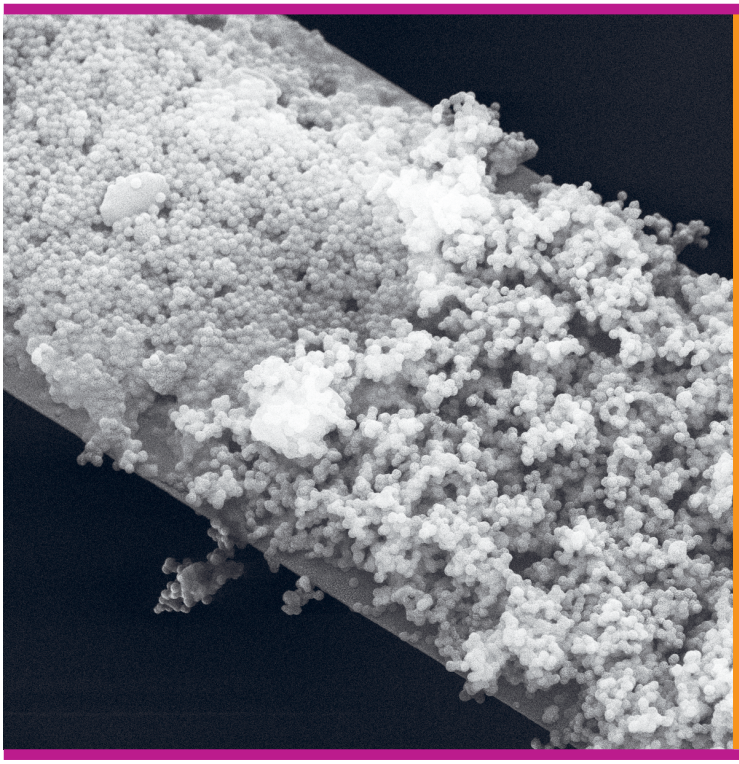

Analyzing Engineered Nanoparticles Using Photothermal Infrared Spectroscopy

Shoko Yamada
PhD Thesis February 2016

DTU Nanotech
Department of Micro- and Nanotechnology

Analyzing Engineered Nanoparticles Using Photothermal Infrared Spectroscopy

Shoko Yamada
Ph.D. Thesis

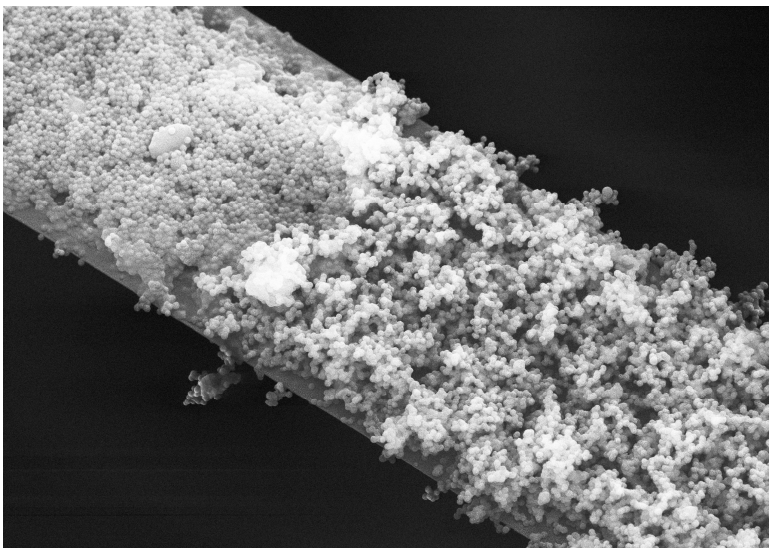

February 2016

Department of Micro- and Nanotechnology
Technical University of Denmark
Ørsteds Plads
Building 345B
2800 Kgs. Lyngby
DENMARK

Preface

This Ph.D. thesis was written as a partial fulfillment of the requirements for obtaining the Ph.D. degree at the Technical University of Denmark (DTU). The work has been carried out at the Department of Micro- and Nanotechnology (DTU Nanotech) during the period from the 1st of April 2010 to the 10th of February 2016, including 34 months of leave.

This Ph.D. project has been carried out in the Nanoprobes group at DTU Nanotech and supervised by Professor Anja Boisen and co-supervised by Associate Professor Silvan Schmid.

This Ph.D. project is a part of NANODEVICE, European Community's Seventh Framework Programme which has been financed by the European Commission.

Acknowledgements

Firstly I would like to thank my supervisors: Professor and the group leader Anja Boisen for giving me the opportunity to do a Ph.D. project in the Nanoprobes group. You have been a great supervisor offering endless support, guidance and patience throughout the project. It has been a honour to work with you, such a cheerful woman. Associate Professor Silvan Schmid for your valuable help in all aspects of the project. Your ideas and support have been of great importance for the project.

I would like to thank all the people that have been a member of the Nanoprobes group during the many years. It has been very inspiring to work together with all you talented people from all over the world. A special thanks goes to Lee Mackenzie Fischer for your great help in the electrochemical sensor part, to Tom Larsen for your infinite help with a high quality of pedagogy, fruitful discussion on my project even after you left DTU Nanotech, and for being my wonderful officemate, to Xueling Quan for the interesting discussion on electrochemistry and metformin and for being my marvellous officemate, to Sanjukta Bose for the hot discussion on polymer, to Ritika Singh Petersen for helping me with polymer processing, to Kasper Bayer Frøhling for the surface functionalisation of the gold coated strings, to Alina Joukainen Andersen for the discussion on the experimental details, and to Rikke Kragh Lauridsen for being a great companion.

I would like to thank Assistant Professor Seonghwan Kim at University of Calgary, Professor Thomas Thundat at University of Alberta, and Senior Researcher Kent Mattsson at DTU Fotnik for the help with the photothermal IR setup. I would like to thank Professor Ole Hansen for your help with the analytical model. I would like to thank the Senior Scientist Sønnik Clausen at Technical University of Denmark in Risø for helping me with the calibration of the thermal IR source.

Being a part of the NANODEVICE project has been a great experience for me and I would like to thank all the people that have been a part of it. A special thanks goes to Professor Ulla Vogel and Senior Researcher Keld Alstrup Jensen at the National Research Centre for the Working Environment. I learned a lot about nanoparticles, environment and health from you, and also thank you for providing the nanoparticle samples.

The experimental results presented in this Ph.D. thesis could not have

been achieved without the chips fabricated in the cleanroom at DTU Danchip. I would like to thank all the people at DTU Danchip for their help and support. A special thanks goes to Søren M.B. Petersen for the long discussion on the design of the vacuum chambers and also for machining them, to Jonas Michael Lindhard for the help with the ICP etcher, to Conny Hjort, Helle Vendelbo Jensen and Louise Jørgensen for the advices regarding wet chemistry, and to Jens H. Hemmingsen for helping me with the electrical part of the experimental setups.

Finally I would like to thank all my friends and family members who have also helped, supported and encouraged me throughout my Ph.D. project.

Abstract

Nanoparticles, particles having one or more dimensions smaller than 100 nm, show novel properties and functions that differ significantly from those of their corresponding bulk counterpart. Due to their small size and large surface to volume ratio they can e.g. diffuse easily and be highly reactive. To facilitate occupational safety and health there is a need to develop instruments to monitor and analyze nanoparticles in the industry, research and urban environments. The aim of this Ph.D. project was to develop new sensors that can analyze engineered nanoparticles. Two sensors were studied: (i) a miniaturized toxicity sensor based on electrochemistry and (ii) a photothermal spectrometer based on tensile-stressed mechanical resonators (string resonators).

Miniaturization of toxicity sensor targeting engineered nanoparticles was explored. This concept was based on the results of the biodurability test using redox activity measurements. With a new setup adapted to miniaturization, stable pH was achieved, platinum was found to be more suitable than gold for open circuit potential-time measurements, miniaturized platinum working electrodes and quasi silver/silver chloride reference electrodes were fabricated, and Gambles solution with dispersed iron oxide nanoparticles showed lowered potential as expected. Despite the potential of this concept instability and lack of reproducibility continued to be an unneglectable issue.

The concept of utilizing string resonators for photothermal spectroscopy was, for the first time, studied in details both theoretically and experimentally. The string-based photothermal spectrometer consists of a string resonator on which an analyte is collected. Wavelength-dependent absorption by the analyte leads to heating of the string which is reflected in its resonance frequency. This setup allows for spectroscopic measurement of the analyte. An analytical model describing the resonance frequency of a string resonator locally heated was developed. The developed model was in agreement with FEM simulations and experimental results. Theoretical and experimental work lead to a set of design rules for the responsivity of the string-based photothermal spectrometer. Responsivity is maximized for a thin, narrow and long string irradiated by high power radiation.

Various types of nanoparticles and binary mixtures of them were successfully detected and analyzed. Detection of copper-chelation of the anti-

diabetic drug metformin was demonstrated as well. The estimated detection limit for the developed system is an analyte with a mass of ∼150 ag (1 ag = 10^{-18} g). In short, it has been demonstrated that the string-based photothermal spectrometer is a promising technique for nanoparticle detection and analysis.

Dansk Resumé

Nanopartikler, partikler med en eller flere dimensioner der er mindre end 100 nm, har unikke egenskaber, der adskiller sig væsentligt fra deres makroskopiske modstykke. På grund af deres lille størrelse og den store overflade i forhold til volumen kan de bl.a. diffundere let og være yderst kemisk reaktive. For at minimere sundhedsrisikoen fra nanopartikler, er det nødvendigt at udvikle instrumenter til at overvåge og analysere nanopartikler i industri-, forsknings- og urbane miljøer. Dette Ph.D. projekt havde til formål at udvikle nye sensorer til detektering og analysering af nanopartikler. Følgende to sensorer er blevet undersøgt: (i) en miniaturiseret toksicitetssensor baseret på elektrokemi, og (ii) et fototermisk spektrometer baseret på forspændte mikro-mekaniske resonatorer (strenge-resonatorer).

Den miniaturiserede toksicitetssensor er baseret på resultaterne af en såkaldt biodurability test, hvor redox-aktivitetsmålinger giver et mål for skadeligheden af en given type nanopartikler. Med et nyt setup tilpasset miniaturisering blev der opnået stabil pH, platin som elektrodemateriale blev fastslået til at være bedst egnet til tidsafhængige potentialemålinger i åbent-kredsløb konfiguration, miniaturiserede arbejdselektroder af platin og referenceelektroder af kvasi-sølv/sølvklorid blev fremstillet, og Gambles opløsning med iblandet jernoxid-nanopartikler viste reduceret potentiale som forventet. Til trods for potentialet af denne sensor, var ustabilitet og manglende reproducerbarhed et tilbagevendende problem.

Konceptet med at udnytte mekaniske strenge til fototermisk spektroskopi er her, for første gang, blevet undersøgt i detaljer både teoretisk og eksperimentelt. Det strenge-baserede fototermiske spektrometer består af en vibrerende streng hvorpå en prøve af nanopartikler er indsamlet. Absorption af lys, med specifik bølgelængde, i prøven fører til opvarmning af strengen hvilket medfører en ændring i strengens resonansfrekvens. Dette setup tillader spektroskopiske målinger af den prøve. En analytisk model, som beskriver resonansfrekvensen af en streng som bliver opvarmet lokalt, er blevet udviklet. Denne model stemmer overens med både FEM simuleringer og eksperimentelle resultater. Teoretiske og eksperimentelle resultater har ført til et sæt af designregler for responsiviteten af det strenge-baserede fototermiske spektrometer. Responsiviteten er maksimal for en tynd, smal og lang streng bestrålet med lys af høj effekt.

Forskellige typer af nanopartikler og binære blandinger af disse er blevet detekteret og analyseret med succes. Påvisning af kobber-chelat af det antidiabetiske lægemiddel metformin er også blevet detekteret. Den anslåede detektionsgrænse for det udviklede system er en prøve med en masse på $\sim$150 ag (1 ag = 10^{-18} g). Samlet set er det blevet påvist, at det strengebaserede fototermiske spektrometer er et lovende setup til detektion og analyse af nanopartikler.

Contents

Chapter 1

NANODEVICE Project

This Ph.D. project is a part of NANODEVICE project which has been financed by the European Community's Seventh Framework Programme. The NANODEVICE project ran from 2009 to 2013 and it had 26 partners. The aim of NANODEVICE is to develop novel concepts, methods, and technologies for the production of portable, easy-to-use devices for the measurement and analysis of airborne engineered nanoparticles in workplace air. Due to the increasing use of engineered nanoparticles in many different applications and also due to the industries' awareness in the potential toxicity of nanoparticles, instruments are needed to monitor emission and release of nanoparticles at workplaces. Such instruments could for example prevent the employees from inhaling harmful nanoparticles that are invisible to human eyes. The existing instruments measure only number and size of nanoparticles and they are not capable of analysing the composition. It is necessary to develop new technologies and new devices for online analysis of the composition of airborne nanoparticles to judge if the nanoparticles are harmful.

Particles that have at least one dimension smaller than 100 nm are defined as nanoparticles. Objects at nano scale, take on novel properties and functions that differ markedly from those seen in the corresponding bulk counterpart, primarily because of their small size and large surface area. For example, titanium dioxide (TiO_2) is used as white pigment in many industrial products like paint, plastic, paper, food, toothpaste, cosmetics and skin care products. As sunscreen, TiO_2 protects the skin from UV radiation. Studies have, however, revealed that the same properties that make nanoparticles so unique could also be responsible for their potential toxicity. The amount of engineered nanoparticles is increasing at a rapid rate and the uptake of airborne nanoparticles by inhalation is a major exposure scenario [1, 2]. Instruments are needed to monitor emission and release of nanoparticles in workplaces to facilitate occupational safety and health.

For the same mass of particles with the same chemical composition and

crystalline structure, a greater toxicity was found from nanoparticles than from their larger counterparts. This led to the conclusion that the inflammatory effect may be dependent on the surface area of nanoparticles, suggesting a need for changes in definitions and regulations related to dose and exposure limits [3, 4]. Smaller nanoparticles have a higher surface area and a higher particle number per unit mass compared to larger particles. The body would react differently to the same mass dose consisting of billions of nanoparticles compared to microparticles. Larger surface area leads to increased reactivity and is an increased source of reactive oxygen species, as demonstrated by in vitro experiments [5].

There are many research groups that study toxicity of engieered nanoparticles. On the industry side, there are players to develop devices to measure and to analyze nanoparticles. The nanotoxicologists are lobbying towards setting exposure limits separately for nanoparticles from bulk materials and there will be at least recommendations and perhaps regulations for nanoparticle exposure and measurements in the future on the EU level. There are also desires from the industry side to have safer working places by measuring nanoparticles [6].

This Ph.D. project belongs to the device development part of the NANODEVICE project which aims at developing technologies in miniaturized and field-worthy specific monitors for engineered nanoparticles. Micro- and nanomechanical sensors have been chosen at DTU Nanotech for the device development for their high sensitivity. Silvan Schmid has developed the sensor for mass spectrometry, which is based on changes in resonance frequency of a mechanical string resonator due to an added mass. Two types of sensors/monitoring methods have been investigated in this thesis: One is based on electrochemistry to monitor the toxicity of nanoparticles and the other is based on photothermal spectroscopy with mechanical string resonators that rely on thermally generated stress in the strings. The goal of this project is to develop new sensors that distinguish nanoparticles of different materials.

1.1 Outline

The aim of this Ph.D. project has been to develop sensors to analyze engineered nanoparticles in the air. Initially, it was focused on electrochemical sensors based on the macroscale study of "Biodurability test of the redox activity and the particle size" for the purpose to investigate the biological solubility of particles in extracellular lung fluid, Gamble's slution. The goal was to develop miniaturized sensors for the same purpose.

Then the idea of a completely new type of sensor arose: The string-based photothermal IR spectrosocpy to analyze engineered nanoparticles in the air. This sensor type is based on temperature induced changes in the resonance frequency of a pre-stressed doubly clamped beam. The dynamic behaviour

of the beam is considered string-like because of the tensile stress in it. The resonance frequency changes as a function of absorbed power because the string expands when heated .

It was decided to move the focus from the electrochemical sensors to the string-based photothermal spectroscopy because the concept looked promising. This means that the majority of the Ph.D. thesis is used to describe the theory, fabrication, design, characterization and application of string-based photothermal spectroscopy.

Chapter 1: Introduction to the NANODEVICE project is described.

Chapter 2: The theory describing the working principle of electrochemical sensors to analyze nanoparticles in the air is presented. The theory is used to miniaturize the macroscale experimental setup, that are then fabricated and characterized.

Chapter 3: Introduction to infrared spectroscopy is described. Then previous researches on general photothermal specrtoscopy, on phototehrmal cantilever deflection spectroscopy and on micro- and nanomechanical string resonators are presented.

Chapter 4: The general string theory describing the free vibration of undamped beams is presented. The chapter is continued to deduce an expression for the photothermal frequency resoponse of a string from the equation of motion for an undamped beam. Then the principle of photothermal IR spectroscopy with mechanical string resonators is presented. The last part of the chapter is used to describe the general theory of infrared spectroscopy.

Chapter 5: The fabrication of string resonators is described in this chapter. This includes considerations regarding selection of string materials and the design of the fabrication processes.

Chapter 6: A number of different experimental setups used in the various measurements are described in this chapter. This includes resonance frequency measurements, frequency actuation, photothermal infrared setups, an aerosol sampling setup and used chemicals, FTIR and a power measurement QCL.

Chapter 7: The results obtained when investigating the two types of IR sources, the strings fabricated with two materials, and photothermal IR spectroscopy for a variety of applications are presented in this chapter. Firstly, the thermal IR source and the QCLs are characterised. Then the effect of changing string dimensions and absorbed power is investigated via FEM simulations and experimentally. Thermal relaxation in strings, response time of strings, and frequency stability

are also discussed. Lastly IR spectra of silicon nitride, PVP, titanium dioxide nanoparticles, metformin, and binary mixtures of PS and PVP measured by photothermal spectrosocpy are presented.

Chapter 8: This chapter contains the conclusions drawn from the findings during this Ph.D. project.

Chapter 9: The outlook for future work is described.

A number of appendices are given in the end of the thesis. Appendix A includes detailed process sequences for the fabrication of the different structures used during this Ph.D. project. Appendix B includes dimensions of the vacuum chamber built and used for the experiments. A Matlab script used for calculating the Allan deviation from frequency stability measurements is presented in Appendix C. Matlab scripts used for extracting IR spectra from raw measurement data are presented in Appendix D. A Matlab script used for normalizing IR spectra with respect to IR power is presented in Appendix E. Appendix F includes protocol for estradiol thiol-aptamer functionalisation presented in Outlook chapter. A list of projects supervised and a list of publications made during this Ph.D. project are given in Appendices G and H. Appendix I includes the published paper: Photothermal Infrared Spectroscopy of Airborne Samples with Mechanical String Resonators and Appendix J includes the submitted manuscript: Nanomechanical IR Spectroscopy for Fast Analysis of Liquid-Dispersed Engineered Nanomaterials.

Part I

Electrochemical Sensor

Chapter 2

Toxicity Sensor for Engineered Nanoparticles

2.1 Introduction

Research and product developments in the area of nanotechnology have steadily increased especially due to new, beneficial properties of nanomaterials. Nanotechnology nowadays used in electrical devices, in construction and composite materials, as catalysts and as antibacterial coatings, is more and more present in workplaces as well as consumer products. This steady increase is accompanied with larger production, handling and processing facilities for nanostructured materials and higher volume of nanomaterials. As it has been pointed out in Chapter 1, the new properties and the high mobility of some nanomaterials may lead to health or environmental effects. For the workplace safety, measurement techniques have to allow sensitive and cost effective determination of airborne engineered nanomaterials [7].

The durability of engineered nanomaterials in biological systems is important for both therapeutic and diagnostic applications, as well as for unintentional exposure, due to its potential influence on the toxicity of nanomaterials. A fundamental material property that influences biopersistence is "biodurability" - the long-term chemical stability in biological compartments. For mineral fibers this biodurability is commonly assessed by measuring dissolution rates in macrophage cultures [8]. Wiesinski et al performed biodurability tests of engineered nanoparticles in gastrointestinal fluids and found that removal of the polyethylene glycol (PEG) ligand diminished the stability of PEG350-quantum dot suspensions, while PEG5000-quantum dots were severely degraded [9].

Numerous in vitro studies report that engineered nanoparticles cause oxidative stress-mediated toxicity in diverse cell types, including liver [10], alveolar macrophages [11], and *Salmonella* bacteria [12]. When potentially damaging stimuli such as nanoparticles enter a cell, the plasma membrane

of the phagocyte surrounds the foreign substance and a multicomponent enzyme system known as NADPHox is activated. This activation results in the immediate production of superoxide anions which convert to multiple reactive oxygen species including hydrogen peroxide, hydroxyl radicals, and peroxynitrites that can destroy the offending stimuli through oxydative stress pathways [13]. Superoxide anions can be directly toxic and especially in the presence of transition metals, most notably ferrous iron, superoxides can convert to the highly reactive hydroxyl radical via the Fenton reaction [13].

A partner in NANODEVICE project performed "Atmosphere- and pH-controlled batch reactor biodurability test with on-line measurement of the redox activity and the particle size" for the purpose to investigate the biological solubility of particles in extracellular lung fluid (Gamble's solution, chemicals are shown in Table 2.1). Simulated lung fluids have been used to evaluate human exposure to particulates from environmental emissions. Artificial lysosomal fluid (ALF) and Gamble's solution are used to simulate different interstitial conditions in the lung. ALF is analogous to the fluid with which inhaled particles would come into contact after phagocytosis by alveolar and interstitial macrophages in the lung. Gamble's solution represents the interstitial fluid deep within the lung [14].

In a previous study, 3.75% CO_2 and 96.25% HEPA filtered air was mixed and bubbled in the Gamble's solution. pH was adjusted to 7.4 using 7.7 M HCl. Duirng the measurement, 1 M NaOH was used for pH titration to keep the pH at 7.4. γ -Fe_2O_3 (maghemite) nanoparticles were used in the experiments as a representative of engineered nanoparticles. Redox potential of Gamble's solution with and without added nanoparticles was measured using a redox electrode and recorded. Redox potential is a measure of the affinity of a substance for electrons. The result shows a drop in the redox potential of around 20 mV in the Gamble's solution with an added 0.16 mg/ml of γ -Fe_2O_3. The voltage is expected to correlate linearly with the dose of nanoparticles at these concentrations.

Open Circuit Potential Time (OCPT) measurement is an important technique for investigating various electrochemical processes, such as corrosion of metals [15] and secondary batteries [16]. Experimental setups are usually designed to attain an equilibrium situation, where all anodic and cathodic reactions proceed at an equal finite rate. Consequently, the net current flow is zero and the voltage corresponding to this zero current is defined as the open circuit potential [17]. Shifts in OCPT result from a change in the accumulated charge on an electrode. A shift to a more negative value is therefore indicative of a process that either decreases the excess positive charge or increases the excess of negative charge on an electrode, depending on the potential of zero charge [18].

Based on the "Biodurability test with on-line measurement of the redox activity" experiment, it should be possible to detect the reactive oxygen species caused by engineered nanoparticles by OCPT measurements.

Table 2.1: Composition of the Gamble's solution.

Chemicals	Weight [g]
$MgC_{12}(H_2O)_6$	0.424
NaCl	13.2
$Na_2HPO_4(H_2O)_{12}$	0.716
$Na_2SO_4(H_2O)_{10}$	0.358
$CaCl_2$	0.044
$NaHCO_3$	5.406
Glycine	0.236
Na_3-citrate	0.306
Na_2-tartrate	0.36
Na-pyruvate	0.344
Na-lactate	0.583
Milli-Q water	2000
Formaldehyde 4 %	

In order to develop a portable sensor to measure the toxicity of engineered nanoparticles, electrochmical measurement setups have been investigated concerning a miniaturization.

2.2 Experimental

A representative of the interstitial fluid of the deep lung, Gamble's solution, was employed to investigate the stability of different electrodes and then to characterize the redox activity between the Gamble's solution and engineered nanoparticles. Gamble's solution was prepared according to Table 2.1 and was kept in a refrigerator.

Open Circuit Potential is a technique that measures the potential difference between a working electrode and a reference electrode. A potential change would be observed when there is redox activity between nanoparticles and Gamble's solution which is designed to resemble conditions in the lung fluids. OCPT measurements were performed using electrochemical analyzers (CH Instruments, CHI660C and CHI1030) and an electrochemical

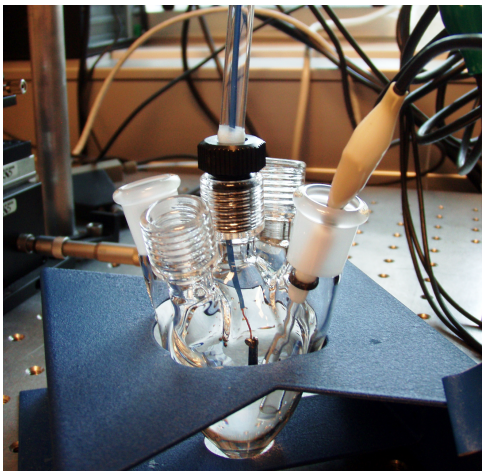

Figure 2.1: Electrochemical cell with a commercial Ag/AgCl reference electrode in the right inlet and a Pt chip working electrode in the center inlet.

cell from Gamry Instruments (Dr. Bob's cell) which is shown in Fig. 2.1.

2.3 Results and Discussion

2.3.1 pH Stability in Gamble's Solution

The Gamble's solution prepared according to Table 2.1 showed a pH drift from 8.6 to 9.2 during a 24 hour measurement. Constant pH and temperature are required for this OCPT measurement since pH and temperature changes would also be detected as a potential change. It is preferable to avoid bublling of CO_2 and air for the miniaturization purpose. It is also preferable to avoid titration during the measurement since it requires on-line pH measurement and automatic titration according to the measured pH value. In order to achieve a stable pH without titration during the measurement, Gamble's solution is buffered with Na_3PO_4. The pH is adjusted to 7.4 by adding NaOH. The pH of the buffered Gamble's solution increased only 0.06 over 22 hours compared to 0.6 increase in pH when not buffered as shown in Fig. 2.2. In the following experiments buffered Gamble's solution is used.

2.3.2 Working Electrodes

Regardless the size of a working electrode, gold is highly used as an electrochemically active surface on which the behaviours of chemical or biological samples are studied [19]. In electrochemical experiments, the quality of the active surface will affect the measurements. On exposure to a non-cleanroom environment the gold surface is subject to numerous ambient contaminants, affecting electrochemical effects [20]. It is for this reason that

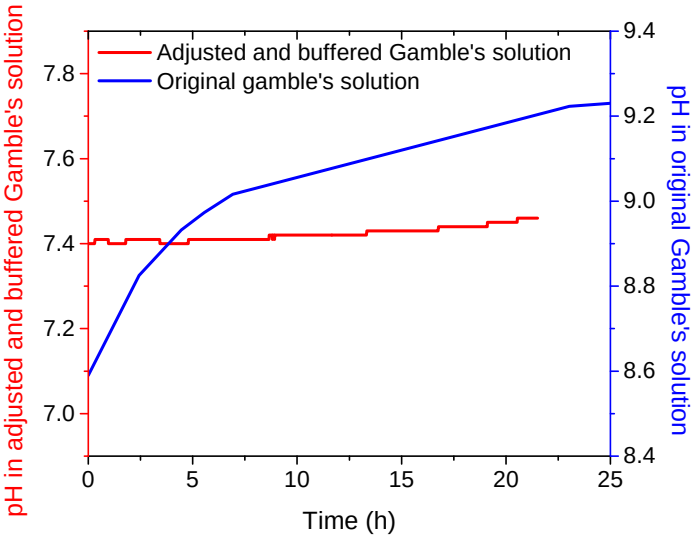

Figure 2.2: pH measurement of the original and buffered Gamble's solution showing 0.6 increase in pH for the original Gamble's solution and 0.06 increase in pH for the buffered Gamble's solution.

gold must be cleaned immediately before use. A commercial Au electrode from Metrohm was cleaned using seven different methods and also combination of those methods; polishing with Al_2O_3, being soaked in H_2O_2 + KOH for 45 minutes, being soaked in ethanol for two hours, triple pulse amperometry in 100 mM sodium phosphate buffer (pH=7.4), and potential sweep in 50 mM KOH [21, 22]. The cleanliness was evaluated by measuring cyclic voltammetry in 10 mM ferri/ferro-cyanide redox couple and 200 mM KCl (reference/counter-electrolyte) in Milli-Q water. The potential-difference between the peak cathodic and anodic currents, ΔE_P, is used as a measure of electrochemical cleanliness of the electrode surface. A smaller ΔE_P indicates a cleaner surface [21]. The combination of soaking in 100 mM KOH and 35% H_2O_2 for 8 minutes, soaking in ethanol for 2 hours and 6667 cycles of triple pulse amperometry 1.6V/0V/-0.8V (vs. Ag/AgCl) in 100 mM sodium phosphate buffer at pH 7.4 gave the cleanest Au electrode surface; however, the electrode surface was not stable enough to perform reproducible OCPT measurements for 24 hours. In order to improve the stability of the Au electrode surface, it was modified with 2-mercaptoethanol. It was, however, not stable enough to perform reproducible OCPT measurements for 24 hours, either.

It has been concluded that Au electrode is not suitable for OCPT measurements due to its instability and a commercial Pt electrode from Radiometer Analytical was investigated for OCPT measurements. The Pt electrode showed significantly higher stablity and reproducibility of OCPT measure-

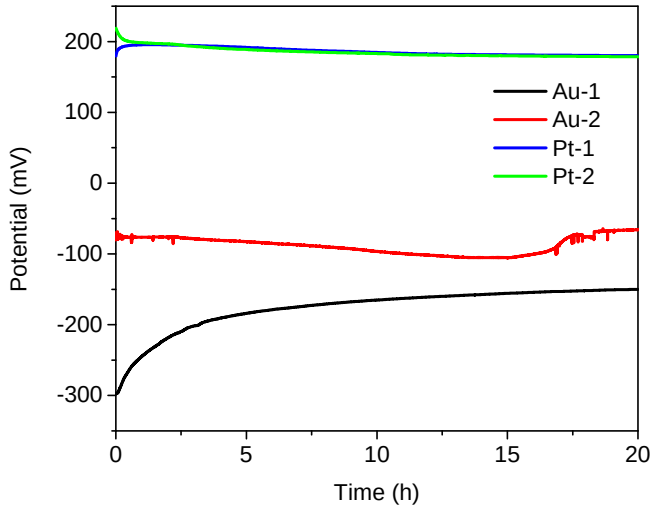

Figure 2.3: Repeated OCPT measurements in buffered Gamble's solution with a Au electrode with a thiol modification and a Pt electrode (vs. Ag/AgCl).

ments, seen in Fig. 2.3. Thus Pt has been chosen as the material for minituarized working electrodes.

Pt working electrodes were fabricated on a Si substrate using the following processes; 1) SiN deposition in a furnace, 2) Electrode mask transfer using UV lithography, 3) Pt depositon with Ti in between as an adheasion layer, 4) SiN deposition for passivation, 5) Mask transfer for the contact pad using UV lithography, and 6) SiN removal over the contact pad. Schematic drawings of the fabrication process can be seen in Fig. 2.4. A detailed process sequence can be found in Appendix A. A schematic and a photograph of a Pt working electrode are shown in Fig. 2.5. The Pt electrode is inserted in Gamble's solution and the contact pad is connected to a potentiostat. In some experiments, screen-printed disposable Pt working electrodes of DropSens were also used to obtain the maximum cleanliness and uniformity.

2.3.3 Reference Electrodes

A reference electrode should provide a stable reference potential during a series of measurements. There are many different types of reference electrodes, e.g. normal hydrogen electrode (NHE), saturated calomel electrode (SCE) and Ag/AgCl electrode. A commercial Ag/AgCl reference electrode consists of Ag and AgCl and contains KCl solution to stabilize the AgCl concentration.Depending on the concentration of KCl solution, the potential against standard hydrogen electrode (SHE) changes. For example, Ag/AgCl/Sat. KCl gives +0.197 V vs. SHE and Ag/AgCl/3.0 mol/kg KCl gives +0.210 V

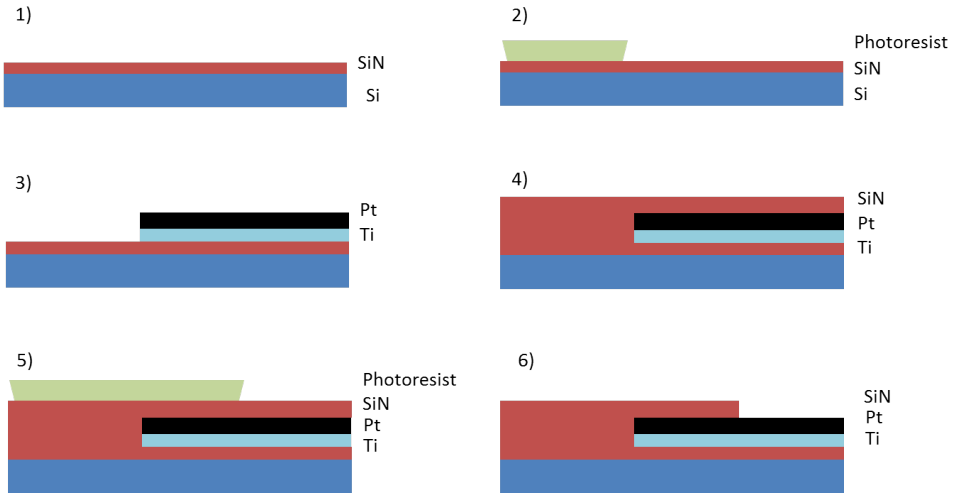

Figure 2.4: Schematic drawings of the fabrication process of Pt working electrodes. 1) SiN depositon. 2) Electrode mask transfer by UV lighography. 3) Electrode metal deposition and lift off. 4) SiN deposition for passivation coating. 5) Contact hole mask transfer by UV lighography. 6) Contact hole etching and photoresist removal.

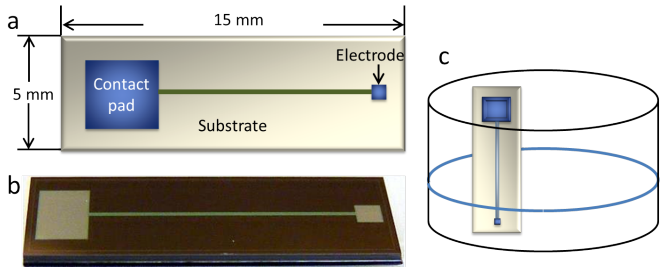

Figure 2.5: (a) Schematic top view and (b) Photograph of a Pt working electrode on a Si substrate with a sensing electrode and a contact pad. (c) The electrode is inserted in Gamble's solution and the contact pad is connected to a potentiostat.

vs. SHE. Therefore a constant concentration of Cl^- is required in the solution around the reference electrode.

In OCPT measurements, it is very important to have stable electrodes. The stability of a commercial Ag/AgCl reference electrode with saturated KCl from Gamry Instruments and a commercial Ag/AgCl reference electrode with 3 M KCl from CH Instruments were investigated. The stability of a reference electrode is dependent on the stability of the Cl^- concentration around the AgCl. The Cl^- concentration in the commercial reference electrodes seem to change during an OCPT measurement due to the length of the measurement of 24 hours. The Ag/AgCl reference electrode from Gamry Instruments has more KCl solution and thus it was more stable than the one from CH Instruments which contained less KCl solution. During the measurements with a commercial Pt working electrode against the Gamry Instruments Ag/AgCl reference electrode, the potential was lowered constantly after each OCPT measurement as seen in Fig. 2.6. To find out the reason for the constantly changing potential, the Ag/AgCl electrode from Gamry was calibrated against the master Ag/AgCl reference electrode which contains much more KCl solution than Gamry's. Gamry's Ag/AgCl reference electrode showed an increased potential against the master Ag/AgCl reference electrode. The Gamble's solution contains 0.11 M Cl^-. During an OCPT measurement, it is probable that water in the Gamble's solution was diluting the KCl solution in the reference electrode and thus the potential of the reference electrode increased. The commercial Ag/AgCl reference electrodes investigated here are thus not suitable for a 24 hour long OCPT measurement.

In Gamble's solution the concentration of Cl^-, approximatelly 0.1 M, does not change during the measurement. In theory, thus, a Ag/AgCl reference electrode without KCl solution in the electrode could also be functioning for this measurement. No KCl solution in a reference electrode makes the minituarization much simpler. In order to investigate a reference electrode without KCl solution in the electrode, quasi Ag/AgCl reference electrodes were fabricated from a Ag wire of 500 μm in diameter in our laboratory by running cyclic voltammetry between +200 mV and +1700 mV (vs. Ag/AgCl) in saturated KCl for 8 hours. The quasi Ag/AgCl electrode is shown in Fig. 2.7.

The first and the second OCPT measurements with a quasi Ag/AgCl reference electrode (black and red lines) showed a good stability as shown in Fig. 2.8. The potential, however, started drifting from the third measurement. Lifetime of smaller reference electrodes are known to be shorter and it is possible that after the second measurement, the quasi Ag/AgCl reference electrode was not functioning as it should anymore. This is still a highly promising type of reference electrode in terms of the simplicity for miniaturization since it functions for at least 48 hours in Gamble's solution.

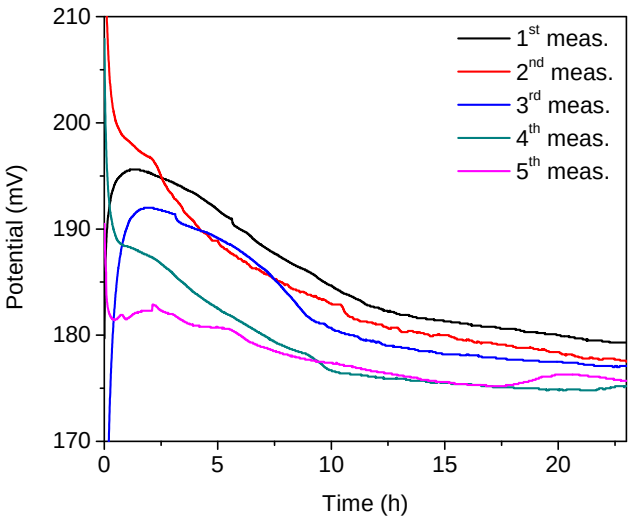

Figure 2.6: OCPT measurements in buffered Gamble's solution with a Pt working electrode against the Gamry's Ag/AgCl electrode with saturated KCl solution.

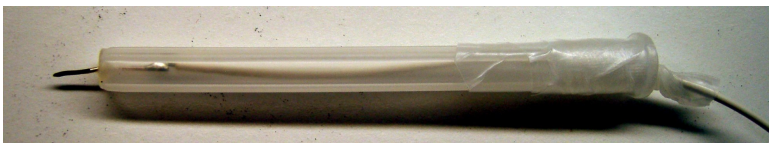

Figure 2.7: Quasi Ag/AgCl electrode fabricated from a Ag wire.

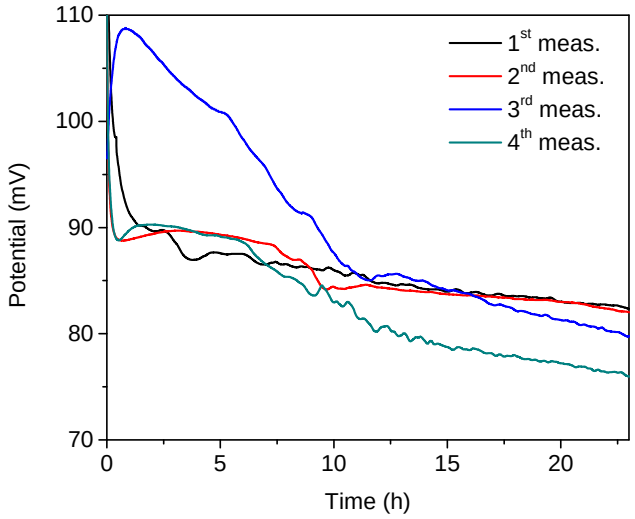

Figure 2.8: OCPT measurements in buffered Gamble's solution with Pt working electrode against self-made Ag/AgCl electrodewithout KCl.

2.3.4 Potential Response of γ-Fe_2O_3 Nanoparticles

γ -Fe_2O_3 nanoparticle powder was provided by a NANODEVICE project partner. γ -Fe_2O_3 powder was dispersed in Gamble's solution using a probe sonicator. The particle size was measured by static light scattering. It showed that the particles had a size distribution with a peak at 3 µm, that was aggregated and agglomerated forms of nanoparticles. Commercial Fe_2O_3 nanoparticles in water which was already dispersed was, thus, purchased from Sigma-Aldrich and it was used in the further experiments. The purchased nanoparticles have a diameter smaller than 100 nm according to a dynamic light scattering measurement at the manufacturer and the average particle size is smaller than 30 nm according to an aerodynamic particle sizer measurement at the manufacturer.

Dispersed Fe_2O_3 nanoparticles in water was added into Gamble's solution just before measurements started. Gamble's solution and nanoparticles were mixed and measured in an electrochemical cell from Gamry Instruments.

OCPT measurements were performed for a) Gamble's solution without nanoparticles, b) Gamble's solution with agglomerated nanoparticles with a peak size at 3 µm and c) Gamble's solution with commercially available dispersed nanoparticles (85.3 mg/ml). The measurements were compared by using a commercial Pt working electrode and Gamry's Ag/AgCl reference electrode. It was clearly seen that only the Gamble's solution with the commercial nanoparticles showed about 20 mV lower potential than the others, which agreed well with the provided result from a NANODEVICE

partner as described in Chapter 2.1. These results were, however, not reproducible. The reason could be that it was too difficult to remove all the invisible nanoparticles from the electrochemical cell. This could make it impossible to obtain the potential without nanoparticles, which is supposed to be higher than that with nanoparticles, and thus the potential drop due to added nanoparticles could not be observed.

With screen-printed disposable Pt working electrodes and also commercial disposable cells, highly stable measurements were performed together with the Ag/AgCl reference electrode of Gamry. γ -Fe_2O_3 nanoparticles dispersed in water from Sigma-Aldrich were used in this experiment. Fig. 2.9 shows the OCPT measurement results of buffered Gamble's solution with Fe_2O_3 nanoparticles (85.3 mg/ml) and blank samples without nanoparticles. Three samples were measured. The first measurement with nanoparticles showed an approximatelly 10 mV shift during the first 7 hours of the measurement. Otherwise no significant difference was observed between blank samples and samples with nanoparticles from the 24 hour OCPT measurements. It still might have shown a redox activity for the first meassurement though it was again not reproducible.

It was not possible to reproduce the redox activity measurement results from a NANODEVICE partner although very stable and clean disposable electrodes were employed for the experimental setup. The concentration of nanoparticles in the provided result from our partner was 0.16 mg/ml. This was found to be a too large amount to assume inhalation from workplace air and a person would have to intake nanoparticles intentionally to be exposed to that much amount of nanoparticles.

2.4 Conclusion

In this chapter, the possibility of miniaturization of toxicity sensor for engineered nanoparticles has been explored based on the results of the biodurability test with a redox activity measurement. First, a stable pH was achieved by buffering the Gamble's solution instead of using titration. Secondly, it was found that Pt should be used as a working electrode for OCPT measurements instead of Au and miniaturized Pt working electrodes were fabricated successfully. Thirdly, it was found that the investigated commercial Ag/AgCl reference electrodes were not suitable for 24 hour OCPT measurements and quasi Ag/AgCl reference electrodes without KCl solution were fabricated. Lastly, a Gamble's solution with dispersed Fe_2O_3 nanoparticles showed approximatelly 20 mV lower potential than the ones without nanoparticles. However the results were not reproducible even when using clean cells and electrodes.

It was thus decided to discontinue the investigation of the MEMS-based electrochemical toxicity sensor. In the following the focus will be on string-

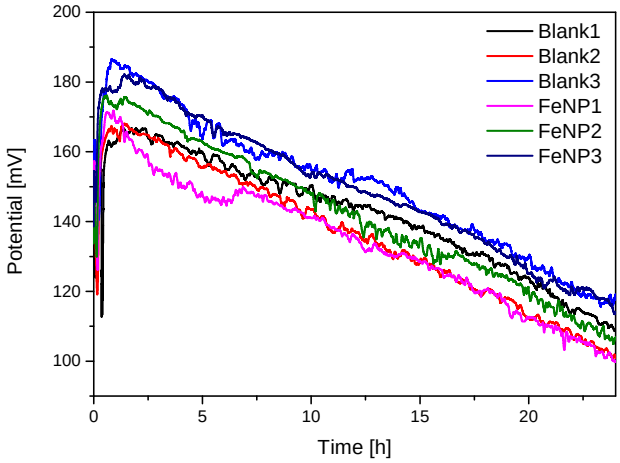

Figure 2.9: OCPT measurements in buffered Gamble's solution with disposable screen-printed Pt working electrodes and the Ag/AgCl reference electrode of Gamry. Only buffered Gamble's solution were measured for Blank 1 to 3 and buffered Gamble's solution with Fe_2O_3 nanoparticles were measured for FeNP 1 to 3 showing no significant difference between blank samples and samples with nanoparticles.

based sensors for photothermal spectroscopy.

Part II

Photothermal Spectroscopy with String Resonators

Chapter 3

Introduction

Analytical chemistry has been important since the early days of chemistry, providing methods for determining which elements and chemicals are present in the object in question. People have been amazed at the multi-colored arc of visible light that sometimes appeared after rainfalls. In 1666 Sir Isaac Newton studied the phenomenon of a prism to generate a rainbow of colors systematically and concluded that white light was actually composed of colors. The science of spectroscopy began from the Newton's experiments [23, 24]. In 1802 an English scientist, William Wollaston improved Newton's procedure and observed that the continuous line spectrum from sunlight was irregularly interrupted by a number of dark lines [25]. About a decade later a German optician, Joseph von Fraunhofer developed the spectroscope and observed over 500 dark lines in the solar spectrum [26, 27]. The first instrumental analysis was flame emission spectrometry developed by Robert Bunsen and Gustav Kirchhoff who discovered rubidium (Rb) and caesium (Cs) after observing new colored lines in the line spectra in 1861 [26].

Spectroscopy techniques offer a simple and sensitive way to analyse a sample chemically and are therefore widely used in science and industry. Chemical information is obtained by measuring a unique interaction of a sample matter with a defined emitted energy. Detection of the unique spectrum of an analyte by IR absorption spectroscopy can be a solution to the specificity problem when performing chemical analysis of increasingly smaller sample volumes.

3.1 Infrared Spectroscopy

In 1800 Sir William Herschel discovered the IR region of the electromagnetic spectrum. He detected the existence of radiant heat beyond the red portion of the spectrum in a region where no sunlight was visible using a glass prism and thermometers with blackened bulbs [23]. IR spectra of over 50 compounds were reported by Abney and Festing in 1881, that marked a

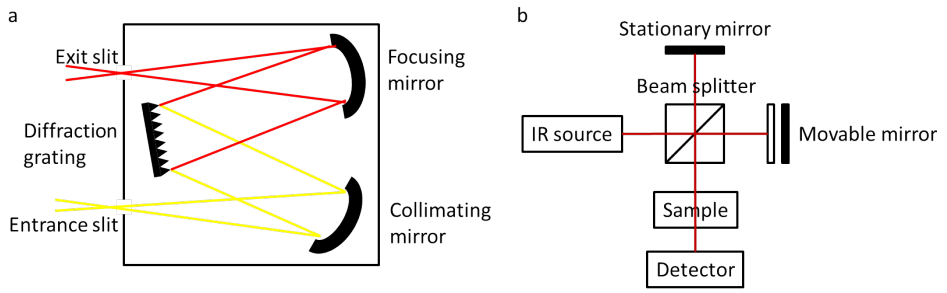

Figure 3.1: (a) Schematic of a monochromator. IR light is dispersed by a grating. (b) Schematic of a FTIR spectrometer. It is based on the interference of radiations.

start of the modern catalogue of IR spectra. They correlated absorption bands with the presence of certain functional groups in the molecules [28]. William W. Coblentz conducted comprehensive measurements that lead to the accurate IR spectra of hundreds of organic and inorganic compounds [23]. During the 1930's ,the first prototypes of IR spectrometers were built and by the 1950's IR spectroscopy was established as a major analytical method in both industry and academia.

The instrument used today to obtain IR spectra is called an IR spectrometer or a spectrophotometer. There are two types of IR spectrometers: dispersive and Fourier transform (FT) instruments. IR spectra are obtained faster with FTIR spectrometers than with dispersive instruments. A dispersive IR spectrometer is based on dispersion of light by a grating (a prism was used earlier). A simple dispersive IR spectrometer consists of an IR source, a monochromator and a detector. A typical monochromator consists of a diffraction grating, slits and spherical mirrors as shown in Fig. 3.1(a). The diffraction grating disperses light by diffracting different wavelengths at different angles and thus a particular wavelength that passes through the monochromator is selected by rotating the angle of the grating. FTIR spectrometers are based on the interference of radiations and consist of an optical system which uses an interferometer, a Michaelson interferometer is most commonly employed, and a dedicated computer. An interferogram is obtained by measuring the signal at many positions of the moving mirror as shown in Fig. 3.1(b) and the interferogram is converted into a spectrum by a Fourier transform [29].

Common IR sources are globars (silicon carbide rods), Nernst glowers (yttria-stabilized zirconia rods) and nichrome coils. Two types of detectors are used: one based on the heating effect of the radiation and the other on photoconductivity. The three main types in the first category are: thermocouple, bolometer, and Golay detector. The thermocouple produces a voltage from the thermal energy and has been used most frequently. The thermal energy causes an electrical resistance change in the bolometer which has a

short response time. In the Golay detector, which is sensitive but mechanically not robust, a rise in temperature produces a rise in pressure. Mercury cadmium telluride (MCT) is a commonly used photoconductivity cell, which has high sensitivity and quick response time in IR region. It requires a liquid nitrogen temperature for noise reduction [29–31]. The most widespread detectors in IR spectrometers are the pyroelectric detectors such as triglycine sulfate and deuterated triglycine sulfate (TGS and DTGS). Pyroelectricity is the electrical response of a polar, dielectric material to a change in temperature and it is one of the most competitive principles for uncooled IR detection [32].

There are several different types of sampling methods. Transmission spectroscopy is the oldest and simplest IR method. The method is based on the absorption of IR radiation at specific wavelengths as it passes through a sample. Attenuated total reflectance spectroscopy (ATR), which is the most widely used FTIR sampling method today, utilizes the phenomenon of total internal reflection [31].

An FTIR microscope which consisits of a FTIR spectrometer and an optical microscope can be used for mapping and imaging with focal plane array (FPA) which can speed up the data collection process. Employing synchrotron light as its IR source, a spacial resolution of 6 μm was reported [33]. A protocol for collecting IR spectra and images from biological samples has been described [34]. IR spectroscopy combined with chromatography is a common way to sort a mixture into individual components and then identify each components. An FTIR spectrometer can be combined with a thermal method such as thermogravimetric analysis (TGA) in order to analyse gaseous products evolved from a sample. In emission spectroscopy a sample is used as the IR source since a material emit IR radiation due to its temperature [35].

Identifying organic compounds is the most common application of IR spectroscopy. Inorganic materials usually have broader and fewer IR bands at lower wavenumbers than organic materials. Polymer can be investigated by IR spectroscopy to identify composition, to characterize structure, and to monitor polymerization and degradation processes [36–38]. IR spectroscopy is a powerful tool to study biological systems such as proteins, lipids, peptides, animal tissue, plants, and clinical samples [39–41]. In industry IR spectroscopy, both in the near and middle IR regions, has been extensively used in qualitative and quantitative pharmaceutical analysis [42], food analysis [43], and quality control of pulp and paper [44]. IR spectroscopy is applied to investigate cultural heritage materials [45] and also for the forensic analysis of paints [46].

In absorption spectroscopy, the energy absorbed by the sample is usually directly determined by measuring the fraction of light being transmitted through the sample. IR spectroscopy in the mid-IR region provides information on molecular vibrations that results in a sample specific absorption

spectrum, i.e., fingerprint. A minimum sample mass of 0.25 mg and additional 100 mg potassium bromide (KBr) are typically needed for preparing a micro-pellet for transmission measurements with FTIR [47].

3.2 Photothermal Spectroscopy

Photothermal spectroscopy is based on a photo-induced change in the thermal state of a sample. It is a group of highly sensitive methods to measure optical absorption and thermal characteristics of a sample [48, 49]. In 1977 Brilmyer *et al* proposed photothermal spectroscopy using a thermistor to measure the temperature change of a sample during sample irradiation with high intensity monochromatic light and the technique was evaluated with crystalline solids (cadmium sulfide and titanium dioxide) and solutions of the dyes rose bengal, methylene blue, and aniline yellow [50]. They also examined electroactive spieces and estimated the lower limit for detection was 75 - 100 monolayers with their instrumentation It was concluded that the sensitivity could be improved by instrumental changes such as more intense light sources (e.g., lasers), more sensitive thermal detectors, and light modulation or signal averaging techniques [51]. This technique is similar to photoacoustic spectroscopy where the pressure fluctuations in a gas arising from heat produced by the absorption of radiation from a modulated light beam is detected by a sensitive microphone [52] although photothermal spectroscopy allows a more flexible sample arrangement and also it is free from acoustic noise problems.

Direct spectroscopic methods measure the transmission of light used to excite a sample while indirect spectroscopic methods measure an effect that optical absorption has on a sample. Sample heating is, however, a direct consequence of optical absorption and photothermal spectroscopic signals are directly related to light absorption [48]. The amount of incident light minus the amount of tansmitted light is equal to the total amount of absorbed, scattered and reflected light in the "direct methods" and only the amount of absorbed light is measured in the "indirect methods".

The theory for a spectroscopy based on the photothermal deflection of a laser beam was developed and experimentally verified by Jackson*et al* [53]. Weaver *et al* presented the combination of scaning tunnelling microscope and photothermal spectroscopy with nanometre resolution [54]. Photothermal FT-IR spectroscopy to acquire polymer spectra was demonstrated by Hammiche *et al* using a micro-sized probe for scanning thermal microscopy. Absorption coefficients of hydrogenated microcrystalline silicon films were estimated using resonant photothermal bending spectroscopy by detecting the bending of a film/substrate bimorph structure caused by the thermal expansion of a thin film under light illumination [55].

3.3 Photothermal Cantilever Deflection Spectroscopy

It has been shown that photothermal absorption spectroscopy can be implemented with a mechanical sensor. Photothermal cantilever deflection spectroscopy (PCDS) examines wavelengths of IR sequentially like a dispersive IR spectrometer where a bimaterial cantilever, metal layer on silicon or silicon nitride cantilever, is used as a sample holder as well as an IR detector. The sample adsorbed or deposited on top of a cantilever interacts with IR light when IR light irradiates the cantilever. The molecules of the sample absorb IR light which matches their vibrational frequency, resulting in rise in the temperature of the cantilever at the irradiated area. The cantilever deflects due to the different thermal expansion coefficients of the two materials used for the cantilever. The amount of deflection of the cantilever can be related to the amount of IR light absorbed in the sample [56].

By measuring the bending of a bimaterial cantilever due to photothermal heating, the sensitivity was increased by two orders of magnitude compared to standard photothermal deflection spectroscopy [57, 58]. The cantilever-based photothermal spectroscopy has been applied for detecting chemicals [59–61], biomolecules [62], trace explosives [63, 64], and chemical warfare agents in applications such as humanitarian demining [62, 65], using a quantum cascade laser [66], using a nanoporous microcantilever [67], using a bimetallic microchannel cantilever [68], including standoff techniques [69,70], for investigating polymer thin films [56, 66], characterization in thermodynamic, thermomechanical, and chemical properties of a photosensitive polymer [71, 72], and selective detection of naphtha and bitumen in oil sands processing [73].

3.4 Micro- and Nanomechanical String Resonators

Micro and nano-electromechanical resonators have offered a range of extremely sensitive mass sensors, going down to the zeptogram-scale [74], real-time mass spectroscopy of nanoparticles [75–77], reaching the single protein level [78, 79], weighing biomolecules, single cells and single nanoparticles in fluid [80], even down to the yoctogram mass level [81] and to the atomic-resolution [82].

Such mass sensors, however, lack intrinsic selectivity and typically rely on selective interfaces for chemical specificity [83]. One way to obtain good specificity without surface modification of string resonators is to use a string resonator as a detector of a spectrometer as mechanical string resonators are promising temperature sensors due to their high sensitivity and well-defined resonance peaks [84]. Larsen *et al* reported that a temperature resolution of $2.5 \times 10^{-4}\,^{\circ}\mathrm{C}$ was obtained when using the shortest 114 μm long silicon-rich silicon nitride strings and by monitoring the temperature induced fre-

quency detuning [85]. Silicon-rich silicon nitride strings showed the best overall performance compared to aluminium and nickel strings due to their high reproducibility and excellent dynamic properties in spite of the lower sensitivity [85]. They also demonstrated measurements of a simple absorption spectrum of multiple polystyrene microparticles illuminated with a LED light source of red, green and blue on a microstring [86].

Strings allow for a simpler fabrication compared to bimaterial cantilevers as only a single material is necessary for the beam structure which is clamped at both ends. Measuring frequency detuning is a more robust detection scheme than measuring deflection. Heat dissipation can be minimized as no metal is required for strings and it is possible for strings to have a larger aspect ratio. Finally strings facilitate simple non-diffusion limited analyte sampling, which is described in Section 4.3 [76].

When this project was started, there was no research conducted in the field of photothermal spectroscopy using micro- and nanostring resonators although string resonators possess several advantages to be employed as a thermal detector for photothermal spectroscopy. At some point, we might find that resonating mechanical strings are a better solution as thermal detectors for photothermal spectrocopy. Combined with the unique fingerprints shown in the mid-IR region, a photothermal IR spectroscopy technique with mechanical string resonators will be the subject of this Ph.D. thesis for the believed potential.

Chapter 4

Theory

Understanding the resonating behaviour of mechanical strings is essential when exploring the use of them as the sensing part in photothermal spectroscopy. This chapter will start with general string theory. From the equation of motion for an undamped beam to an expression for the photothermal frequency resoponse of a string will be deduced. Then the principle of photothermal IR spectroscopy with mechanical string resonators will be presented. Lastly, general theory on infrared spectroscopy will be presented[1].

4.1 String Approximation

The equation of motion for a thin tensile stressed beam, as depicted in Fig. 4.1, with a length L, width w and height h, is given by the Euler-Bernoulli beam equation: [90]

$$EI_z \frac{\partial^4 u(x,t)}{\partial x^4} - N \frac{\partial^2 u(x,t)}{\partial x^2} + \rho A \frac{\partial^2 u(x,t)}{\partial t^2} = 0, \tag{4.1}$$

[1]Section 4.1 and Section 4.4 are to a large extent based on materials found in [87–89].

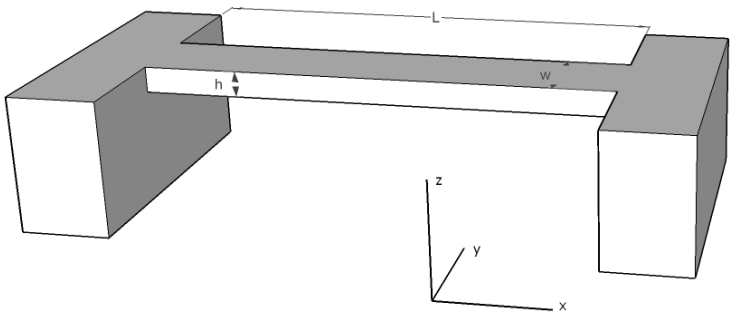

Figure 4.1: Schematic drawing of a doubly-clamped beam with length L, width w and height h.

where $u(x,t)$ is the displacement function of the beam as a function of position along the beam and time, E Young's modulus, I_z the area moment of inertia, N the axial force, ρ the mass density and $A = wh$ the cross-sectional area of the beam. The axial force N can also be written as σA, where σ is the axial stress. The three force terms in Eq. 4.1 represent the flexure, tensile stress and inertia.

An analytical solution to Eq. 4.1 is not available using the boundary conditions for a doubly-clamped beam: $U(0,t) = U(L,t) = 0$ and $U'(0,t) = U'(L,t) = 0$ [91]. The boundary conditions of a pinned-pinned beam: $U(0,t) = U(L,t) = 0$ and $U"(0,t) = U"(L,t) = 0$ can, however, give an approximated solution to Eq. 4.1. The eigenfrequency of a doubly-clamped beam is then given as

$$\omega_n = \frac{\lambda_n^2}{L^2}\sqrt{\frac{EI}{\rho A}}\sqrt{1 + \frac{\sigma A L^2}{\lambda_n^2 EI}}, \tag{4.2}$$

where $\lambda_n^2 = n\pi$ (n=1,2,3,..) are solutions to the characteristic equation. It can be seen that the eigenfrequency is increasing with increasing tensile stress. The flexural rigidity of the beam can be neglected when the tensile stress becomes sufficiently high, which is true when $12\sigma L^2 \gg \lambda_n^2 E h^2$. Ignoring the flexural rigidity, Eq. 4.2 is reduced to

$$\omega_n = \frac{\pi}{L}\sqrt{\frac{\sigma}{\rho}} \qquad n = 1, 2, 3, .., \tag{4.3}$$

which is the eigenfrequency of a string with the n$^{\text{th}}$ mode shape

$$u_n(x) = a_n sin(\frac{n\pi}{L}x), \tag{4.4}$$

where a_n is the vibrational amplitude for the n$^{\text{th}}$ mode.

Dividing the result by 2π the eigenfrequency in hertz can be written by

$$f = \frac{n}{2L}\sqrt{\frac{\sigma}{\rho}}. \tag{4.5}$$

4.2 Photothermal Frequency Response

Heating of a string will make it expand in accordance with the coefficient of thermal expansion α of the string material. This will lead to a reduction in the tensile stress which is reflected in the resonance frequency. A reduced tensile stress causes a lower resonance frequency according to Eq. 4.5.

We shall now consider an idealized quasi one-dimensional situation, where the string is heated by an applied power P distributed evenly in a cross-section of the beam at position x_0, while the ends of the beam are kept at

ambient temperature $T(0) = T(L) = 298\,\mathrm{K}$. The heat flux density $\mathbf{J}_Q$ is given by Fourier's Law of heat conduction

$$\mathbf{J}_Q = -\kappa \nabla T, \tag{4.6}$$

where κ is the thermal conductivity of the string material and ∇T is the temperature gradient. The temporal and spatial evolution of the temperature is governed by the heat continuity equation

$$\rho c_p \frac{\partial T}{\partial t} = -\nabla \cdot \mathbf{J}_Q + q, \tag{4.7}$$

where c_p is the specific heat capacity of the string material, while q is the dissipated power density. We shall only consider steady state, where the divergence of the heat flux density is zero, $\nabla \cdot \mathbf{J}_Q = 0$, except at $x = x_0$; as a result the temperature profile must be piecewise linear if the thermal conductivity is constant

$$T(x) = \begin{cases} T_0 + [T(x_0) - T_0]\, x/x_0 & , \text{for } 0 \le x \le x_0 \\ T_0 + [T(x_0) - T_0]\, (L - x)\,/\,(L - x_0) & , \text{for } x_0 \le x \le L. \end{cases} \tag{4.8}$$

The average temperature increase across the length of the beam then becomes $\Delta T = [T(x_0) - T_0]\,/2$. The absorbed power at $x = x_0$ must, according to the heat continuity equation, equal the sum of heat fluxes to the left and right of $x = x_0$, i.e. $P = A\kappa\,[T(x_0) - T_0]\,[1/x_0 + 1/\,(L - x_0)]$, where $A = wh$ is the cross-sectional area of the string. As a result the average temperature increase of the string becomes

$$\Delta T \equiv \frac{T(x_0) - T_0}{2} = \frac{PL}{8\kappa A} \frac{4}{\frac{L}{x_0} + \frac{L}{L - x_0}} = \frac{PL}{8\kappa A} \frac{4x_0\,(L - x_0)}{L^2}. \tag{4.9}$$

The temperature increase is maximized when the power is dissipated at the mid-point of the beam with $x_0 = L/2$, and then

$$\Delta T = \frac{PL}{8\kappa A}. \tag{4.10}$$

The thermoelastic response of the string material is governed by $\varepsilon = \sigma/E + \alpha\,(T - T_0)$, since only the longitudinal stress in the string is non-zero; here ε is the longitudinal strain. The stress, however, must be independent on position in steady state, and at the same time the mean strain ε_0 must be unaffected by the temperature increase since the length of the string is defined by the fixed end points at $x = 0$ and $x = L$; i.e. ε_0 is the built-in strain in the string. It, thus, follows that the stress in the string becomes

$$\sigma = E\varepsilon_0 - \alpha E \Delta T = E\varepsilon_0 \left(1 - \frac{\alpha}{\varepsilon_0} \Delta T\right) = \sigma_0 \left(1 - \frac{\alpha E}{\sigma_0} \Delta T\right), \tag{4.11}$$

where $\sigma_0 = E\varepsilon_0$ is the initial tensile pre-stress. Then the resulting resonant frequency, according to Eq. 4.5, becomes

$$f_n(P) = \frac{n}{2L}\sqrt{\frac{\sigma_0}{\rho}}\sqrt{1 - \frac{\alpha E}{\sigma_0}\Delta T} = \frac{n}{2L}\sqrt{\frac{\sigma_0}{\rho}}\sqrt{1 - \frac{\alpha E}{\sigma_0}\frac{PL}{8\kappa A}\frac{4x_0\,(L - x_0)}{L^2}}. \tag{4.12}$$

If the string is heated at its mid-point $x_0 = L/2$, the resonant frequency shift magnitude is maximized, and the resonant frequency becomes

$$f_n(P) = \frac{n}{2L}\sqrt{\frac{\sigma_0}{\rho}}\sqrt{1 - \frac{\alpha E}{\sigma_0\kappa}\frac{PL}{8A}} \simeq \frac{n}{2L}\sqrt{\frac{\sigma_0}{\rho}}\left(1 - \frac{\alpha E}{\sigma_0\kappa}\frac{PL}{16A}\right). \tag{4.13}$$

In Eqs. 4.12 and 4.13 the front factor is the initial resonant frequency of the string due to the pre-stress, while the last factor is the correction due to thermal effects caused by the dissipated power. Note, in the derivation of the model equations temperature independent Young's modulus, mass density, and thermal expansion coefficient are assumed. The relative resonance frequency change of a mechanical string resonator as a function of the absorbed power P in the string center is given by

$$\frac{\Delta f}{f} = -\frac{\alpha E}{\sigma_0\kappa}\frac{L}{16A}P. \tag{4.14}$$

The power sensitivity, in the case of heating at the center, equals:

$$S_p = \frac{df_n(P)}{dP} = \frac{-nE\alpha}{32\rho\kappa A\sqrt{\frac{\sigma_0}{\rho} - \frac{E\alpha PL}{8\rho\kappa A}}}. \tag{4.15}$$

According to this model, the power sensitivity increases with increasing resonant mode number, Young's modulus, thermal expansion coefficient and string length and with decreasing mass density, pre-stress, thermal conductivity, or the cross-sectional area of the string.

For a bimaterial string consisting of a base layer with a thickness h_b and a coating layer with a thickness h_c, an effective thermal conductivity $\kappa^\star$, an effective stress $\sigma^\star$, and an effective mass density $\rho^\star$ can be defined as

$$\kappa^\star = \frac{h_b\kappa_b + h_c\kappa_c}{h_b + h_c} \tag{4.16}$$

$$\sigma^\star = \frac{h_b\sigma_b + h_c\sigma_c}{h_b + h_c} \tag{4.17}$$

$$\rho^\star = \frac{h_b\rho_b + h_c\rho_c}{h_b + h_c}, \tag{4.18}$$

where where the parameters with the subscript b and c belong to the base layer and the coating layer, respectively. By inserting $\sigma = E\varepsilon_0 - \alpha E\Delta T$ (Eq. 4.11) in Eq. 4.17, an effective stress $\sigma^\star$ becomes

$$\sigma^\star = \frac{\varepsilon_0(E_bh_b + E_ch_c) - (\alpha_bE_bh_b + \alpha_cE_ch_c)\Delta T}{h_b + h_c}. \tag{4.19}$$

The maximum temperature increase when the power is dissipated at the mid-point of the beam is

$$\Delta T = \frac{PL}{8\kappa^\star w(h_b + h_c)} = \frac{PL}{8w(h_b\kappa_b + h_c\kappa_c)}. \tag{4.20}$$

The resonance frequency of a bimaterial string resonator as a function of the absorbed power P in the string center is given by

$$\begin{aligned} f &= \frac{n}{2L}\sqrt{\frac{\sigma^\star}{\rho^\star}} = \frac{n}{2L}\sqrt{\frac{\varepsilon_0(E_b h_b + E_c h_c) - (\alpha_b E_b h_b + \alpha_c E_c h_c)\Delta T}{h_b\rho_b + h_c\rho_c}} \\ &= \frac{n}{2L}\sqrt{\frac{\varepsilon_0(E_b h_b + E_c h_c)}{h_b\rho_b + h_c\rho_c}}\sqrt{1 - \frac{\alpha_b E_b h_b + \alpha_c E_c h_c}{\varepsilon_0(E_b h_b + E_c h_c)}\frac{PL}{8w(h_b\kappa_b + h_c\kappa_c)}} \\ &\simeq \frac{n}{2L}\sqrt{\frac{\varepsilon_0(E_b h_b + E_c h_c)}{h_b\rho_b + h_c\rho_c}}\left(1 - \frac{\alpha_b E_b h_b + \alpha_c E_c h_c}{\varepsilon_0(E_b h_b + E_c h_c)}\frac{PL}{16w(h_b\kappa_b + h_c\kappa_c)}\right). \end{aligned} \tag{4.21}$$

In Eq. 4.21 the front factor is the initial resonant frequency of the string due to the pre-stress, while the last factor is the correction due to thermal effects caused by the dissipated power. The relative resonance frequency change of a mechanical string resonator as a function of the absorbed power P in the string center is given by

$$\frac{\Delta f}{f} = -\frac{\alpha_b E_b h_b + \alpha_c E_c h_c}{\varepsilon_0(E_b h_b + E_c h_c)}\frac{L}{16w(h_b\kappa_b + h_c\kappa_c)}P. \tag{4.22}$$

4.3 Photothermal Spectroscopy with Mechanical Resonators

As it has been described in Section 3.2, the cantilever-based photothermal spectroscopy has been applied for detecting many different targets such as chemicals, bio-molecules and trace explosives. Instead of using cantilevers for photothermal spectroscopy, string resonators are employed in this photothermal spectroscopy. The responsivity of chemical or biochemical sensors is strongly dependent on the sample collection efficiency [92]. The probability of nano-scale sample entities to stick to a micro- or nano-scale sensor surface by diffusion is very low, which results in long sampling time [93, 94]. For many sensor applications, the available sample concentration is, however, below the detection limit. This problem is commonly overcome by performing a pre-concentration of the analyte. Sample preparation and pre-concentration are not only time consuming but also contribute to increased error in the total analysis of a sample. In our photothermal sensor we apply an efficient non-diffusion limited sampling method in which airborne species

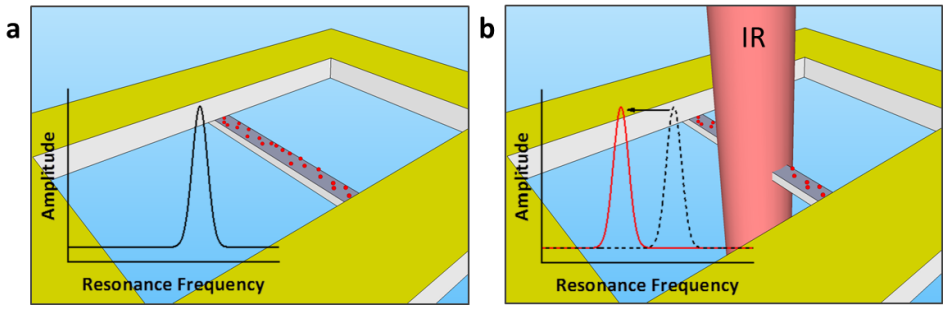

Figure 4.2: Schematic drawings explaining photothermal IR spectroscopy with a mechanical string resonator with in-situ non-diffusion limited sampling. (a) Airborne species are deposited on a string by aerosol flowing through the chip thereby passing the string resonator. The airborne species are then efficiently collected on the string mainly by inertial impaction. (b) The collected species are excited into vibration modes by absorption of IR photons causing a photothermal heating. The thermal energy is then transferred to the string resulting in a frequency detuning.

are directly collected on the mechanical string resonator with an up to 100% collection efficiency of the species that are flowing in the projection of the string resonator [76].

The micro- and nanostring spectrometer thus fulfills two core roles: 1) as sampling / pre-concentrating element and 2) as thermally isolated ultrasensitive temperature sensing element. Once the analyte is collected on the string, it is exposed to monochromatic IR radiation. When IR photons are absorbed by the analyte molecules on the string surface, the analyte molecules undergo transitions from the ground vibrational states to the excited states. Eventually, the energy is released to the string surface through vibrational energy relaxation. These processes result in heating up the string, generating a frequency shift of the string [66]. Fig. 4.2 schematically depicts the principle of photothermal IR spectroscopy. A string vibrates at its resonance frequency as shown in Fig. 4.2(a). When the string is heated by the absorbed heat by the sample, the heated string expands in accordance with the thermal expansion coefficient of the string material and this leads to a reduction in the tensile stress. The reduced tensile stress causes a lower resonance frequency according to Eq. 4.5, as shown in Fig. 4.2(b). The resonance frequency shift is proportional to the heat flux into the string. Photothermal spectra, recorded while monochromatic IR light is scanned, are therefore similar to IR absorption spectra and contain a superposition of characteristic vibrational signatures of the chemical entities in the sample.

4.4 Infrared Spectroscopy

The part of the electromagnetic spectrum between the visible and microwave regions is the IR region which is divided into three regions: the near-infrared

with a wavenumber range from 4000 to 14000 cm^{-1}, mid-infrared with a wavenumber range from 400 to 4000 cm^{-1}, and far-infrared with a wavenumber range from 4 to 400 cm^{-1} [88]. Frequency, ν, is the number of wave cycles that pass through a point in one second, which is measured in Hz. Wavelength, λ, is the length of one complete wave cycle, which is often measured in cm. Wavelength and frequency are inversely related:

$$c = \lambda\nu, \tag{4.23}$$

where c is the speed of light, 3×10^8 m/s. A wavenumber is the inverse of the wavelength in cm:

$$\bar{\nu} = \frac{1}{\lambda}, \tag{4.24}$$

where $\bar{\nu}$ is in units of cm^{-1}. Energy is related to frequency, wavelength and wavenumber as follows:

$$E = h\nu = \frac{hc}{\lambda} = hc\bar{\nu}, \tag{4.25}$$

where h is Planck's constant, 6.6×10^{-34} J·s.

Absorption occurs when a molecule is exposed to IR radiation and the radiant energy matches the energy of a specific molecular vibration. The wavenumbers at which a molecule absorbs radiation give information on functional groups present in the molecule. There are two types of molecular vibrations: stretching and bending. A molecule consisting of n atoms has a total of $3n$ degrees of freedom. In a nonlinear molecule, 3 of these degrees are rotational, 3 are translational, and the remaining $3n$-6 correspond to fundamental vibrations. In a linear molecule, 2 degrees are rotational, 3 are translational, and the remaining $3n$-5 correspond to fundamental vibrations. The stretching and bending vibrations for a methylene group are illustrated in Fig. 4.3(a). Bending vibrations occur at lower frequencies than corresponding stretching vibrations.

The stretching frequency of a bond can be approximated by Hooke's law, where two atoms and the connecting bond are treated as a simple harmonic oscillator composed of two masses joined by a spring as shown in Fig. 4.3(b). According to Hooke's law, the frequency of the vibration of the spring is given by:

$$\nu = \frac{1}{2\pi}\sqrt{\frac{k}{m}} \tag{4.26}$$

where k is the force constant, m is the mass and ν is the frequency of the vibration. Vibrational motion is quantized and it follows the rules of quantum mechanics. The allowed transitions fit the following equation expressing the potential energy:

$$E = (n+1)h\nu, \tag{4.27}$$

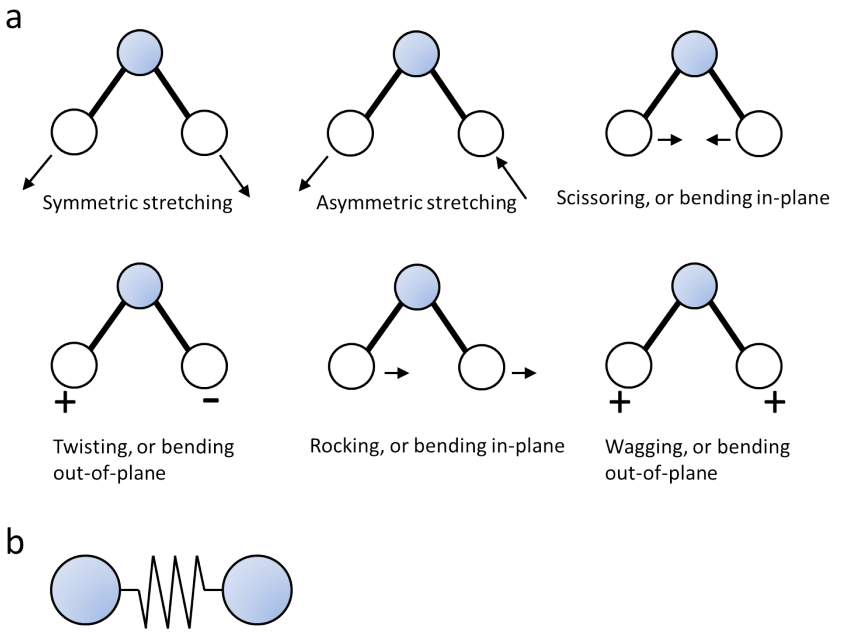

Figure 4.3: (a) Stretching and bending vibrational modes for a methylene group. (b) Simple harmonic oscillator composed of two atoms joined by a spring.

where n is the quantum number (0,1,2,..). According to the selection rule, only transitions to the next energy level are allowed. Therefore molecules will absorb an amount of energy equal to $h\nu$. When transitions of $2h\nu$, $3h\nu$, or higher occur, bands called overtones appear in an IR spectrum. They are of lower intensity than the fundamental vibration bands.

In reality a molecule is an anharmonic oscillator, whose bond can come apart and cannot be compressed beyond a certain point. As the interatomic distance increases, the energy reaches a maximum. For the case of a diatomic molecule, the wavenumber deduced from Hooke's law can be written as

$$\bar{\nu} = \frac{1}{2\pi c}\sqrt{\frac{f(m_1 + m_2)}{m_1 m_2}}, \tag{4.28}$$

where m_1 and m_2 are the mass of atoms 1 and 2 in g, respectively.

Band intensities in an IR spectrum can be expressed as either absorbance (A) or percent transmittance (%T). Absorbance is the logarithm of the reciprocal of the transmittans:

$$A = \log_{10}\left(\frac{1}{T}\right). \tag{4.29}$$

4.5 Summary

The general theory describing the undamped free vibration and the influence of tensile stress on the eigenfrequency of doubly-clamped beams have been presented. The expression for the eigenfrequency of strings has been modified to include the changes induced by heating the center of a string, including a bimaterial string. The principle of photothermal spectroscopy with mechanical string resonators has been presented. Combined with non-diffusion limited sampling, photothermal IR spectroscopy with mechanical string resonators provides vibrational signatures of analytes by measuring a frequency detuning of a string. Lastly some general theory of infrared spectroscopy has been presented.

Chapter 5

Fabrication

The analytical expression for the photothermal frequency response of a string resonator, Eq. 4.13, states that the relative frequency shift magnitude increases with absorbed power, Young's modulus, thermal expansion coefficient and string length, while it decreases when pre-stress, thermal conductivity, or the cross-sectional area of the string increases. To investigate photothermal IR spectroscopy using string resonators, different types of strings are to be fabricated.

The strings need tensile stress at the end of the fabrication process since the sensing principle relies on changes in tensile stress. It is often observed that stress develops in films during deposition or growth. These are called intrinsic stress or growth stress. Redistribution of a matter usually result in film stresses since the film is constrained by the substrate. When a film on a substrate is subjected to a temperature change, the difference in thermal expansion will result in thermal stresses in film and substrate. Stress in a deposited or grown film can be compressive or tensile. If the chosen material is not pre-stressed after deposition/growth, annealing can be used to introduce tensile stress in some cases. The level of tensile stress has to be considered as the relative frequency shift magnitude decreases with increasing stress. Some materials like stoichiometric LPCVD silicon nitride tend to be highly stressed, up to 1 GPa, after deposition [95].

To maximize the relative frequency shift magnitude, Young's modulus and thermal expansion coefficient have to be as large as possible and pre-stress and thermal conductivity have to be as small as possible. When focusing on Young's modulus, materials like silicon nitride, silicon carbide, aluminum nitride etc. are attractive but they also have low thermal expansion coefficient. Polymers generally have high thermal expansion coefficient but low Young's modulus. Metals tend to have the values of thermal expansion coefficient and Young's modulus between those for ceramics and polymers. Talbe 5.1 shows Young's modulus, thermal expansion coefficient, thermal conductivity and pre-sterss of silicon, aluminium, silicon rich silicon nitride, stoichiomet-

Table 5.1: Mechanical and thermal properties of silicon, aluminium [84, 98], silicon rich silicon nitride [84, 99–103], stoichiometric silicon nitride [101, 104–107] and silicon carbide [108, 109].

	Si	Al	Si_xN_y	Si_3N_4	SiC
Young's modulus [GPa]	69	131-170	295-360	310-325	450
Thermal expansion coefficient [ppm/°C]	2.56	23.1	1.23	1.5-2.6	3.8-4.3
Thermal conductivity [W/(m·°C)]	149	237-250	2.5-24	2.1	2.1
Pre-stress [MPa]	0	18.3	230-270	1100-1150	tunable

ric silicon nitride and silicon carbide. Fabrication techniques available in the cleanroom at DTU Danchip have to be taken into account when selecting the string materials. A material like silicon carbide is interesting for this kind of application as the stress can be tailored by changing the deposition parameters and annealing [96]. Young's modulus of silicon carbide is higher than that of aluminium and silicon nitride, the thermal expansion coefficient of silicon carbide is between that of aluminium and silicon nitride, and it has been used for nanomechanical resonators [97]. However, silicon carbide deposition is not possible with the current cleanroom facility at DTU Danchip.

A higher quality factor results in a higher frequency resolution. Larsen *et al* investigated the temperature sensitivity of silicon nitride and aluminum microstrings [84]. A relative temperature sensitivity of -1.74%/°C was measured for the aluminum strings which was more than one order of magnitude higher than reported values for a comparable device. The quality factor was ranging from 3×10^5 for the 114 µm long strings to 2.4×10^6 for the 1579 µm strings. The quality factor of 200 µm long aluminium strings was 3700. The quality factor of the silicon nitride strings is, thus, two orders of magnitude higher than that of the aluminium strings. Schmid *et al* measured a quality factor of almost 7 million for stoichiometrich silicon nitride strings at a resonance frequency of 176 kHz which is higher than the quality factor of silicon rich silicon nitride strings [110]. On the ohter hand, a higher stress in the string material results in a smaller frequency shift according to Eq. 4.13. Inserting the values from Table 5.1, $\alpha E/\sigma_0\kappa$ for aluminium, silicon rich silicon nitride and stoichiometric silicon nitride become approximately 3.6×10^{-7}, 1.0×10^{-7} and 3.2×10^{-8}, respectively. Silicon carbide will have a similar value to silicon nitride depending on the tensile stress. An aluminium string

will induce a largest frequency shift theoretically among these 3 materials when the other parameters are the same. After these considerations, three string materials have been selected: Aluminium, silicon rich silicon nitride and stoichiometric silicon nitride. Aluminum has been selected because it has the possibility of achieving a largest photothermal response. Stoichiometric silicon nitride has been selected because of its highest frequency resolution. Silicon rich silicon nitride has been selected because of the possibility of achieving both a large photothermal response and also a high frequency resolution.

5.1 Aluminium Strings

Aluminium strings have been fabricated by means of standard fabrication techniques. Fig. 5.1 gives a schematic overview of the fabrication process. A detailed process sequence can be found in Appendix A. The fabrication starts with a 350 µm thick double side polished 4 inch silicon (100) wafer. 1) A 550 nm thick layer of LPCVD silicon nitride is deposited on both sides of the wafer. The thickness of the silicon nitride was measured using an ellipsometer. 2) A 1.5 µm thick layer of AZ5214e photoresist is spin-coated on the back side of the wafer and patterned by UV lithography. The lithography mask is aligned to the flat of the wafers. This pattern is transferred into the silicon nitride by an anisotropic RIE etch (trifluoromethane: 8 sccm, nitrogen: 43 sccm, pressure: 38 mTorr and power: 50 W). 3) A potassium hydroxide etch (28 wt% at 80 °C, 4.5 hours) is used to etch through the silicon wafer from the backside. 4) A 100 nm thick layer of aluminium is deposited on the front side by electron beam deposition. 5) A 1.5 µm thick layer of AZ5214e photoresist is spin-coated on the front side of the wafers and patterned by UV lithography. The lithography mask is aligned to the flat of the wafer. This pattern is transferred into the aluminium by inductively coupled plasma (ICP) etching (hydrogen bromide: 15 sccm, chlorine: 25 sccm, pressure: 1 mTorr, coil power: 500 W, platen power: 100 W, temperature: 20 °C) for 30 seconds. Then the strings are annealed in an oven at 250 °C for 3 hours. 6) A 1.5 µm thick layer of AZ5214e photoresist is spin-coated on the front side to protect the aluminium strings while silicon nitride under the strings are being etched. 7) The LPCVD silicon nitride on the front side is patterned from the back side in a similar way as the silicon nitride on the back side by RIE etching and the strings are released. 8) The photoresist is removed in acetone.

An schematic representation of the fabricated chips can be seen in Fig. 5.2. All chips are 7.0 mm long and 10 mm wide and contain 30 strings with the same length. The 30 strings are divided into 6 groups with designed widths of 3.0, 6.0, 9.0, 12, 15 and 18 µm. The designed lengths of the strings ranges from 100 to 900µm. Scanning electron microscope (SEM) images of two of

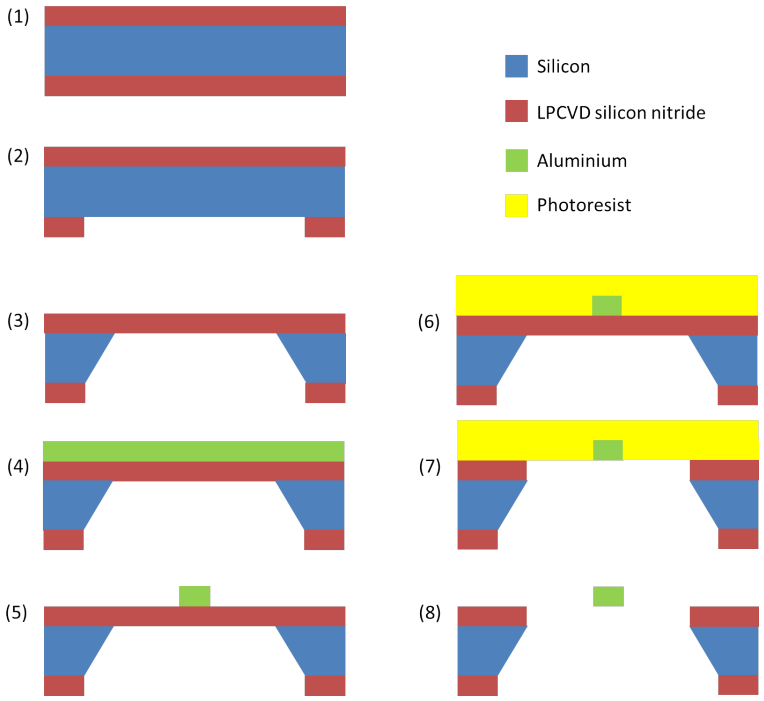

Figure 5.1: Schematic overview of the aluminium string fabrication process. 1) Deposition of LPCVD silicon nitride, 2) UV lithography and pattern transfer by RIE etching on the backside, 3) pattern transfer in silicon substrate by potassium hydroxide etching on the backside, 4) deposition of aluminium by electron beam evaporation, 5) UV photolithography and pattern transfer by ICP etching on the front side, 6) protection of strings by spin-coating photoresist, 7) release of strings by RIE etching on the backside and 8) removal of photoresist in acetone.

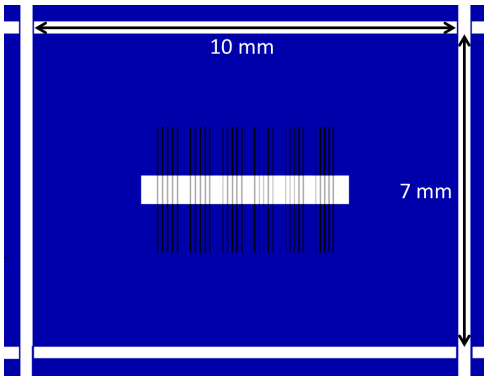

Figure 5.2: Schematic drawing of a chip design for aluminium strings. Each chip contains 30 strings with the same length. These strings are devided into 6 groups with designed widths of 3.0, 6.0, 9.0, 12, 15 and 18 µm. The length of the strings ranges from 100 µm to 900 µm.

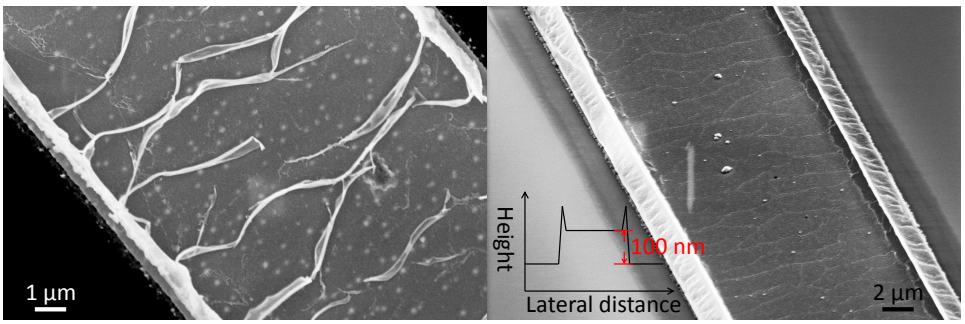

Figure 5.3: SEM images of aluminium strings showing the polymer-like material left after the removal of photoresist by an ICP etcher and by a plasma asher. The schematic drawing depicts the cross-section view of the aluminium string with the polymer-like material verified by a stylus profilometer, showing the veils at the edges of the aluminium string.

the fabricated aluminium strings can be seen in Fig. 5.3. There is a polymer-like material along the edges of the aluminium strings. The schematic drawing in the right image depicts the cross-section view of the aluminium string with polymer-like material verified by a stylus profilometer, showing the veils at the edges of the aluminium string. All aluminium strings were covered with the polymer-like material.

Energy dispersive X-ray spectroscopy (EDX) was employed to analyze the elemental composition of the veils using LEO 1550 Scanning Electron Microscope. SEM-EDX is capable of detecting and quantifying elements heavier than carbon. Fig. 5.4 shows the areas analyzed by EDX: area 1 is for the polymer-like veil and area 2 for the string without the veils. The area 1 contained 3 times more oxygen than the area 2 as shown in Table 5.2. The composition of the photoresist AZ5214e used in the fabrication is not revealed,

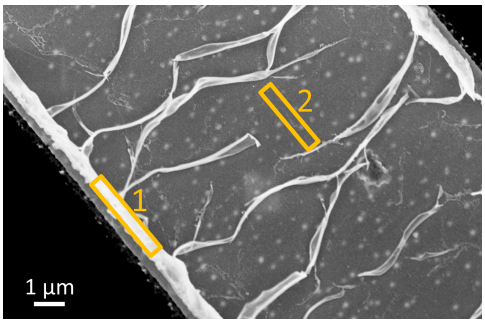

Figure 5.4: SEM image of an aluminium string with polymer-like veils, showing two areas analyzed by SEM-EDX.

Table 5.2: Elemental composition analysis by SEM-EDX.

Element	Atomic % in area 1	Atomic % in area 2
Nitrogen	31.64	32.20
Oxygen	5.07	1.57
Aluminium	4.25	5.04
Silicon	58.76	61.19

however, a polymer often contains oxygen. To investigate the polymer-like veils further, X-ray photoelectron spectroscopy (XPS) was employed to analyze the elemental composition of veils using Thermo K-Alpha system. XPS is capable of detecting and quantifying every element except hydrogen and helium. The disadvantage of XPS is a larger spot area of minimum 30 µm compared to EDX of ∼1 µm. Fig. 5.5 shows the areas analyzed by XPS: area 1 is for the aluminium strings on a silicon nitride support and area 2 for the silicon nitride support. As expected from the SEM-EDX results, more carbon and oxygen were found in the area 1 as shown in Table 5.3, which is in an agreement with the hypothesis of the polymer-like veils being polymer. Besides carbon and oxygen, fluorine was found only in the area 1, which could bind to aluminium as aluminium fluoride. The gases used to etch aluminium are chlorine and hydrogen bromide that do not contain fluorine. We suspect that the fluorine originates from the sulphur hexafluoride gas for silicon etching, which was used by another user of the ICP etcher.

In order to avoid the veils, the following parameters for the aluminium etch were investigated according to the recommendations from the manufacturer of the ICP etcher: power, cooling temperature, plasma ion density. None of the parameters changed the result and the polymer-like material was still

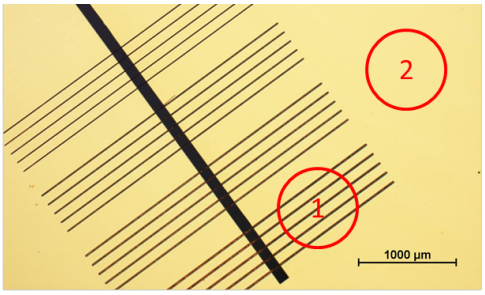

Figure 5.5: Optical microscope image of aluminium strings with polymer-like veils, showing two areas analyzed by XPS.

Table 5.3: Elemental composition analysis by XPS.

Element	Atomic % in area 1	Atomic % in area 2
Carbon	3.07	2.23
Nitrogen	15.08	16.56
Oxygen	42.42	40.78
Fluorine	1.54	-
Silicon	37.90	40.44

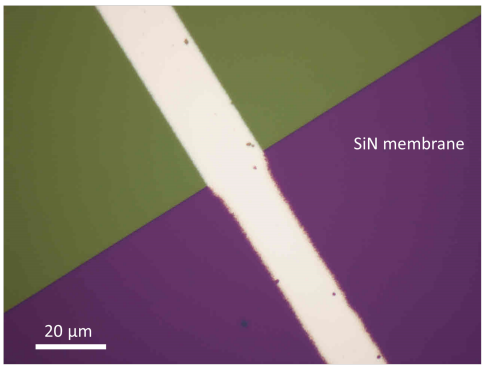

Figure 5.6: Optical microscope image of an aluminium string patterned by wet etch. The greenish area is supported by the silicon substrate and the purplish area has only silicon nitride membrane of 550 nm thick.

on the strings. Different photoresist strip methods were also investigated to remove the veils: oxygen plasma by the ICP etcher, oxygen plasma by an plasma asher and by acetone rinse. None of them succeeded in removing the veils. Apart from the dry etching, the aluminium strings were patterned by wet etch. The pattern was not well-transferred from the photoresist to the aluminium probably due to a difference in the etch rate between the aluminium on the swaying silicon nitride thin film of 550 nm and the aluminium on the stationary silicon substrate of 350 µm in the wet etch solution. After all these investigations on aluminium etching, the former PhD student Tom Larsen found that aluminium string resonators displayed a considerable amount of hysteresis in the frequency versus temperature curves, which is highly undesirable when considering both accuracy and precision [85]. It was thus decided to discontinue the investigation of the fabrication of aluminium strings and to concentrate on the fabrication of silicon nitride strings.

5.2 Silicon Nitride Strings

It is well established that the intrinsic residual stress of silicon nitride films can be lowered by increasing the silicon component of the films. The lower intrinsic residual stress of silicon rich silicon nitride films is due to volumetric distortion of the Si-Si_xN_{4-x} tetrahedral unit brought about by a reduction in the local atomic strain of silicon-nitrogen bonds. The stress can be varied from tensile to compressive in the transition from stoichiometric silicon nitride to silicon rich silicon nitride as summarized by Habermehl [111]. Mechanical stress in silicon nitride remains due to (a) the mismatch between the coefficients of thermal expansion of the silicon substrate and the silicon nitride film and (b) the intrinsic stresses within the film. The thermal component of this stress is a small, compressive stress while the intrinsic component is a much larger tensile stress [99]. Olson has shown that the

residual stress can be estimated from the refraction index of a silicon nitride film [95].

Both silicon rich silicon nitride strings and stoichiometric silicon nitride strings have been fabricated by means of standard fabrication techniques. The fabrication process has been developed by Silvan Schmid. Fig. 5.7 gives a schematic overview of the fabrication process. A detailed process sequence can be found in Appendix A. The fabrication starts with a 350 µm thick double side polished 4 inch silicon (100) wafer. 1) A layer of LPCVD silicon nitride is deposited on both sides of the wafer: 185 nm thick layer for silicon rich silicon nitride and 61 nm thick layer for stoichiometric silicon nitride. The thickness of the silicon nitride was measured using an ellipsometer. 2) A 1.5 µm thick layer of AZ5214e photoresist is spin-coated on the front side of the wafer and patterned by UV lithography. The lithography mask is aligned to the flat of the wafer. 3) This pattern is transferred into the silicon nitride by an anisotropic RIE etch (sulphur hexafluoride: 32 sccm, oxygen: 8 sccm, pressure: 80 mTorr and power: 30 W). The etched pattern defines the outline of the chips and the individual strings. 4) A 400 nm thick layer of PECVD (plasma enhanced chemical vapor deposition) silicon nitride is deposited on the front side to cover the etched pattern. This layer protects the LPCVD silicon nitride while processing on the backside and releasing the strings later. 5) The LPCVD silicon nitride on the backside is patterned in a similar way as the silicon nitride on the front side using UV lithography and RIE etching. The lithography mask is aligned to the crystal orientation of the wafer, which is utilized in the release step. 6) A potassium hydroxide etch (28 wt% at 80 °C, 4.5 hours) is used to etch through the wafer from the backside and to release the strings. 7) The protective PECVD silicon nitride layer is finally removed in a buffered hydrogen fluoride etch.

The wafers of silicon rich silicon nitride strings were divided into individual chips of 7 mm × 10 mm containing 3 strings of the same dimensions with separate holes as seen in Fig. 5.8(a). This chip design enables us to sample at 3 different occasions when an appropriate sampling chamber is used. All chips of stoichiometric silicon nitride strings are 10 mm long and 7 mm wide and contain 25 strings with the same length as seen in Fig. 5.8(b). These chips were designed to facilitated the investigation of width-dependent factors. The 25 strings are divided into 5 groups with designed widths of 3.0, 6.0, 15, 30 and 50 µm. The designed length of the strings ranges from 100 to 500 µm. Each chip can be separated from the frame by holding a chip with a pair of tweezers and pressing the etched separation trenches with another pair of tweezers. The dimensions of the fabricated strings can differ from that of the design due to the manually operated photoresist development process, the misalignment of the mask, and the variation in the thickness of the wafers. The measured lengths and widths of the strings will therefore be presented together with the experimental results. A SEM image of a fabricated silicon rich silicon nitride string is shown in Fig. 5.9 with the

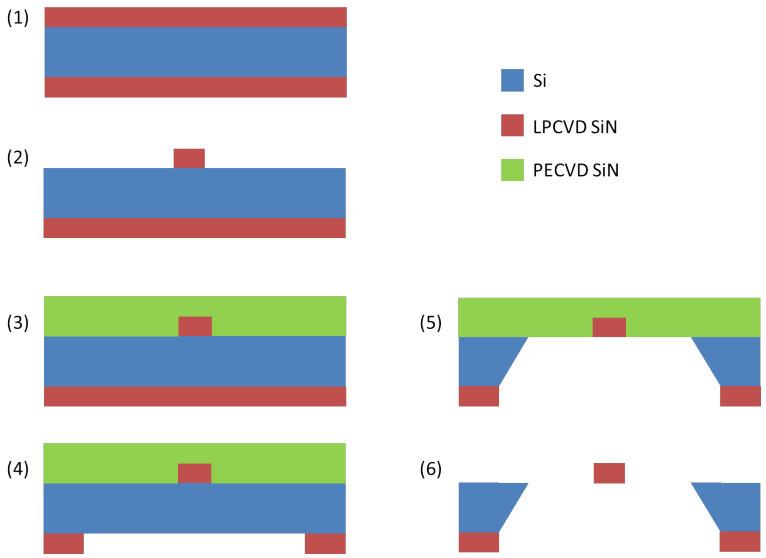

Figure 5.7: Schematic overview of the silicon nitride string fabrication process. 1) Deposition of LPCVD silicon nitride, 2) UV lithography and pattern transfer by RIE etching, 3) deposition of protective PECVD silicon nitride layer, 4) UV lithography and pattern transfer by RIE etching on the backside, 5) release of string by potassium hydroxide etch and 6) removal of PECVD silicon nitride by a buffered hydrogen fluoride etch.

measured dimensions of 213 µm long, 981 nm wide and 185 nm thick for the designed dimensions of 200 µm long, 1000 nm wide. The following strings were also used in the experiments: a) silicon rich silicon nitride strings of 505 µm long, 1.7 to 9.5 µm wide and 43 nm thick which had a chip design of 4 strings with the same width and 7 different widths on a chip fabricated by Peter Larsen, b) stoichiometric silicon nitride strings of 515 to 750 µm long, 2.0 to 49 µm wide and 157 and 312 nm thick with a chip design shown in Fig. 5.8(b) fabricated by Silvan Schmid, and c) stoichiometric silicon nitride strings patterned by deep-UV projection lithography that have a thickness of 100 nm, a length of 100 µm and a width of 5.0 µm and either 250, 500 or 1000 nm on a chip fabricated by Maksymilian Kurek.

5.3 Summary

Aluminium, silicon rich silicon nitride and stoichiometric silicon nitride were selected as string materials after considering the possibility to realize doubly-clamped beams with tensile stress using the cleanroom facility at DTU Danchip. Besides that, thermal expansion coefficient, Young's modulus and thermal conductivity were also taken into consideration since they affect the relative frequency shift magnitude. Aluminium strings are expected to have an excellent sensitivity, stoichiometric silicon nitride strings are expected to have the highest frequency resolution and silicon rich silicon nitride strings

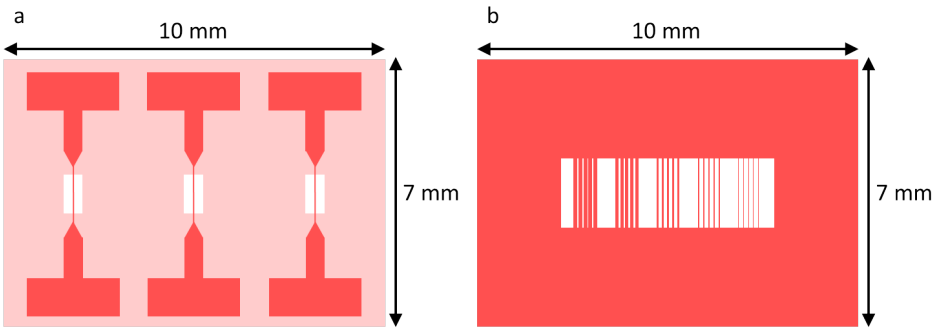

Figure 5.8: Chip designs for silicon nitride strings. (a) Silicon rich silicon nitride strings. Each chip contains 3 strings with the same dimensions. The width of the strings ranges from 1.0 µm to 5.0 µm, the length of the strings ranges from 100 µm to 500 µm and the thickness is 185 nm. (b) Stoichiometric silicon nitride strings. Each chip contains 25 strings with the same length. These strings are devided into 5 groups with designed widths of 3.0, 6.0, 15, 30 and 50 µm. The length of the strings ranges from 100 µm to 1500 µm.

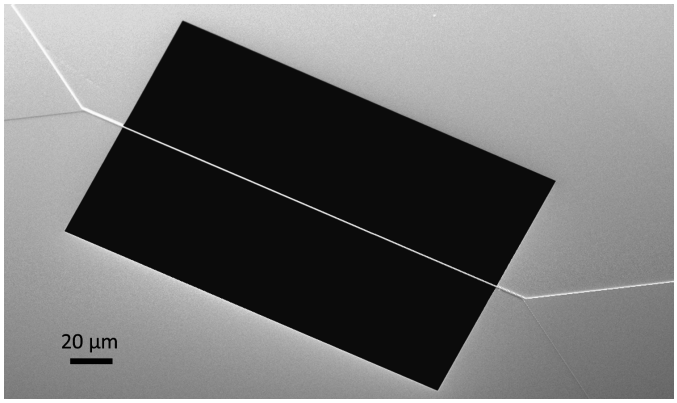

Figure 5.9: SEM image of a silicon rich silicon nitride string with the measured dimensions of 213 µm long, 981 nm wide and 185 nm thick for the designed demensions of 200 µm long and 1000 nm wide.

are expected to have advantages of both aluminium and stoihiometric silicon nitride strings. Fabrication of aluminium strings had an issue of polymer-like veils at the edges of aluminium strings which could not be removed or avoided with the currently available equipments at DTU Danchip. Both silicon rich silicon nitride and stoichiometric silicon nitride strings were fabricated successfully.

Chapter 6

Experimental

A number of different experimental setups have been used in the various measurements and they will be described in the following sections. The first section describes resonance frequency measurements and two ways of single frequency actuation. Photothermal infrared setups used for irradiating strings with IR light are described in the second section. The third section is used to describe the setup for aerosol sampling and information on chemicals. Two instruments for Fourier transform infrared spectroscopy (FTIR) are described in the fourth section and the instrument used for measuring the power of quantum cascade lasers (QCLs) is described in the fifth section.

6.1 Measuring Resonance Frequency

The microscope-based laser Doppler vibrometer (MSA-500) from Polytec GmbH can measure out of plane vibrations with frequencies ranging from 0 Hz to 24 MHz. Fig. 6.1 shows an optical schematic of a laser Doppler vibromer. The beam of a helium neon laser at a wavelength of 632.8 nm is split by a beam splitter 1 into a reference beam and a measurement beam. After passing through a beam splitter 2, the measurement beam is focused onto the sample, which reflects it. The reflected beam is deflected by the beam splitter 2 and then merged with the reference beam by the beam splitter 3 and is directed to the detector. The vibration amplitude and frequency are extracted from the Doppler shift of the reflected laser beam frequency due to the motion of the surface. The laser Doppler vibrometer contains three different objectives: 5×, 20× and 50× and the objective of 20× was used in the most of the measurements. The frequency resolution of a measurement depends on the number of FFT (fast Fourier transform) lines selected in the software used to analyse the measurement data.

All resonance frequencies were measured while keeping the chips at a pressure below 1.0×10^{-5} mbar. This means that the heat transfer to the surrounding is primarily via conduction through the two anchor regions

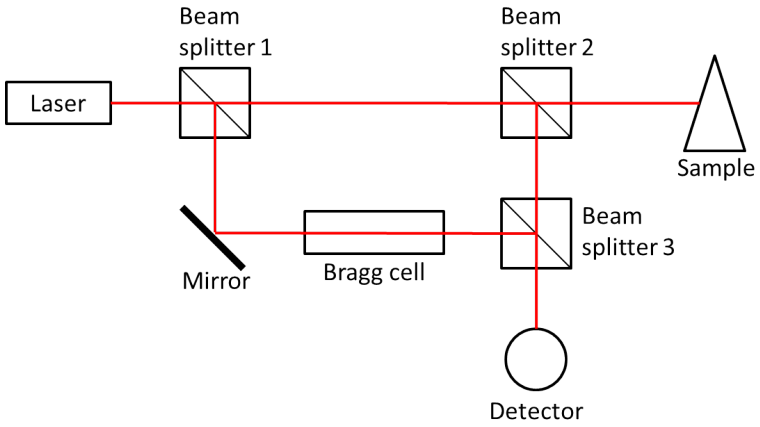

Figure 6.1: Optical schematic of a laser Doppler vibrometer. The laser is split by a beam splitter 1 into a reference beam and a measurement beam. After passing through a beam splitter 2, the measurement beam is focused onto the sample, which reflects it. The reflected beam is deflected by the beam splitter 2 and then merged with the reference beam by the beam splitter 3 and is directed to the detector.

of a string. The pressure was established inside the chamber using a turbo pump (HiPace 80, Pfeiffer Vacuum) and a membrane pump (PJ 15347-813.4, Leybold AG) placed in series. The pressure was measured using a MKS PDR900-1 vacuum gauge controller.

A single frequency of strings, in most of the cases the first mode of the thermal noise resonance peaks, was actuated using a ring piezo-electric ceramic linear transducer element (PZT) with an inner diameter of 6 mm (CMAR03, Noliac) which allows for actuation and having optical access from underneath at the same time. Two different methods were used to actuate a single frequency. The first method is a positive feedback loop as illustrated in Fig. 6.2(a). Vibration of a string is measured by the laser Doppler vibrometer. Then the output signal from the laser-Doppler vibrometer is used as a input signal for the limiter which gives a square wave output signal. The amplitude of this square wave output signal is adjusted to a proper size using an attenuator. The PZT element is used for actuating the string in accordance to the square wave signal. The frequency counter (53132A, Agilent Technologies) determines the frequency of the AC signal coming from the laser Doppler vibrometer. The sampling rate of this frequency counter is approximately 0.2 seconds. A LabVIEW program was used to acquire and store the values measured by the frequency counter. The used limiter was built by Silvan Schmid. This method is more suited for a longer string from 500 μm.

The second method used is a phase-locked loop (PLL), which can follow a resonance frequency over a defined range by locking-in a phase shift of a resonance peak as shown in Fig 6.2(b). The PZT element is driven by

the output signal from the lock-in amplifier (HF2LI, Zurich Instruments) ranging up to 10 Vpk. This is sufficiently strong for most of the strings we have fabricated except for the stoichiometric silicon nitride strings which are shorter than 100 μm due to their high tensile stress. A digital PLL consists of a phase detector, a digital loop filter and a digitally controlled oscillator as illustrated in Fig. 6.2(c). The phase detector compares the phase of the oscillator with the incoming reference signal, giving an output proportional to the difference in phase. This is then filtered to remove unwanted high-frequency components, and the output from the filter is used to control the frequency of the oscillator, locking it to the input signal. The lock-in amplifier determines the frequency of the AC signal coming from the laser Doppler vibrometer and stores the measured values with a sampling rate of up to 461000 samples/second. The sampling rate of 56.2 samples/second was used for the most of the measurements.

6.2 Photothermal Infrared Setups

The first photothermal IR setup was built based on the work by Wig *et al* [65] with a thermal IR source. The sensor chip was placed on a ring PZT with an inner diameter of 6 mm for IR radiation. An aluminium vacuum chamber provided a vacuum-tight electrical connection for actuation, a glass window for the optical readout and a 3 mm thick, uncoated potassium bromide IR window where the ring PZT was mounted. A thermal IR source of nichrome wire wound on a ceramic rod was used together with the interference filter wheel of a commercially available Foxboro Miran 1A-CVF spectrophotometer. The IR monochromator consists of an IR radiator that is focused onto a slit by an elliptical mirror. A variable-wavelength, band pass, filter wheel is positioned after the slit and is used to select a specific wavelength of the radiation. The filter wheel covers the wavelength range from 2.5 to 14.5 μm (from 690 to 4000 cm^{-1}) with a spectral resolution of approximately 0.05 μm at 3 μm (62 cm^{-1} at 3333 cm^{-1}), 0.12 μm at 6 μm (34 cm^{-1} at 1667 cm^{-1}), and 0.25 μm at 11 μm (21 cm^{-1} at 909 cm^{-1}) according to the manufacturer. The string was illuminated with monochromatic IR light with the chopper set at 1 Hz. The IR light from the source was focused onto the backside of string using a spherical mirror. Fig. 6.3 shows a schematic drawing and a photograph of the first photothermal setup.

The second photothermal setup was built in order to align a string in a more precise way. The sensor chip was mounted on a ring PZT with an inner diameter of 6 mm for IR radiation. An aluminium vacuum chamber (dimensions are provided in Appendix B) provides a vacuum-tight electrical connection for PZT, a glass window for the optical readout and a 2 mm thick zinc selenide window with an anti-reflective coating for the IR radiation from 3 to 12 μm (from 833 to 3333 cm^{-1}). Zinc selenide has been chosen

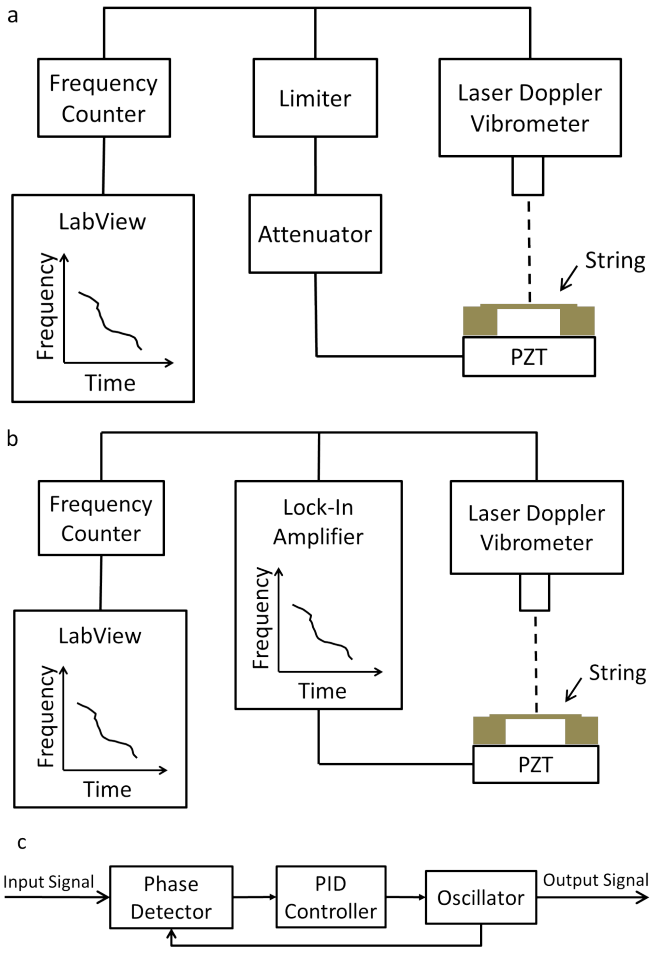

Figure 6.2: Schematic drawings of two ways to actuate a single frequency and to measure resonance frequency, (a) using a positive feedback loop and (b) using a phase-locked loop. (c) Block diagram of a phase-locked loop.

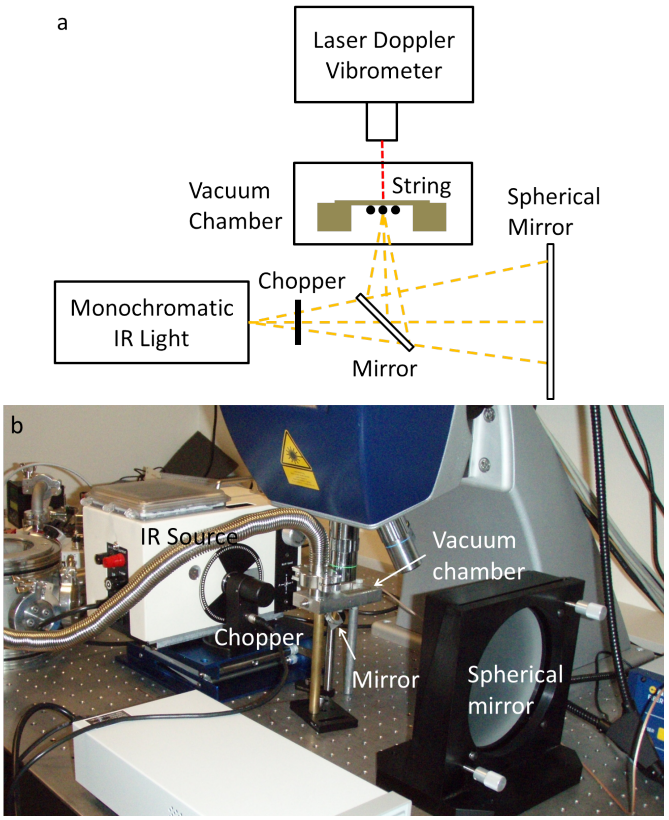

Figure 6.3: (a) Schematic drawing and (b) photograph of the first photothermal IR setup with a thermal IR source. The string is placed at the focal point of the spherical mirror. A chopper is used to obtain a frequency shift signal caused by the absorbed IR light.

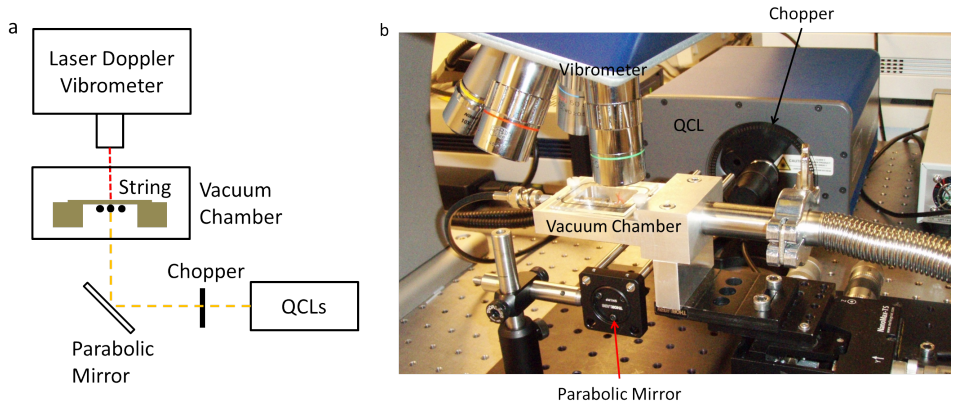

Figure 6.4: (a) Schematic drawing and (b) photograph of the second photothermal IR setup with QCLs. The string is placed at the focal point of a parabolic mirror. A chopper is used to obtain a frequency shift signal caused by the absorbed IR light.

for the IR window for its higher water resistance compared to potassium bromide. A widely tunable mid-infrared, pulsed laser source (an old model from 2013 of LaserTune, Block Engineering) was employed as the IR source. It consists of 4 quantum cascade laser (QCL) modules and a visible laser light for alignment. The laser tuning ranges from 925 cm^{-1} to 1920 cm^{-1}. The power of the QCLs can be varied by changing the duty cycle given by pulse width [ns]/pulse period [ns] which has a maximum value of 5.0% and a minimum value of a 0.625%. The synchronization data of the IR laser from QCLs was recorded and stored by the lock-in amplifier together with the resonance frequency data. The string was illuminated with IR light with the chopper set at 10 Hz to obtain frequency shifts. The IR light was focused on the backside of the string using an off-axis parabolic mirror. Fig. 6.4 shows a schematic drawing and a photograph of the second photothermal setup. The diameter of the focused IR light was estimated from the diameter of the focused visible laser light which could be seen using the optical microscope of the vibrometer. The diameter can vary depending on how well the light is focused on a string and the estimated diameter was approximately 25 µm. The diameter was also verified by SEM on a polymer sample as the polymer nanoparticles are rearranged in a denser manner where it has been irradiated with IR radiaton, which was measured to be approximately 20 µm.

6.3 Aerosol Sampling

All samples were collected on strings as nanoparticles. Aerosol was produced by either a single-jet nebulizer (TSI model 9302) or a constant output nebulizer (TSI model 3076). Both of them are instruments for nebulizing a liquid solution or a suspension. They produce droplets with a mean diam-

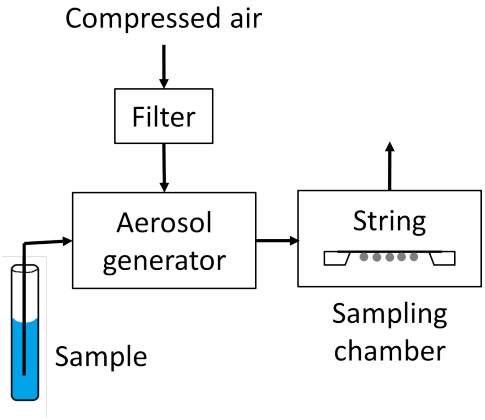

Figure 6.5: Experimental setup used for aerosol sampling. The air for the aerosol generation was supplied through a filtered air supply and the aerosol was produced with an aerosol generator from an aqueous solution.

eter of 0.3 µm. The difference is that the atomizer model 3076 consists of stainless-steel components, which can be used for a wider range of materials compared to the model 9302 having plastic components. In an atomizer, compressed air expands through an orifice to form a high-velocity jet, liquid is drawn into the atomizing section and is then atomized by the jet as know as Bernoulli's principle. Large droplets are removed by impaction on the wall opposite the jet and excess liquid is drained. The air for the aerosol was supplied through a filtered air supply (TSI model 3074) and the droplets were dried in a aerosol diffusion dryer using silica gel. The particle diameter of a water soluble substance is determined by the concentration of the substance, i.e. a 1 ppm sodium chloride solution gives sodium chloride nanoparticles with a peak diameter of 30 nm. The number of nanoparticles was counted by a miniature diffusion size classifier DiSCmini from Matter Aerosol AG, the pressure of the compressed air was adjusted using a pressure regulator and the flow rate was monitored by a mass flowmeter (TSI 4100 series). All samples were directly collected on the backside of strings using an efficient non-diffusion limited sampling method [76]. A schematic drawing of the aerosol sampling setup is depicted in Fig. 6.5.

For the experiments in Section 7.3.2, aerosol was generated from a 0.05 wt% aqueous solution with poly-vinylpyrrolidone (PVP, K30, Mw 40000 g/mol, Sigma-Aldrich) at 100 kPa and was deposited on a SiN string of 506 µm long, 3.0 µm wide and 157 nm thick for 60 seconds. The measured average diameter of the PVP nanoparticles was 29 nm and the particle number concentration was 3×10^6 particles/cm^3.

Titanium dioxide nanoparticles NM-104 (gift from Danish National Research Centre for Working Environment) were dispersed in ammonium acetate (Sigma-Aldrich) buffer at pH 4.3 for the experiments in Section 7.3.3.

The reason for using ammonium acetate buffer to disperse titanium dioxide nanoparticles is that titanium dioxide nanoparticles have an isoelectric point at pH≈7 which in turn causes agglomeration of dispersed nanoparticles near neutral pH [112, 113]. Titanium dioxide aerosol was generated from a 0.05 wt% titanium dioxide solution in a 0.44 wt% ammonium acetate buffer with a compressed air pressure of 100 kPa and was deposited on a SRN string of 512 μm long, 3 μm wide and 185 nm thick for 5 minutes. The measured average diameter of the titanium dioxide nanoparticles with ammonium acetate was 28 nm and the particle number concentration was 1.8×10^6 particles/cm^3. Ammonium acetate aerosol was generated from a 0.27 wt% ammonium acetate buffer at pH=4.7 with a compressed air pressure of 100 kPa and was deposited on a SRN string of 511 μm long, 5.5 μm wide and 185 nm thick for 40 minutes. The measured average diameter of the ammonium acetate nanoparticles was 11 nm and the particle number concentration was 5.5×10^5 particles/cm^3.

1,1-Dimethylbiguanide hydrochloride (metformin) and copper nitrate were purchased from Sigma-Aldrich and used without further purification. For the experiments in Section 7.4.1, the 200 μM metformin solution and 10 mM copper nitrate soultion were prepared using milliQ water. The copper-metformin complex solution was obtained by mixing 10 mM copper nitrate soultion and 200 μM metformin with the ratio of 1:100. Metformin aerosol was generated from the 200 μM metformin solution with a compressed air pressure of 120 kPa and was deposited on a stoichiometric silicon nitride string of 100 μm long, 500 nm wide and 100 nm thick for 5 minutes. Copper-metformin complex aerosol was generated from the 100 μM copper-metformin complex solution with a compressed air pressure of 120 kPa and was deposited on a SRN string of 112 μm long, 5.0 μm wide and 185 nm thick for 5 minutes.

Polymer mixtures for the experiments in Section 7.4.2 were prepared as the followings. Polyvinylpyrrolidone (PVP10, Mw 10000 g/mol) and polystyrene (PS) latex beads of a mean particle size of 100 nm (LB1, 10 wt%) were purchased from Sigma-Aldrich and used without further purification. The 1700 ppm PVP solution was prepared using milliQ water. The mixture solution of PS and PVP with the mass ratio PS/PVP of 1.0 was obtained by mixing 1700 ppm PVP soultion, 10% PS solution and milliQ water with the ratio of $60{:}1{:}1{\times}10^5$, that resulted in 1.0 ppm PVP and 1.0 ppm PS. The mixture solution of PS and PVP with the mass ratio PS/PVP of 0.50 was obtained by mixing 1700 ppm PVP soultion, 10% PS solution and milliQ water with the ratio of $120{:}1{:}1{\times}10^5$, that resulted in 2.0 ppm PVP and 1.0 ppm PS. The mixture solution of PS and PVP with the mass ratio PS/PVP of 0.67 was obtained by mixing 1700 ppm PVP soultion, 10% PS solution and milliQ water with the ratio of $78{:}2{:}1{\times}10^5$, that resulted in 1.3 ppm PVP and 2.0 ppm PS. The mixture solution of PS and PVP with the mass ratio PS/PVP of 2.3 was obtained by mixing 1700 ppm PVP soultion, 10% PS

solution and milliQ water with the ratio of 42:0.3:1×10^5, that resulted in 0.70 ppm PVP and 0.30 ppm PS. The four types of polymer mixures were deposited on 100 μm long, 5.0 μm wide and 100 nm thick SiN strings for 20 minutes. Aerosol of all the mixtures of PS and PVP was generated with a compressed air pressure from 100 to 120 kPa. The measured average particle number concentration was between 1.4×10^5 and 1.5×10^5 particles/cm^3 and the air flow was between 1.5 and 1.6 L/min. A SEM image of a mixture of PS and PVP nanoparticles on a SiN string of 99 μm long, 4.9 μm wide and 100 nm thick is shown in Fig. 6.5(b).

6.4 FTIR

A Spectrum 100T from PerkinElmer was used to obtain reference IR spectra in the wavenumber range from 650 to 4000 cm^{-1}. A silicon nitride film on a silicon wafer was mounted in a wafer holder and was measured using transmission mode. All the other materials were measured using attenuated total reflectance (ATR) mode with a diamond crystal. The measurement area of the ATR accessory is ∼2 mm and the penetration depth is 10 to 15 μm. PVP samples of ∼200 mg was necessary for a FTIR measurement with the ATR accessory. Same samples as in the photothermal IR spectroscopy were measured by FTIR except the PS sample for a practical reason, the latex beads were not measured by FTIR. PVP (K30, Mw 40000 g/mol, Sigma-Aldrich), PVP (K10, Mw 10000 g/mol, Sigma-Aldrich) and PS (Mw 280000 g/mol, Sigma-Aldrich) were measured by FTIR.

The thermal IR source with a wheel filter was calibrated by a Bomem Arid Zone FTIR spectrometer (Bomem MB-Series, Bomem inc.) using a detector of deuterated triglycine sulfate (DTGS) of a pyroelectric type with flat response curve and with a resolution of 2 cm^{-1}. The IR radiation from the thermal IR source was collimated using a parabolic mirror as shown in Fig. 6.6. The calibration was conducted on 2012-07-11.

6.5 Measuring IR Power

A thermal power sensor S302C from Thorlabs was used in order to obtain a power distribution of the IR laser together with a laser power and energy meter PM100USB from Thorlabs. The thermal power sensor covers the wavenumber range from 0.19 to 25 μm (from 526 to 52632 cm^{-1}) and the optical power range from 100 μW to 2 W with a resolution of 1 μW. The response time of the sensor from 0% to 90% is 3 seconds. The data was recorded at a sampling rate of 10 samples/second using PM100USB Control Software provided with the laser power and energy meter.

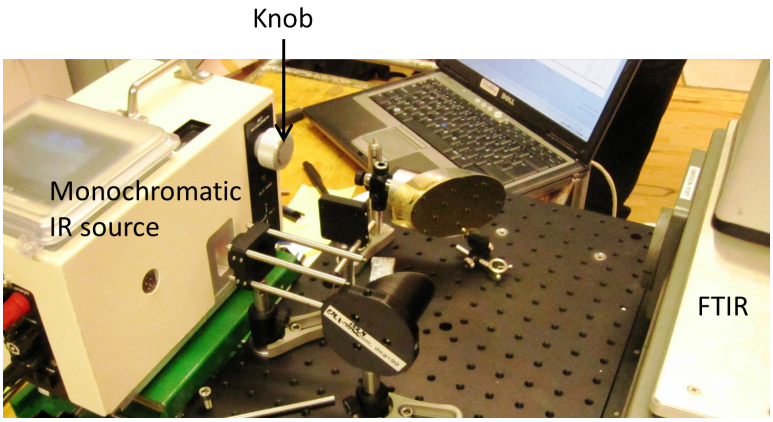

Figure 6.6: Experimental setup used to calibrate the Foxboro Miran 1A-CVF spectrophotometer. The IR radiation from the IR source was collimated using a parabolic mirror.

6.6 Summary

All resonance frequencies were optically read-out using a laser Doppler vibrometer at a pressure below 1.0×10^{-5} mbar. Strings were driven at the resonance frequency by means of a positive feedback or a phase-locked loop. The first photothermal IR setup was built using a thermal IR source combined with a filter wheel which was capable of scanning the wavelength range from 2.5 to 14.5 μm (from 690 to 4000 cm^{-1}). The second photothermal IR setup was built using QCLs which was capable of scanning the wavenumber range from 925 to 1920 cm^{-1}. The diameter of the IR laser was estimated to be approximately 20 μm by SEM.

All samples were directly collected on the backside of strings as nanoparticles generated from a liquid solution or a suspension. The materials deposited on strings are PVP, titaniums dioxide nanoparticles with ammonium acetate, metformin and its copper complex, and mixtures of PS and PVP with ratios PS/PVP between 0.5 and 2.3.

FTIR was used to obtain reference IR sepctra and to calibrate the thermal IR source with a wheel filter. A thermal power sensor was used to obtain the power distributin of QCLs.

Chapter 7

Results and Discussion

This chapter will be used to present the results obtained when investigating the two types of IR sources, the strings fabricated with two materials, and photothermal IR spectroscopy for a variety of applications. In the first section, the thermal IR source with a filter wheel is characterised using a FTIR and the QCLs are characterized using a thermal power sensor. The effect of changing string dimensions and absorbed power level is investigated, first via FEM simulations and then experimentally in the second section. Thermal relaxation in strings, response time of strings, and frequency stability are also discussed. The third section will present IR spectra of silicon nitride, PVP and titanium dioxide nanoparticles measured by photothermal spectrosocpy using the thermal IR source, and then the fourth section will present IR spectra of metformin, and binary mixtures of PS and PVP measured by photothermal spectroscopy using QCLs.

7.1 IR Source Characterization

7.1.1 Thermal

In a Foxboro Miran 1A-CVF spectrophotometer, a nickel-chrome alloy wire is used as its IR radiation source which can be electrically heated to 1100 K without severe oxidation [114]. In order to obtain more information on the instrument, we have calibrated the spectrophotometer with a FTIR as described in Section 6.4. Fig. 7.1 shows IR intensitiy of the broadband of the IR source plotted against wavenumber. It can be seen that the broadband of nickel-chrome alloy has its highest IR intensity around 2000 cm^{-1} and it ranges from 500 to 7500 cm^{-1}. The shape of the curve is close to the one for a blackbody at 1100 K, whose simulated IR spectrum is shown also in Fig. 7.1 [115], which agrees well with the literature [114]. The noise seen from 1300 to 2000 cm^{-1} is caused by the bending mode of water in a gas phase, which has a band center at 1594 cm^{-1} The noise seen from 3400 to 3950 cm^{-1} is caused by the symmetric and asymmetric stretching modes of

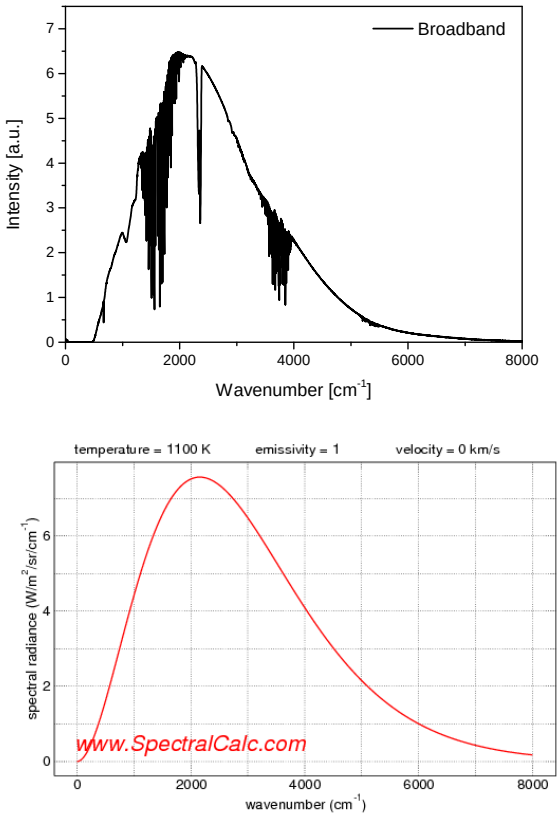

Figure 7.1: (Top) IR intensity of the broadband of the thermal IR source (nickel-chrome alloy) as a function of the wavenumber showing a highest IR intensity around 2000 cm^{-1}. The broadband ranges from 500 cm^{-1} to 7500 cm^{-1}. (Bottom) Simulated IR spectrum of a blackbody at 1100 K [115].

water in a gas phase, which has band centers at 3656 and 3755 cm^{-1}, respectively [116, 117]. The intensity drop between 2300 and 2400 cm^{-1} is caused by carbon dioxide molecules in the air.

The filter wheel covers the wavelength range from 690 to 4000 cm^{-1} with two overlapping regions that are located from 1250 to 1266 cm^{-1} and from 2222 to 2273 cm^{-1}. The intensity of of the IR source at 21 wavenumbers were measured: 690, 714, 769, 833, 909, 1000, 1111, 1250 and 1266 cm^{-1} in the first module, 1250, 1266, 1429, 1667, 2000, 2222 and 2223 cm^{-1} in the second module and 2222, 2500, 2857, 3333 and 4000 cm^{-1} in the third module. Fig. 7.2(a)(b)(c) show the measured data of the first module, the second module and the third module, respectively. The noise caused by water molecules is again seen in the monochromatic light at 1429 and 1667 cm^{-1} in module 2. The intensity of the monochromatic IR light between 1200 and 3000 cm^{-1} is relatively high and stable and the intensity at the rest of the

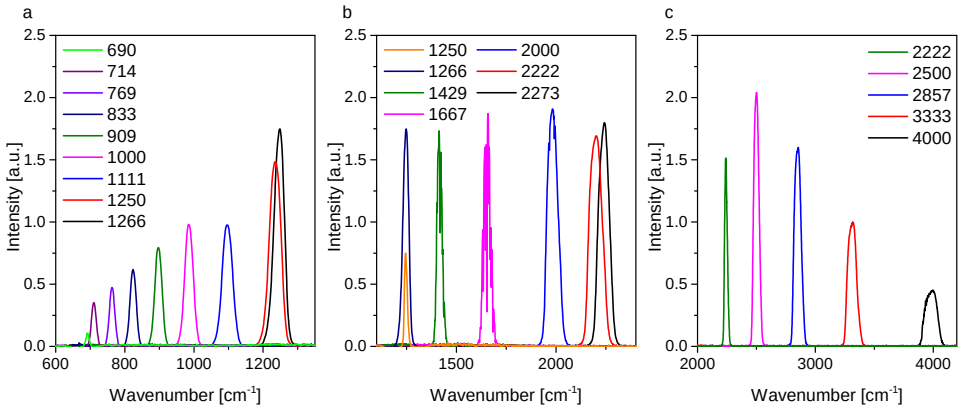

Figure 7.2: IR intensity of monochromatic IR light at 21 different wavenumbers. The intensity was measured at (a) 690, 714, 769, 833, 909, 1000, 1111, 1250 and 1266 cm^{-1} in the first module, (b) 1250, 1266, 1429, 1667, 2000, 2222 and 2223 cm^{-1} in the second module, and (c) 2222, 2500, 2857, 3333 and 4000 cm^{-1} in the third module of the Foxboro Miran 1A-CVF spectrophotometer.

wavenumbers follows the intensity curve of the broadband.

In order to assess how how correct this Foxboro Miran 1A-CVF spectrophotometer is, wavenumbers were measured against the standard FTIR spectrometer. The measured wavenumbers show some deviations compared to the ones in the standard FTIR spectrometer as all kinds of instruments do. The wavenumber deviations were calculated from the wavenumber with a highest intensity at 16 different wavenumbers. The wavenumber with a highest intensity at 1429 and 1667 cm^{-1} were estimated from the width of the spectra due to the absorption by gaseous water molecules. The knob of the instrument was turned manually to set a wanted wavenumber. All of the 3 modules show blue shifts when wavenumbers are smaller and move to red shifts with increasing wavenumbers as seen in Fig. 7.3(a). The largest red shift of 20.6 cm^{-1} was observed at 2222 cm^{-1} in module 2 and the largest blue shift of 17.0 cm^{-1} was observed at 2222 cm^{-1} in module 3. The repeatability of the instrument was investigated by rotating the knob to the line where the wavenumber indicated 2500 cm^{-1} from both directions and it was repeated 5 times. Fig. 7.3(b) shows that the maximum deviation is 1.5 cm^{-1}, which is much smaller than the deviations measured at 16 different wavenumbers over the whole measurement range.

7.1.2 QCL

The magnitude of the relative frequency shift for photothermal spectroscopy increases with increasing absorbed power according to Eq. 4.13. As the project progressed we replaced the thermal IR source with QCLs to improve the magnitude of the relative frequency shift by 3 orders of magnitude on

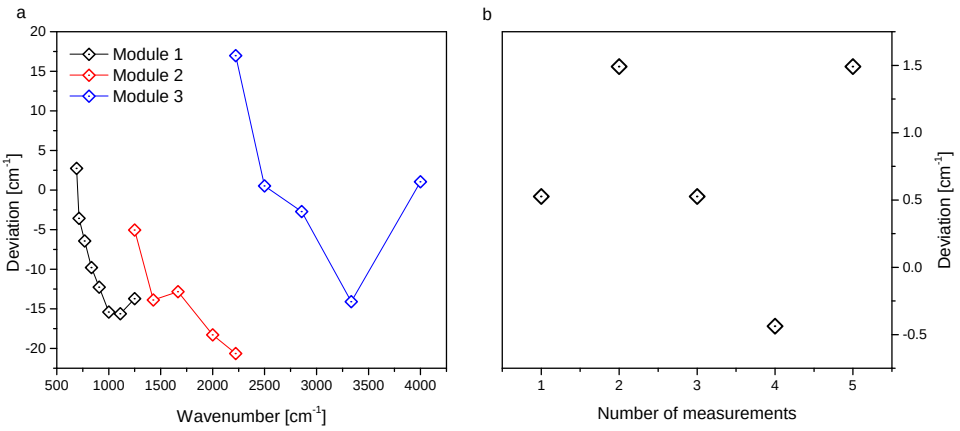

Figure 7.3: (a) Wavenumber deviations of the measured monochromatic IR light at 16 different wavenumbers compared to the wavenumber set by the knob on the instrument, showing the largest red shift of 20.6 cm^{-1} at 2222 cm^{-1} in the module 2 and the largest blue shift of 17.0 cm^{-1} at 2222 cm^{-1} in the module 3. (b) Wavenumber deviations of the measured monochromatic IR light at 2500 cm^{-1}. The knob was rotated to the both directions and the measurements were repeated 5 times. The maximum deviation is 1.5 cm^{-1}, which is much smaller than the deviations measured at 16 different wavenumbers over the whole measurement range.

average. The first QCL was demonstrated at Bell Laboratories in 1994 [118] and it is the only semiconductor laser source which operates at room temperature in the mid-infrared range [119]. Razeghi reported that an output power of 3.4 W at an emitting wavenumber of 2083 cm^{-1} was demonstrated from a single device operating in continuous wave at room temperature [120].

Scanning IR power of a widely tunable mid-infrared laser source LaserTune was measured using a thermal power sensor. The LaserTune was purchased in 2013 and the currently commercially available model in 2014 has a different specification such as a wavenumber range from 769 to 1852 cm^{-1} in comparison to our model from 925 to 1920 cm^{-1}. The IR source consists of 4 laser modules as seen in Fig. 7.4(a). It can be seen that the second module has 2 power peaks and the third module has 3 power peaks while modules 1 and 4 have one power peak each. IR power of up to 3 mW was measured at module 1 and 2. Modules 3 and 4 emit IR light at the wavenumbers where water molecules in air interfere. No IR is emitted at the vertical lines seen in the figure which is caused by the rotation of the grating device. No IR is emitted while the grating rotates. Fig. 7.4(b)(c) show close-ups of the IR power distribution of the module 1 and 4, respectively. It can be seen that the response time of the thermal power sensor S302C from Thorlabs described in Section 6.5 is too slow to follow the changes in the IR laser power when there is no IR radiation. It can also be seen that the time necessary for the grating to rotate changes in the module 1, a shorter time up to 990 cm^{-1} and it takes a longer time after that. The effect of the water vapor in the

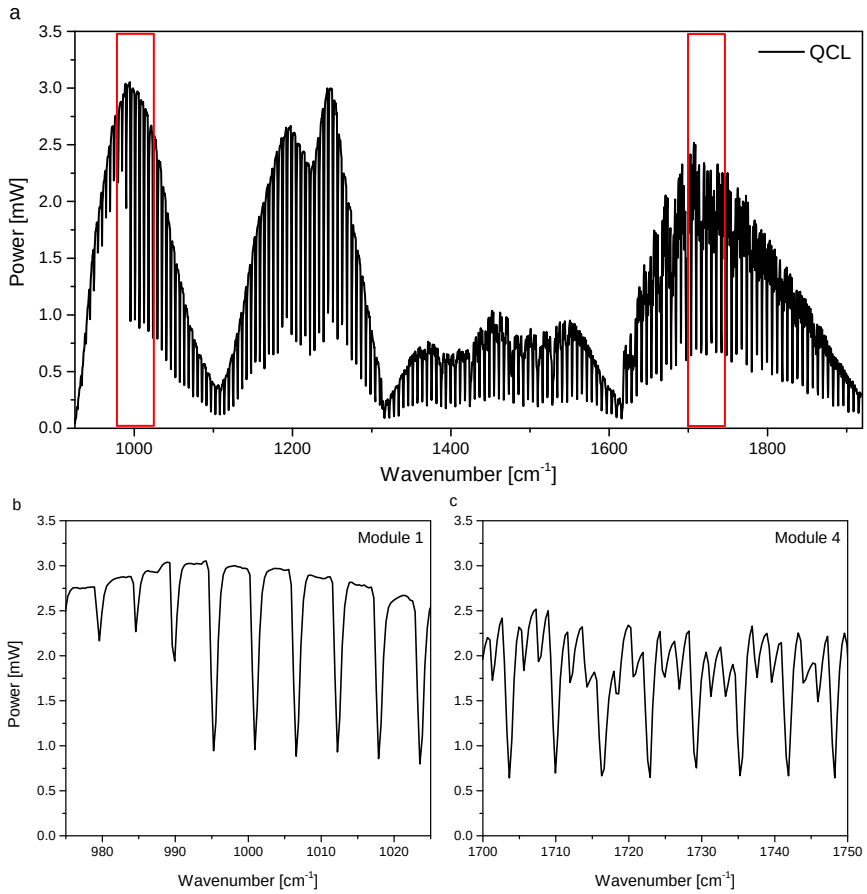

Figure 7.4: (a) IR power of QCLs as a function of wavenumber, showing 4 QCL modules. The vertical lines are caused by the rotation of the grating device. (b)(c) Close-ups of the IR power of the module 1 and 4, respectively. The response time of the thermal power sensor is too slow to follow the changes in the IR laser power.

air is clearly seen in Fig. 7.4(c).

Comparing the overall performance of the two types of IR sources, the filter wheel of the thermal IR source Foxboro Miran 1A-CVF covers the whole mid-infrared range while the QCL IR source covers only a part of the fingerprint region (600-1500 cm^{-1}) and most of the double bond region (1500-2000 cm^{-1}) [121]. Regarding the IR power, the thermal IR source was calculated to be 14 nW at 904 cm^{-1} [122] and QCL showed 3.0 mW at 1000 cm^{-1}, which is 5 orders of magnitude as powerful as the thermal IR source. The broad range of thermal IR source will be used to analyse even the triple bond region (2000-2500 cm^{-1}) and the X-H stretching region (2500-4000 cm^{-1}) such as O-H stretching [121]. The powerful QCL will be used to analyse a smaller amount of samples. Photothermal IR spectroscopy using these IR sources will be demonstrated later in this chapter.

7.1.3 Summary - IR Source

The thermal IR source, Foxboro Miran 1A-CVF spectrophotometer, has its highest IR intensity around 2000 cm^{-1} and it ranges from 500 to 7500 cm^{-1}, whose shape of the broadband curve is close to the one for a blackbody at 1100 K. The filter wheel covers the wavelength range from 690 to 4000 cm^{-1} with two overlapping regions that are located from 1250 to 1266 cm^{-1} and from 2222 to 2273 cm^{-1}. The largest shift of 20.6 cm^{-1} was observed at 2222 cm^{-1} against a calibrated FTIR.

The thermal IR source was replaced with a widely tunable mid-infrared laser source LaserTune to improve the magnitude of the relative frequency shift. This IR laser source has four modules and covers a wavenumber range of 925 to 1920 cm^{-1}. IR power of up to 3 mW was measured at module 1 and 2. The thermal IR source has a advantage of covering the whole mid-infrared range while the IR laser source is a powerful tool when analysing a smaller amount of samples.

7.2 String Characterisation

The string-based photothermal spectroscopy relies on changes in its resonance frequency as a function of absorbed power. The magnitude of the relative frequency shift of a string is, as described in Section 4.2, determined by its length, cross-sectional area, thermal expansion coefficient, Young's modulus, built-in tensile stress, thermal conductivity, and absorbed power by the string. In this section, the effect of string dimensions, irradiation power and source is investigated, first by FEM simulations and then experimentally. Stress relaxation in strings, response time of strings, and frequency stability are also discussed in this section. Further, the power resolutions of strings with different lengths and different materials are presented.

7.2.1 FEM Simulations

Finite Element Method (FEM) simulations have been used to investigate how induced frequency shifts are related to the string dimensions, the level of absorbed power and the thickness of an additional layer on a string. Five sets of simulations have been made: the influences of string width, thickness and length, the influence of level of absorbed heat in a string, and the influence of an added gold layer on a string. The simulations have been made using the FEM simulation software COMSOL 4.2 and COMSOL 4.3a.

Figure 7.5 shows the comparison of the analytic model given by Eq. 4.14 and the FEM simulation. In the simulations, an initial strain of 8.0×10^{-4} is introduced to the strings. The material properties for the SRN string used in the simulations are shown in Table 7.1. To simplify the simulations it is only the strings that are simulated and the influence from the frame

Table 7.1: Material properties of silicon nitride and gold used for the FEM simulations and for calculations with the analytical models.

	SRN	SiN	Gold
Young's modulus [GPa]	250	320	70
Thermal expansion coefficient [ppm/°C]	2.3	2.0	14.2
Thermal conductivity [W/(m·°C)]	20	2.1	317
Pre-stress [MPa]	200	1120	0
Mass density [kg/m^3]	3100	3200	19300
Heat capacity [J/(kg·°C]	700	711 [123]	129
Emissivity	1	1	1

is neglected. The temperature of the anchor regions is fixed. Temperature induced changes in Young's modulus, mass density, and thermal expansion coefficient are also neglected. In order to evaluate the analytical model and results from the FEM simulations, relative frequency shifts are calculated from the analytical model Eq. 4.14 using the same material properties, as a function of the width, thikness and length of a string, and also as a function of the power of absorbed IR radiation.

In the first set of simulations, the influence of string width is investigated by changing the width in steps of 5 µm from 10 µm to 50 µm. Fig. 7.5(a) shows the relative frequency shift of a string as a function of the inverse of string width. The relative frequency shift is increasing linearly with the inverse of the string width. In the second set of simulations, the influence of string thickness is investigated by changing the thickness in steps of 20 nm from 150 nm to 350 nm. Fig. 7.5(b) shows the relative frequency shift of a string as a function of the inverse of string thickness. The relative frequency shift is increasing linearly with the inverse of the string thickness as well as the inverse of the string width.

In the third set of simulations, the influence of string length is investigated by changing the length in steps of 50 µm from 200 µm to 600 µm. Fig. 7.5(c) shows the relative frequency shift of a string as a function of the length of the string. The relative frequency shift is increasing linearly with the increasing string length. In the fourth set of simulations, the resonance frequency is simulated when different levels of heat is absorbed in the center of a string. The heat absorbing area is circular and it has a diameter of 6 µm. The power of the absorbed heat is varied from 60 nW to 6 µW. Fig. 7.5(d) shows the relative frequency shift of a string as a function of the power of

absorbed radiation. The relative frequency shift is increasing linearly with the increasing power of absorbed radiation.

The analytical expression given in Eq. 4.14 is in a good agreement with the results from the FEM simulations. The small differences in the relative frequency shift can derive from the difference in the dimensions of heat absorbing area in the string. For the analytical expression, it is assumed that the string is heated by an applied power distributed evenly in a cross-section of the string at the center of the length. For the FEM simulations, on the other hand, a circle with a diameter of 6 μm is assumed. The small differences can also derive from the heat loss via radiation in the FEM simulations, while the analytical model does not include it. The emissivity of silicon nitride has been reported to be 0.90 to 0.98 in the infrared region by Ravindra *et al* [124] compared to 1 which is used in the simulations. In order to investigate the effect of emissivity, a pair of simulations have been performed. Using a string of 500 μm long, 5 μm wide and 200 nm thick, the resonance frequency is simulated when emissivity is 0 and 1 with the power of absorbed heat of 1 μW. The relative frequency shift for the emissivity of 0 and 1 are calculated to be 4.471×10^{-3} and 4.140×10^{-3}, respectively. Using the emissivity of 0 instead of 1, thus, has increased the relative frequency shift by 8.0%. It has been also calculated that using the analytical model instead of the simulation with the same parameters as above, has increased the relative frequency shift by 8.7%. From these two comparisons, it can be seen that the emissivity plays the main roll for the small differences in the relative frequency shifts.

Adding an extra layer of another material on a string could be significant for functionalizing the surface to attract specific molecules, or to add a material that tailors the optical or thermal properties of the string. For example, gold-coated mirrors are usually used for the optical setups for the mid-infrared range because it reflects more than 95% of the incident light over the whole mid-infrared range. Gold is also one of the most common surfaces to immobilize bio-molecules. More importantly it would be possible to readout electrically using a gold layer as a strain gauge on a string [87,125]. Thus, the resonance frequency of a silicon nitride string with an additional gold layer is simulated. The material properties for the gold layer used in the simulations are shown in Table 7.1.

In the fifth type of simulations, the resonance frequency of a SRN string with a gold coating is simulated. The thickness of the gold coating is changed in steps of 10 nm from 0 nm to 70 nm. Fig. 7.6 shows the relative frequency shift of a string with a gold coating determined by FEM and by the analytical expression given in Eq. 4.22 as a function of the gold coating thickness on a string. The relative frequency shift is decreasing with the increasing thickness of the gold coating. The analytical expression given in Eq. 4.22 is in a good agreement with the results from the FEM simulations.

Polished gold surface has an emissivity of 0.025 while unpolished gold sur-

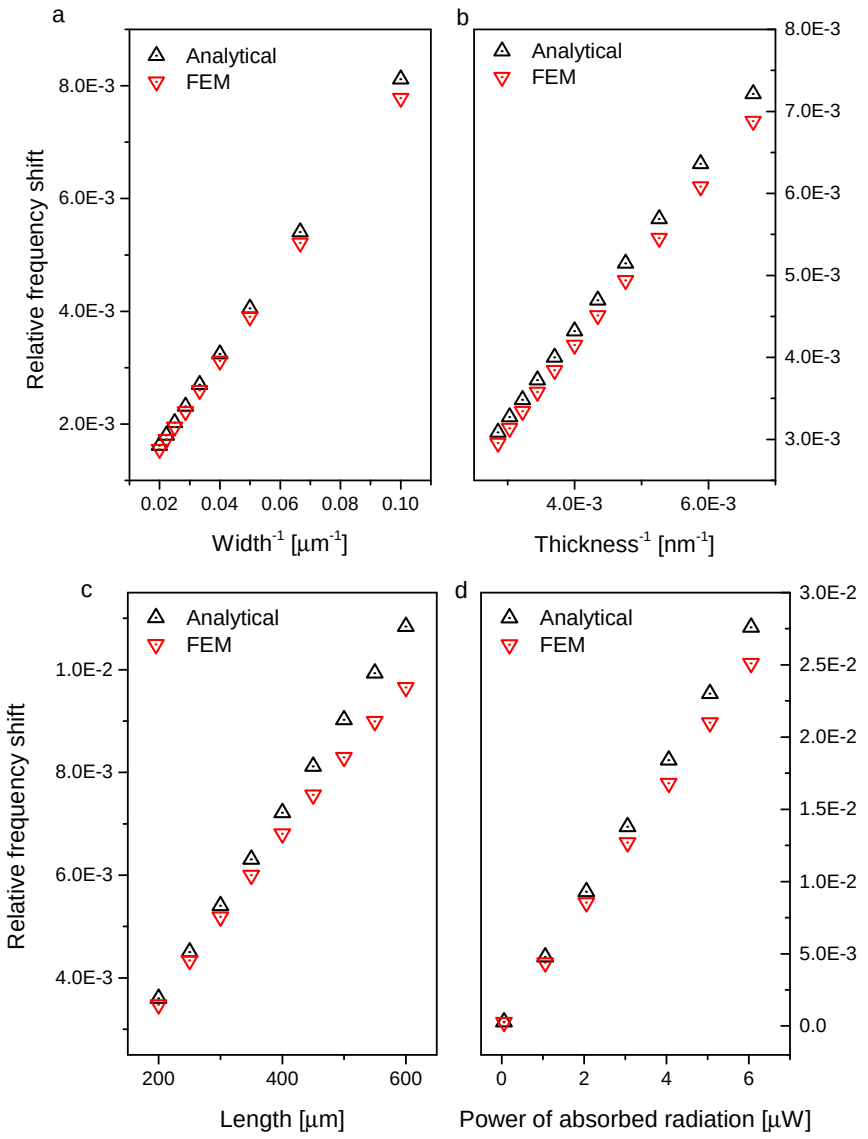

Figure 7.5: Relative frequency shift of strings determined by FEM and by the analytical expression given in Eq. 4.14. (a) Relative frequency shift of a 300 µm long and 200 nm thick SRN string with an absorbed power of 6 µW as a function of the inverse of the string width. (b) Relative frequency shift of a 300 µm long and 15 µm wide SRN string with an absorbed power of 6 µW as a function of the inverse of the string thickness.(c) Relative frequency shift of a 15 µm wide and 200 nm thick SRN string with an absorbed power of 6 µW as a function of the length of the string. (d) Relative frequency shift of a 500 µm long, 5 µm wide and 200 nm thick SRN string as a function of the power of the absorbed radiation.

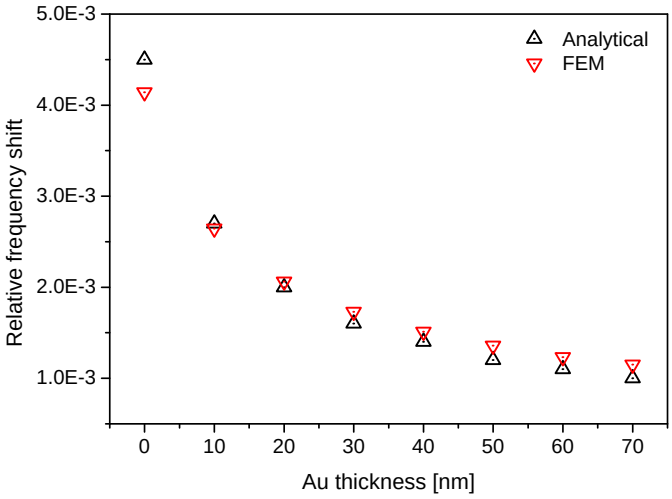

Figure 7.6: Relative frequency shift of a 500 µm long, 5 µm wide and 200 nm thick SRN string with a gold coating determined by FEM and by the analytical expression given in Eq. 4.22 as a function of the gold coating thickness. A heat source is positioned at the center of the string with an absorbed power of 1 µW.

face gives an emissivity of 0.47 [126]. In the case of micro- and nanostrings, gold layer is often deposited by electron beam or sputtering. The emissivity of 1000 nm thick, sputtered gold film has been reported to be around 0.2 for the infrared region of 3 to 14 µm (714 to 3333 cm^{-1}) [127]. As a lower emissivity gives a larger relative frequency shift, the actual relative frequency shift of a silicon nitride string with an gold coating is likely to be slightly larger than that from the simulations.

According to these simulations which agree well with the analytical model, the optimal dimensions for the string for photothermal IR spectroscopy are long, narrow and thin within a reasonable range for a chosen readout method. A higher power gives a larger frequency shift also. A gold layer on a silicon nitride string can be a significant importance for bio-applications even though it decreases the relative frequency shift.

7.2.2 Experimentally Determined Frequency Response

The power of the readout laser in the laser-Doppler vibrometer can be varied between ∼1.9 µW to ∼200 µW when using the 20× microscope objective [128]. The power of the QCLs can also be varied by changing the duty cycle which has a maximum value of 5.0% and a minimum value of a 0.625%. Using the readout laser and the QCLs, the effect of local heating and its sudden changes can be explored. The temperature of a string increases when the readout laser or QCL is focused onto it. The position of the laser spot on the string has an influence on the relative frequency shift magnitude. The frequency shift decreases when the laser spot is moved from the center point

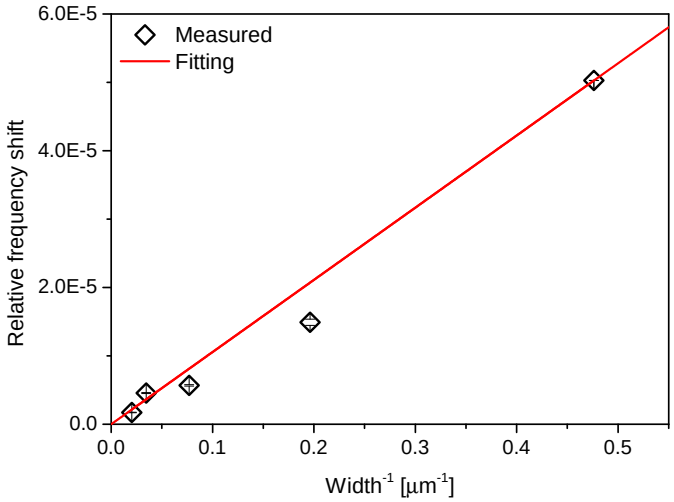

Figure 7.7: Relative frequency shift of a 214 μm long and 61 nm thick SiN string determined experimentally as a function of the inverse of the string width. A helium-neon laser is used as the readout laser which operates at at 633 nm. The readout laser was positioned at the center of the string with a laser power changed instantly from 1.9 μW to 200 μW and back with 30 seconds' intervals. The error bars show the standard deviation of 3 measurements.

of the string towards one of the anchor regions since more heat is dissipated into the silicon frame. The laser spot was placed at the center of strings in the following experiments.

Readout Laser

Fig. 7.7 shows relative frequency shift of SiN strings determined experimentally as a function of the inverse of the string width. The measurement was repeated 3 times and the average of the relative frequency shifts and the standard deviation were calculated from the measurements. It can be seen that the relative frequency shift is increasing linearly with the inverse of the string width, which is in a good agreement with the analytical model and the FEM simulations as shown in Fig. 7.5(a). The red line shows a linear fitting with an intercept at 0. From the slope of the fitted line and the Eq. 4.14, the absorbed power is extracted to be 1.8 nW, which is approx. 10 ppm of the readout laser power.

Fig. 7.8 shows relative frequency shift of two sets of strings that have similar length, similar width and different thickness, determined experimentally and plotted as a function of the inverse of the string thickness. It can be seen that the relative frequency shift is increasing with the inverse of the string thickness in the both sets of the strings, which is in a good agreement with the analytical model and the FEM simulations shown in Fig. 7.5(b). Linear fittings have been performed with an intercept at 0 in the same way

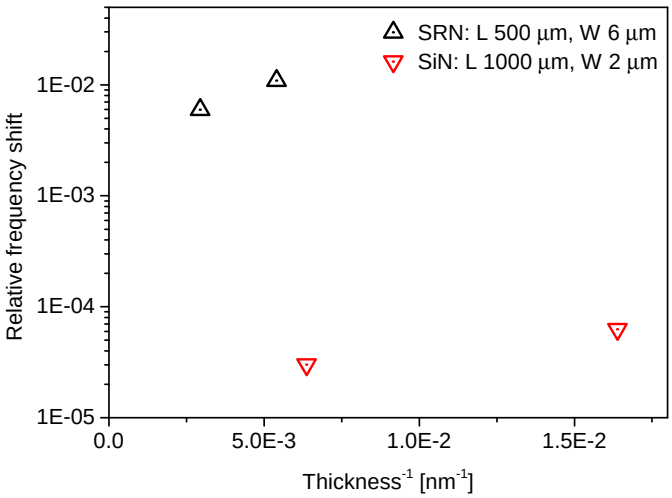

Figure 7.8: Relative frequency shift of 2 sets of strings determined experimentally and plotted as a function of the inverse of the string thickness. The first set is SRN stirngs with a length of 509 µm, a width of 5.5 µm and a thickness of 185 nm, and with a length of 505 µm, a width of 6.7 µm and a thickness of 43 nm. The second set is SiN strings with a length of 1014 µm, a width of 2.1 µm and a thickness of 61 nm ring, and with a length of 1012 µm, a width of 2.0 µm and a thickness of 157 nm. The readout laser at a wavenumber of 633 nm was positioned at the center of the string with a laser power changed instantly from 1.9 µW to 200 µW and back with 30 seconds' intervals.

as in Fig. 7.7. From the slope of the fitted lines and the Eq. 4.14, the absorbed power is extracted to be 2.7 µW for the SRN strings and 0.46 nW for the SiN strings. Considering the extracted absorbed power of 1.8 nW from Fig. 7.7, it can be deduced that SRN absorbs the red light at 633 nm 3 orders of magnitude more than SiN.

Fig. 7.9 shows relative frequency shift of SRN strings determined experimentally as a function of the string length. The measurement was repeated 3 times and the average of the relative frequency shifts and the standard deviation were calculated from the measurements. The red line shows a linear fitting with an intercept at 0. It can be seen that the relative frequency shift is increasing linearly with the string length, which is in a good agreement with the analytical model and the FEM simulations as shown in Fig. 7.5(c). From the slope of the fitted line and the Eq. 4.14, the absorbed power is extracted to be 2.3 µW, which is approx. 1% of the readout laser power. R^2 for the fitting, however, is 0.94 and it can be seen that the 109 µm long string has given a far smaller relative frequency shift compared to the fitted value. The reason for the smaller relative frequency shift can be explained by the smallest length which leads to faster dissipation of the heat.

The extracted absorbed power of 2.3 µW by SRN strings from Fig. 7.9 is in a good agreement with that of 2.7 µW from Fig. 7.8 while the extracted absorbed power of 1.8 nW by SiN string from Fig. 7.7 is in a relatively

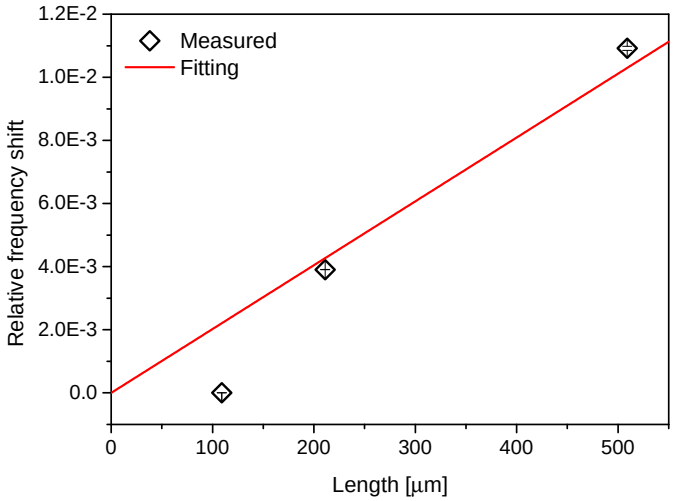

Figure 7.9: Relative frequency shift of 5.5 μm wide and 185 nm thick SRN strings determined experimentally as a function of string length of 109, 211 and 509 μm. The readout laser at a wavenumber of 633 nm was positioned at the center of the string with a laser power changed instantly from 1.9 μW to 200 μW and back with 30 seconds' intervals. The measurement was repeated 3 times and the error bars show the standard deviation.

good agreement with that of 0.46 nW from Fig. 7.7. The difference in the readout laser absorption between SRN and SiN can give a large effect on the frequency stability since this photothermal IR spectroscopy is optically readout using the visible laser of the vibrometer.

IR Laser

Fig. 7.10 shows relative frequency shift of a SRN string determined experimentally as a function of IR power in terms of duty cycle. The IR laser used in this study can irradiate with the maximum duty cycle of 5.0%. The IR laser at a wavenumber of 1495 cm^{-1} was positioned at the center of the string with the laser switched on and off with a duty cycle of 0.625, 1.56, 3.44, and 5.0% with 1 minute's intervals. The red line shows a linear fitting with an intercept at 0. It can be seen that the relative frequency shift is increasing linearly with the increasing IR power, which is in a good agreement with the analytical model and the FEM simulations as shown in Fig. 7.5(d). The actual absorbed power is calculated to be 384 nw from the relative frequency shift of 1.76×10^{-3} at a duty cycle of 5.0% while the power of QCL at 1495 cm^{-1} is measured to be 701 μW. Although it would have been a better comparison to do these measurements with IR light around 900 cm^{-1} where there is a Si-N bond absorption, it was not possible due to the too large frequency shift for the current measurement setup.

It is not always possible to readout a wanted string. It can be due to the dimensions of a string, the design of a chip, or the string material. It seems

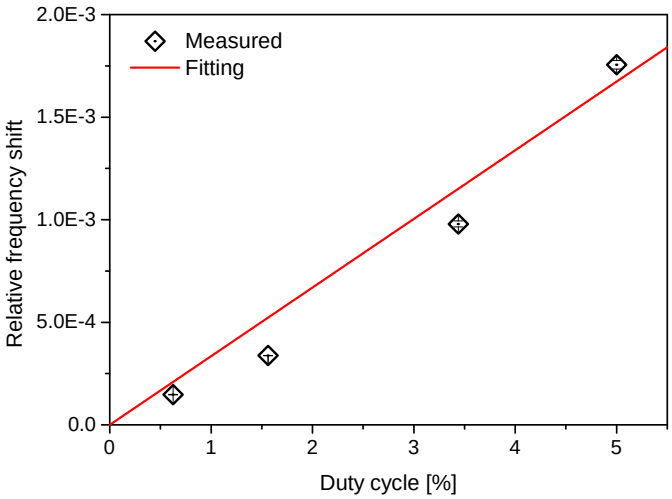

Figure 7.10: Relative frequency shift of a 509 µm long, 5.4 µm wide and 185 nm thick SRN string determined experimentally as a function of IR power in terms of duty cycle. The IR laser at 1495 cm^{-1} was positioned at the center of the string with a laser power switched on and off with a duty cycle of 0.625, 1.56, 3.44, and 5.0%. The measurement was repeated 3 times and the average of the relative frequency shifts and the standard deviation were calculated from the measurements. The error bars show the standard deviation.

that a relatively thinner string, i.e. thinner than 100 nm, is surely more sensitive as a sensing element and at the same time it is more sensitive to contaminants. This makes thinner strings more difficult to be readout in a laboratory environment than in a cleanroom environment. The width of a string plays a role in the reflection of the readout laser, which is detected by the vibrometer as described in Section 6.1. Having a width smaller than the diameter of the laser spot of approximately 6 µm, the amount of reflected readout laser can be too little for a stable measurement. The amount of reflected light can be increased by increasing the readout laser power which can in turn diminish the noise level despite a higher readout laser power, which will be discussed in Section 7.2.5. The maximum readout laser power was necessary for the strings with a width narrower than 1 µm.

As mentioned in Section 6.1, there is a more suited method to actuate a single frequency depending on the length of a string. A longer string, i.e. longer than 400 µm, is more suited to be actuated at a single frequency using the positive feedback loop than a shorter string. The PLL handles a shorter string, i.e. down to 100 µm long, without a complication but a string shorter than 100 µm becomes an issue due to the limitation in the driving force. Regarding the chip design, strings not to close to each other such as the design shown in Fig. 5.8(a) leads to a smaller risk of crosstalks from other strings on the same chip than many strings close to each other such as the design in Fig. 5.8(b). Reflectivity changes depending on the material of a string or the coating of a string. For example, a gold coated silicon nitride

string reflects the readout laser more than a bare silicon nitride string, which enables a measurement with less noise. From a practical point of view, it is recommended for a string to have a minimum thickness of 100 nm, a minimum width of 1 μm, and a minimum length of 100 μm with a chip design of strings not too close to each other when reading out optically using the vibrometer and actuating a single frequency using the PLL.

7.2.3 Thermal Relaxation

We have observed some variations in the rapid shift and relaxation patterns after changing the heat input level, depending on the string dimensions and materials. To investigate these further, resonance frequencies of silicon nitride strings of different width, different thickness, different length, and different materials have been measured as a function of time when the power of the readout laser was changed from 1.9 μW to 200 μW and back with 30 seconds' intervals during the measurement. To calculate and discuss the degree of relaxation, resonance frequencies of silicon nitride strings of different thickness and different materials have been measured for 120 seconds as a function of time when the power of the readout laser was changed from 200 μW to 1.9 μW.

Fig. 7.11 shows relative resonance frequency of SiN strings as a function of time to investigate the rapid shift and relaxation patterns in terms of the influence of string width and thickness. The resonance frequency shows a rapid shift after an instant change in the power of the laser. This is followed by a decaying shift of the resonance frequency. In Fig. 7.11(a) the strings have same length, same thickness, and different widths of 2.1 μm and of 49 μm. The 49 μm wide string shows 1/50 of the instant relative frequency shift of that of the 2.1 μm wide string instead of 1/23 according to Eq. 4.14. This can be explained by the difference in the thermal resistance of the strings. As a string with a smaller cross-sectional area would exhibit a higher thermal resistance and the heat is, thus, transferred slower through the string towards the silicon support. With the sampling rate of the frequency counter ∼172 ms, the 49 μm wide string is likely to have experienced a larger instant frequency shift and then the decaying shift has counteracted the instant shift within two measurement points by the frequency counter.

Fig. 7.11(b) shows the the case of varied width instead of thickness, measuring the frequency shift of two SiN strings with similar length, similar width and different thickness of 61 nm and 157 nm. The 157 nm thick string shows 47% of the instant relative frequency shift of the 61 nm thick string which is relatively close to the calculated value of 38% from the analytical model. It can be because the difference in the dimensions between these two strings is not as extremely as the case in Fig. 7.11(a). This measurement results will be, thus, used to discuss the variation in the relaxation behaviour.

It can be seen that the general tendency in Fig. 7.11(a)(b) is that the resonance frequency is decreasing after 3 cycles of laser power changes. This can be explained by the heat constantly being pumped into the string even when the laser power is as low as 1.9 μW. This constant heat input leads to a lowered relative frequency shift according to Eq. 4.14.

The average magnitudes of 4 relaxation behaviours for the 61 nm thick string and the 157 nm thick string, compared to the magnitude of the rapid shift directly before the relaxation are calculated to be 89% and 55%, respectively, from the measurements shown in Fig. 7.11(b). These numbers are averages of both from 1.9 μW to 200 μW and back and thus do not contain the general frequency decrease by the constant heat input of 1.9 μW. The thinner string exhibits higher magnitude of relaxation than the thicker string after 30 seconds.

Fig. 7.12 shows relative resonance frequency of the same strings that have been used in Fig. 7.11(b), showing the relaxation behaviour after the rapid shift when the power of the laser was changed from 200 μW to 1.9 μW instantly. Fig. 7.12(a)(b) have been fitted by two exponential decaying terms and one exponential decaying term, respectively. As the definition of relaxation time τ is to reach 63.2% of the overall change, the expected overall change is extracted from the fits and then the time necessary for the 63.2% of the overall change is also extracted from the fits. Assuming $F(\infty)$ is the 100% relaxation, the 61 nm thick string would experience 255 ppm relative frequency shift as a result of relaxation, which corresponds to 409% of the rapid shift of 62.3 ppm. In the same way, the 157 nm thick string would experience 79.6 ppm relative frequency shift as a result of relaxation, which corresponds to 265% of the rapid shift of 30.1 ppm. The relaxation time τ has been extracted to be 160 seconds for the 61 nm thick string and 128 seconds for the 157 nm thick string.

The progress of relaxation for the 61 nm thick string is calculated to be 15% after 10 seconds, 37% after 60 seconds, and 54% after 120 seconds. For the 157 nm thick string, the progress of relaxation is calculated to be 11% after 10 seconds, 38% after 60 seconds, and 61% after 120 seconds. As the thinner string would exhibit a higher magnitude of total relaxation compared to the rapid shift, it makes sense that the thinner string exhibits a larger initial relaxation progress within the first 10 seconds after the rapid shift. The progress of relaxation of the thicker string, however, exceeds that of the thinner string by the time of 60 seconds and continues to progress faster. This can be explained by the higher thermal conductivity in the thicker string. The shorter stabilization time of the thicker string is more desirable for photothermal spectroscopy.

Fig. 7.13(a) shows the relative resonance frequency of two SiN strings that have same width, same thickness, and different lengths of 214 μm and of 1014 μm. Here we see that the general tendency of the resonance frequency with the 214 μm string is increasing after 3 cycles of laser power changes

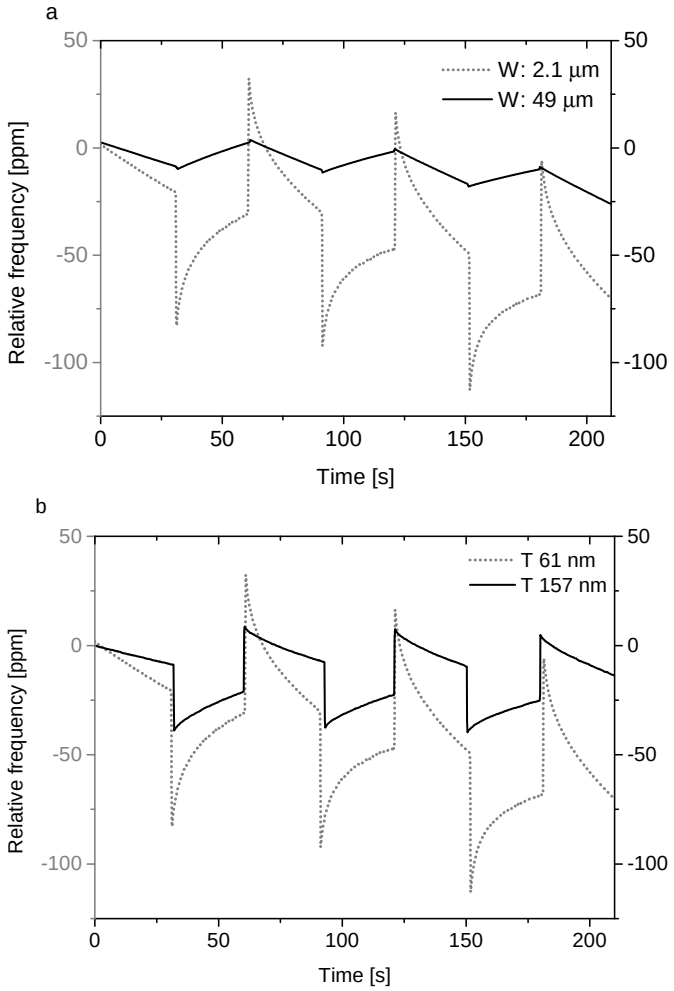

Figure 7.11: (a) Influence of string width: Relative resonance frequency of two SiN strings that have a length of 1014 µm, a thickness of 61 nm, and different widths of 2.1 µm and of 49 µm, when the power of the laser was changed between 1.9 µW and 200 µW with 30 seconds' intervals. (b) Influence of string thickness: Relative resonance frequency of a 1014 µm long, 2.1 µm wide and 61 nm thick SiN string and a 1012 µm long, 2.0 µm wide and 157 nm thick SiN string, when the power of the laser was again changed between 1.9 µW and 200 µW with 30 seconds' intervals.

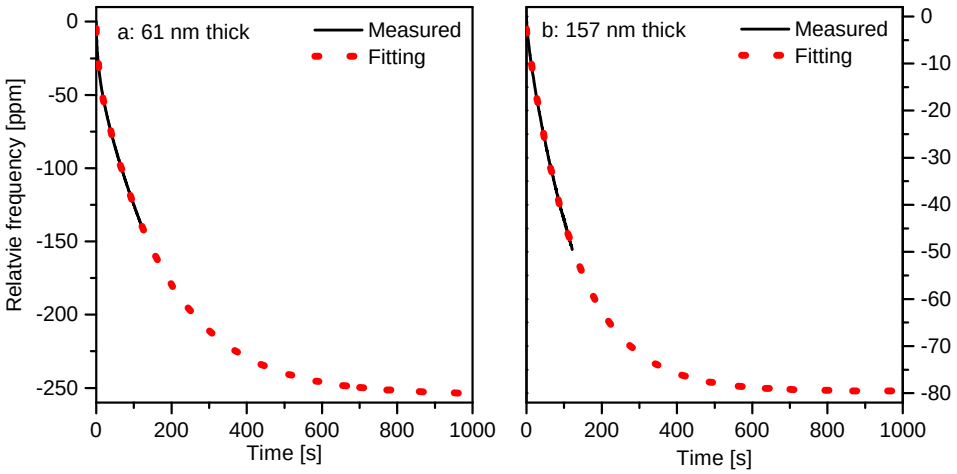

Figure 7.12: Relative resonance frequency of (a) a 1014 µm long, 2.1 µm wide and 61 nm thick SiN string and (b) a 1012 µm long, 2.0 µm wide and 157 nm thick SiN string (the same strings that have been used in Fig. 7.11(b)), showing a relaxation behaviour for 120 seconds after a quick shift when the power of the laser was changed from 200 µW and 1.9 µW instantly.

even though it receives a constant heat input. As the silicon frame expands due to the constant heat input, the hole length is reduced as much for the 214 µm long string's frame and for the 1014 µm string's frame. Due to this phenomenon the 214 µm string would, thus, experience approx. 5 times as much tensile stress caused by the expansion of the silicon frame as the 1014 µm string. Higher tensile stress increases the resonance frequency of a string and this could be the explanation for the general increase in the resonance frequency for the 214 µm long string.

Fig. 7.13(b) shows the relative resonance frequency of two SRN strings that have same width, same thickness, and different lengths of 211 µm and of 509 µm. It can be seen that the relaxation level of SiN strings are distinct from that of SRN strings. SiN strings show a longer relaxation time with a higher degree of relaxation behaviour while SRN strings show much smaller degree of relaxation behaviour. This can be explained by the difference in the thermal conductivity of SRN and SiN. As summarized in Table 5.1, SRN exhibits a wide range of thermal conductivity from 2.5 to 24 W/(m·K) due to the undefined ratio between silicon and nitrogen while SiN gives 2.1 W/(m·K). The ratio of Si/N can vary from 0.77 to 1.14 compared to 0.75 of SiN, which corresponds to 3 to 52% more silicon in SRN [129]. The shorter stabilization time of the SRN string is more desirable for photothermal spectroscopy. A chopper with an appropriate frequency would be helpful for this relaxation issue in order to obtain only the value of the first quick shift.

The variations in the relaxation behaviour can be summarized as follows.

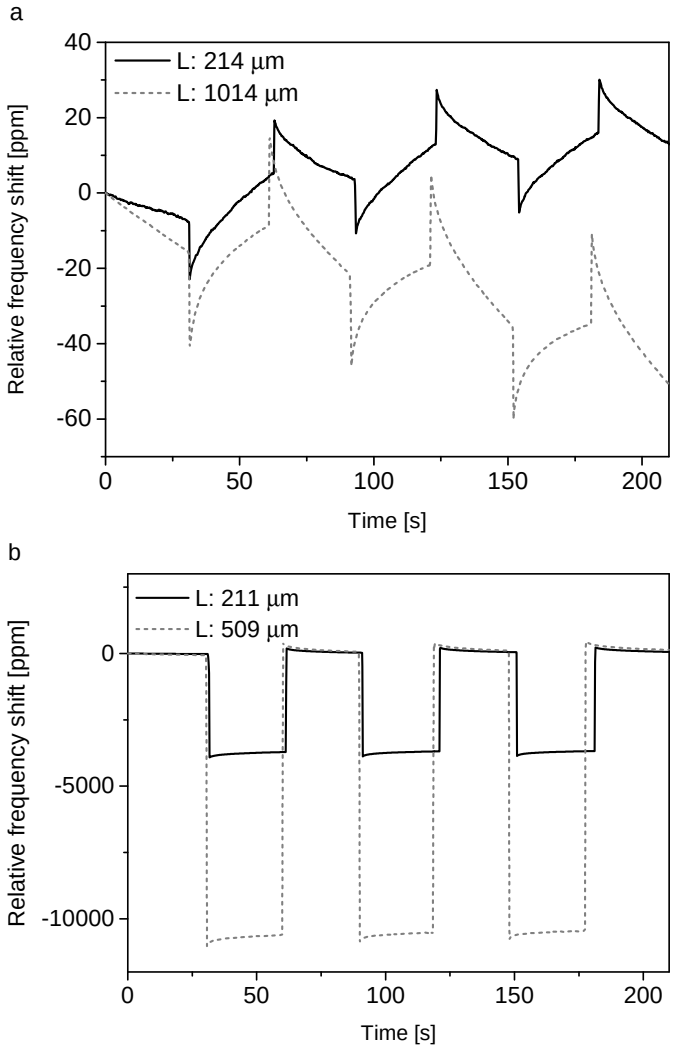

Figure 7.13: Influence of string length. (a) Relative resonance frequency of two SiN strings that have a width of 5.1 µm, a thickness of 61 nm, and different lengths of 214 µm and of 1014 µm, when the power of the laser was changed between 1.9 µW and 200 µW with 30 seconds' intervals. (b) Relative resonance frequency of two SRN strings that have a width of 5.5 µm, a thickness of 185 nm, and different lengths of 211 µm and of 509 µm, when the power of the laser was again changed between 1.9 µW and 200 µW with 30 seconds' intervals.

When the vibrometer laser is focused on a string, heat from the vibrometer laser is constantly pumped into the silicon chip by the heat travelling through the string before it heats up the silicon chip. At equilibrium, the heat input from the vibrometer laser equalises the heat loss from the silicon chip to the environment. When the silicon chip is heated, it expands and it causes the frequency to increase. With a string which conducts the heat faster (e.g. short or thick string), the temperature of the silicon chip finds an equilibrium faster which leads to a shorter relaxation time, while with a string which conducts the heat poorly (e.g. long or thin string), it takes longer time to reach an equilibrium temperature of the silicon chip, and hence a longer relaxation time.

Changing the IR laser power instead of the readout laser power caused similar responses such as that it takes longer time for a SiN string to come to an equilibrium temperature after a laser power change compared to a SRN string of similar dimensions. Thus it is highly probable that strings would behave in the same ways as described in this section when another heat source is used to induce a frequency change instead of the readout laser.

7.2.4 Response Time

In this photothermal IR spectrometer, we have assumed that IR light would irradiate only the string without irradiating the frame. The IR light from the thermal IR source is, however, not collimated and it is hard to bring the IR light into a small focus so that it would not heat the frame. Besides, the power of the thermal IR source is very low so we were unable to measure the diameter of the IR light when focused on the string. This missing information was partly found later by comparing the response time of strings when irradiated by the thermal IR light and by the IR laser.

The lowest frequency of our chopper 1 Hz is used for the photothermal IR spectrometer with the thermal IR source. Fig. 7.14(a) shows resonance frequency of a SiN string irradiated by a scanning thermal IR light and with the chopper set at 1 Hz, which means that the string is irradiated to IR light for 500 ms and then the chopper blocks the IR light so that the string is not irradiated to IR light for the next 500 ms and these two steps are repeated. For example at $\sim$3.8 second the chopper opens for the IR light to irradiate the string and after three measurement points that corresponds to $\sim$500 ms, the frequency is still shifting downwards. At $\sim$4.3 second the chopper starts blocking the IR light and the frequency starts shifting upwards. Since the frequency is still shifting towards thermal equilibrium after 500 ms, the frequency has not reached the thermal equilibrium after 500 ms.

Fig. 7.14(b) shows resonance frequency of a SiN string irradiated by a scanning IR laser and with the chopper set at 10 Hz. Lock-in amplifier was used to determine the frequency of the AC signal coming from the laser Doppler vibrometer and to store the measured values in this measurement.

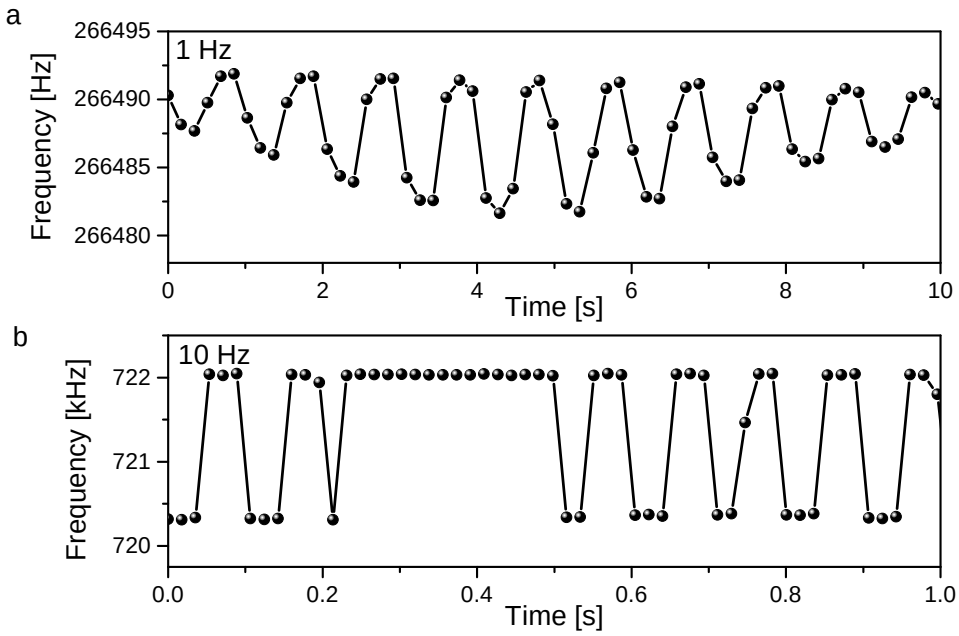

Figure 7.14: (a) Resonance frequency of a 506 µm long, 6.0 µm wide and 157 nm thick SiN string with a scanning thermal IR light irradiated and with a chopper set at 1 Hz. The sampling rate of the frequency counter is ∼172 ms. (b) Resonance frequency of a 100 µm long, 5.0 µm wide and 100 nm thick SiN string with a 10 nm gold coating with QCL irradiated and with a chopper set at 10 Hz. The sampling rate was set to ∼18 ms.

The sampling rate was set to ∼18 ms. It can be seen that the frequency reaches the thermal equilibrium between two measurement points which corresponds to ∼18 ms after opening/closing the chopper for the IR light.

Larsen *et al* reported time constant from similar experiments by monitoring the AC signal from the laser-Doppler vibrometer on an oscilloscope for an instant change of the laser power from 50 - 200 µW and it was reported to be ∼30 ms for different types and different lengths of strings when heating only strings by laser [85]. They also calculated the characteristic time constants to be 516 µs for a 114 µm long SRN string and 41 ms for a 1022 µm long SRN string.

As the strings in this project are long, narrow and thin, only the strings act as the heat sensing element which has an extremely low thermal mass and the support can be considered as a heat sink. For this type of construction, a characteristic thermal time constant, the time required for the output to complete 63.2% of the total rise (or decay) resulting from a step change in the input [130], is defined by the ratio between the thermal mass H (J/K) of the string and the thermal conductance G (W/m·K) to its support [131]. A thermal time constant when heating at the center of the string can be

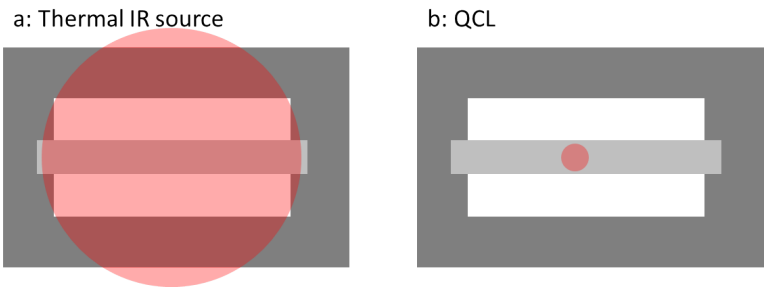

Figure 7.15: Schematic drawings showing the size of the focused IR light when (a) thermal IR source is used and (b) QCL is used.

calculated from

$$\tau = \frac{l^2 \rho c}{4k}, \tag{7.1}$$

where l, ρ, c and k are the length, the mass density, the specific heat capacity and the thermal conductivity of the string. Assuming specific heat capacity, thermal conductivity and mass density of SiN and SRN as in Table 7.1, a thermal time constant of 279 ms, 69 ms and 2.7 ms can be calculated for the 1014 µm long, 506 µm long, and 100 µm long SiN strings, respectively, and a thermal time constant of 7.0 ms and 563 µs can be calculated for the 328 µm long, and 110 µm long SRN strings, respectively.

Comparing the time constant of 69 ms for the 506 µm long SiN to the experimental results in Fig. 7.14(a) that show ∼172 ms between two measurement points and that it does not complete the rise or decay after 500 ms, it can be deduced that both the string and the support are heated when the thermal IR source is used as shown in Fig. 7.15(a). The reason for the long response time when both the string and the support are heated is, that the support has a much larger thermal mass than the string itself which requires a longer time to reach a thermal equilibrium. In the same way, comparing the time constant of 2.7 ms for the 100 µm long SiN to the experimental result in Fig. 7.14(b) which shows ∼18 ms between two measurement points and that it completes 100% of the total rise and decay within the two measurement points, the experimental data agrees well with the calculated time constant and thus it can be deduced that only the string is heated when QCL is used as an IR source as shown in Fig. 7.15(b).

Thermal properties, especially thermal conductivity of SRN vary broadly depending on the ratio between silicon and nitride and on the process parameters. Thermal conductivity of k_{SRN}=20 W/(m·K) has been assumed for the calculation which is close to the higher end value of the reported 3 - 24 W/(m·K) [102]. When the thermal conductivity is 3 W/(m·K), which is similar to that of SiN, the calculated time constant is also similar between SiN and SRN. When the thermal conductivity is 24 W/(m·K), a SRN string responds more than 7 times faster than a SiN string of the same length.

It is of a great importance to have only the string irradiated and not the support for a faster response time. Using an IR laser allows us to irradiate only the string opposing to the thermal source that also irradiates the support. It has been also shown from calculations that SRN strings have a shorter response time compared to SiN strings of the same length due to the higher thermal conductivity.

7.2.5 Frequency Stability

The thermal resolution of a string resonator is defined by its responsivity and frequency stability. We covered how to optimize the responsivity in section 7.2.2 and we will here investigate the frequency stability of the string resonators. If the responsivity stays constant the detection limited can only be improved if the frequency stability is improved. The Allan deviation as a function of averaging time is a standardized measure for the instability of a frequency measurement. The Allan deviation can be calculated from a frequency vs. time data set and it is defined as the square root of the Allan variance which can be written as

$$\sigma_y^2(\tau) = \frac{1}{2(M-1)} \sum_{i=1}^{M-1} [y_{i+1} - y_i]^2, \tag{7.2}$$

where $\bar{y}_i$ is the ith fractional frequency average over the observation period τ and M is the number of fractional frequency values. A log-log plot of the Allan deviation can reveal the origin of the instability in a frequency measurement [132].

The setups to measure resonance frequency described in Section 6.1 were used for the continuous frequency measurements. A PZT element placed in a positive feedback loop was used for actuation of the strings when the noise from the thermal IR source with a filter wheel was investigated. The resonance frequency was measured by the laser-Doppler vibrometer and the frequency counter. A LabVIEW program was used to acquire and store the measured values. A PZT element placed in a phase-locked loop was used for actuation of the strings when the noise from the QCLs were investigated. The measurements were started one hour after starting the turbo pump to minimize the temperature fluctuation caused by the turbo pump. To calculate the Allan deviation, the frequency of the strings was measured for about 25 minutes.

The influence of the IR sources, the readout laser power, the amount of reflected readout laser light, and the string material on the frequency stability has been investigated. Fig. 7.16(a) shows the measured resonance frequency of a SRN string as a function of time and Fig. 7.16(b) shows the calculated Allan deviation as a function of averaging time. The measured resonance frequency was drifting upwards during the entire measurement and thus there

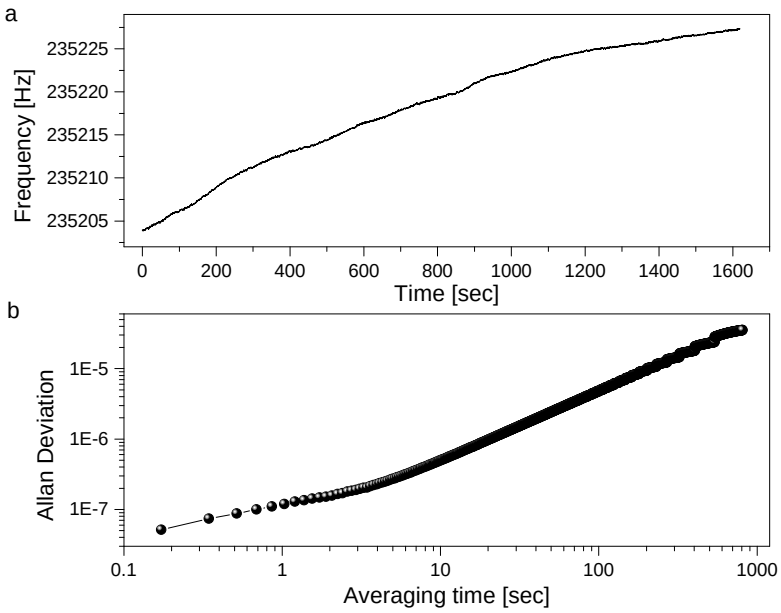

Figure 7.16: (a) Measured resonance frequency of a 509 μm long, 5.4 μm wide and 185 nm thick SRN string as a function of time. (b) Calculated Allan deviation as a function of averaging time of the measured resonance frequency of the same string.

is no minimum in the Allan deviation, which means that the drift is dominating for measurement. The reason for the drifting resonance frequency is that the temperature of the string chip was increasing during the measurement. There are several sources to introduce a temperature change inside the chamber such as ambient temperature and the turbo pump. Another reason is that the temperature inside the chamber drops when the air inside it is pumped out, which is called the Joule-Thomson effect. This phenomenon combined with the heating of the chamber by the turbo pump makes the temperature of the chip increase slowly for hours [128]. It could be possible to achieve better frequency and temperature resolutions if temperature stabilization is used.

The readout laser in the vibrometer uses a visible light at a wavelength of 633 nm. We have found that a SRN string absorbs the light at a wavelength of 633 nm by 3 orders of magnitude more than a SiN string as discussed in Section 7.2.2. While the fluctuation in the readout laser power is negligible for a SiN string due to the extremely low absorption of the readout laser, it affects a SRN string more by fluctuating its frequency.

Firstly using the thermal IR source, we have calculated the Allan deviations of frequency vs. time measurements for three scenarios using an uncoated string: i) without IR light, ii) with IR light at 1176 cm^{-1} where there is low absorption in silicon nitride and iii) with IR light at 909 cm^{-1}

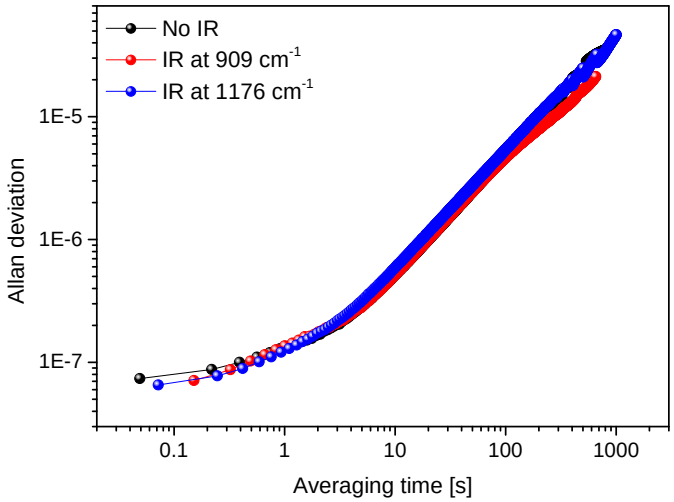

Figure 7.17: Allan deviations showing the influence of the thermal IR source. The resonance frequency of a 509 µm long, 5.4 µm wide and 185 nm thick SRN string was measured without and with IR irradiated at 909 cm^{-1} where there is high absorption in silicon nitride and at 1176 cm^{-1} where there is low absorption in silicon nitride and with a readout laser power of 1.9 µW. Allan deviations of $\sigma(1s) \approx 1.2 \times 10^{-7}$, $\sigma(1s) \approx 1.3 \times 10^{-7}$, and $\sigma(1s) \approx 1.1 \times 10^{-7}$ were obtained from the respective measurements.

where there is high absorption in silicon nitride, that are shown in Fig. 7.17. The lowest readout laser power of 1.9 µW was used. Allan deviations of $\sigma(1s) \approx 1.2 \times 10^{-7}$, $\sigma(1s) \approx 1.1 \times 10^{-7}$ and $\sigma(1s) \approx 1.3 \times 10^{-7}$ were obtained from the respective measurements. It can be seen that IR radiation does not change the Allan deviation. This means that the thermal IR source does not add any measurable noise to the frequency measurement.

Secondly using the QCL, we have calculated the Allan deviations of frequency vs. time measurements in order to assess the influences of the four different QCL modules, the power of IR laser, and the power of readout laser. The QCL consists of four laser modules as described in Section 7.1. The first module ranges from 925 cm^{-1} to 1110 cm^{-1}, the second from 1110 cm^{-1} to 1316 cm^{-1}, the third from 1316 cm^{-1} to 1616 cm^{-1} and the fourth from 1616 cm^{-1} to 1921 cm^{-1}. For the following measurements, the wavenumbers of 1000 cm^{-1}, 1175 cm^{-1}, 1495 cm^{-1} and 1690 cm^{-1} have been used as the representatives of each module as shown in Fig. 7.18.

Fig. 7.19 shows the influence of the QCL on the Allan deviations. The resonance frequency of a SiN string was measured without and with IR radiation at 1495 $cm^{-1}$with a duty cycle of 5.0% from the QCL. Allan deviations of $\sigma(1s) \approx 9.4 \times 10^{-8}$ and $\sigma(1s) \approx 2.1 \times 10^{-7}$ were obtained, respectively. The blue plot with IR radiation has a minimum Allan deviation of $\sigma(5s) \approx 1.5 \times 10^{-7}$, which could be the inherent instability of the QCL [133]. It can be seen that IR radiation from the QCL adds noise in the frequency measurement contrary to the results with the thermal IR source which does

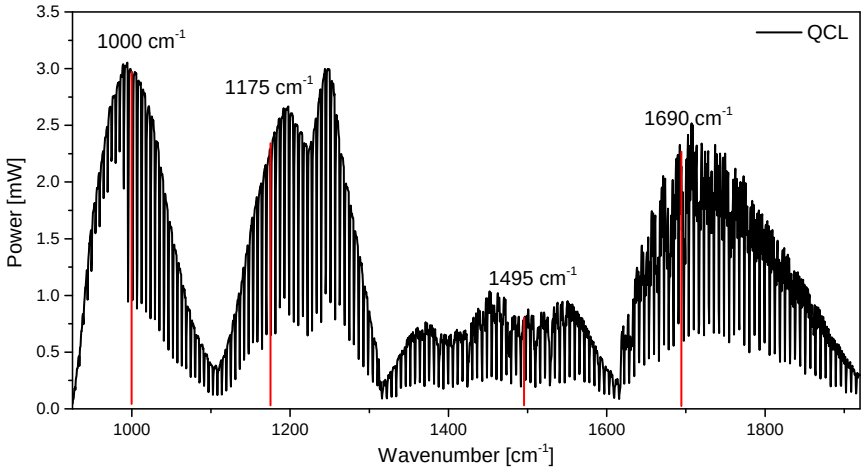

Figure 7.18: QCL power as a function of wavenumber, showing 4 laser modules. The red lines show the wavenumbers of 1000 cm^{-1}, 1175 cm^{-1}, 1495 cm^{-1} and 1690 cm^{-1} that are the representatives of each module used for the resonance frequency measurements.

not add noise.

In the same way Allan deviations of the four different QCL modules were calculated from the resonance frequencies measured of a 100 μm long, 1.0 μm wide and 100 nm thick SiN string with IR irradiated at 1000 cm^{-1}, 1175 cm^{-1}, 1495 cm^{-1}, and 1690 cm^{-1} as shown with red lines in Fig. 7.18 with a duty cycle of IR laser of 5.0% and with a readout laser power of 200 μW. Allan deviations of $\sigma(1s) \approx 1.3 \times 10^{-5}$, $\sigma(1s) \approx 1.2 \times 10^{-6}$, $\sigma(1s) \approx 2.1 \times 10^{-7}$, and $\sigma(1s) \approx 2.0 \times 10^{-7}$ were obtained from the respective measurements. According to the calculated Allan deviations, each laser module has different noise level. Silicon nitride has a strong absorption peak which covers roughly the whole wavenumber range of module 1. The high absorbance can be the reason for the one to two orders of magnitude higher noise level of module 1 compared to the other modules. The second laser module is 6 times as noisy as module 4 though the power of the two lasers are similar.

Fig. 7.20 shows the influence of the power of readout laser. The resonance frequency of a SRN string was measured with a readout laser power of 1.9 μW and 200 μW. Allan deviations of $\sigma(1s) \approx 1.52 \times 10^{-7}$ with the readout laser power of 1.9 μW and $\sigma(1s) \approx 2.77 \times 10^{-6}$ with the readout laser power of 200 μW were obtained from the respective measurements. The black plot with readout laser of 1.9 μW has a minimum Allan deviation of $\sigma(4s) \approx 6.2 \times 10^{-7}$, which also could be the inherent instability of the QCL. It can be seen that increasing the readout laser power by 2 orders of magnitude has increased the Allan deviation of SRN by 19 times. This is due to the larger fluctuation in the readout laser power when the power is higher and the absorption of the visible light at 633 nm by the SRN string.

Fig. 7.21 shows the influence of the amount of reflected readout laser

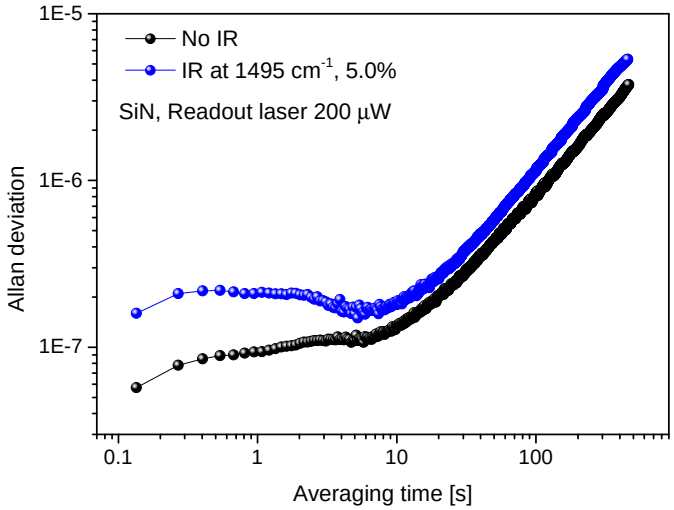

Figure 7.19: Allan deviations showing the influence of the QCL. The resonance frequency of a 100 µm long, 1.0 µm wide and 100 nm thick SiN string was measured without and with IR irradiated at 1495 cm^{-1} with a duty cycle of 5.0% and with a readout laser power of 200 µW. Allan deviations of $\sigma(1s) \approx 9.4 \times 10^{-8}$ and $\sigma(1s) \approx 2.1 \times 10^{-7}$ were obtained from the respective measurements.

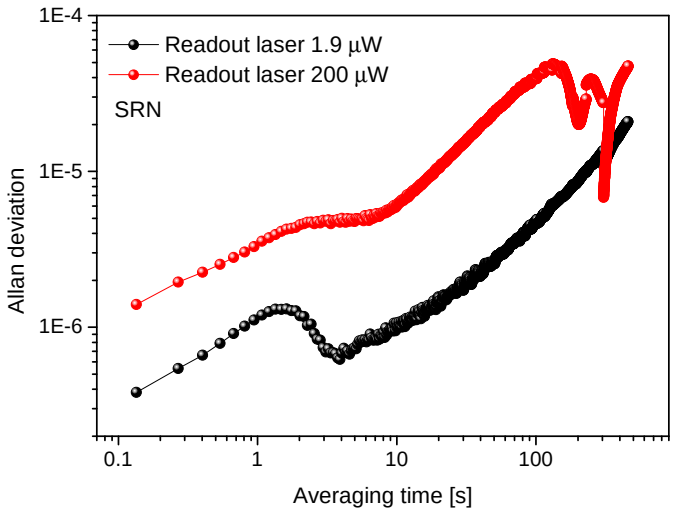

Figure 7.20: Allan deviations showing the influence of the readout laser power. Resonance frequencies of a 509 µm long, 5.4 µm wide and 185 nm thick SRN string were measured with IR irradiated at 1495 cm^{-1} with a duty cycle of 5.0% and with a laser power of 1.9 µW and 200 µW. Allan deviations of $\sigma(1s) \approx 1.5 \times 10^{-7}$ with the readout laser power of 1.9 µW and $\sigma(1s) \approx 2.8 \times 10^{-6}$ with the readout laser power of 200 µW were obtained from the respective measurements.

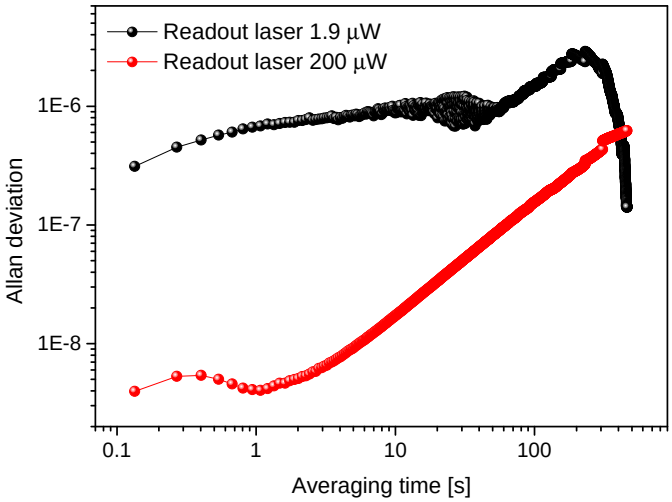

Figure 7.21: Allan deviations showing the influence of the amount of reflected readout laser light. Resonance frequencies of a 110 µm long, 1.2 µm wide, and 185 nm thick SRN string were measured with a readout laser power of 1.9 µW and 200 µW. Allan deviations of $\sigma(1s) \approx 6.6 \times 10^{-7}$ and $\sigma(1s) \approx 4.1 \times 10^{-9}$ were obtained for the readout laser power of 1.9 µW and 200 µW, respectively.

light. The resonance frequencies of a 1.2 µm wide SRN string, whose width is much narrower than the diameter of the readout laser spot ∼6 µm were measured. Allan deviations of $\sigma(1s) \approx 6.6 \times 10^{-7}$ and $\sigma(1s) \approx 4.1 \times 10^{-9}$ were obtained for the readout laser power of 1.9 and 200 µW, respectively. The red plot with readout laser of 200 µW has a minimum Allan deviation of $\sigma(1s) \approx 4.0 \times 10^{-9}$, which could be the inherent instability of the readout laser. It is clearly seen that too little amount of reflected readout laser light leads to an unstable frequency measurement. During my experiments, a width of 5 µm has been wide enough for a good reflection of the readout laser when using the minimum power of the readout laser 1.9 µW. When reading out frequency using an optical method, downsizing of the width of a string can be limited due to the "amount of reflected readout laser light".

Fig. 7.22 shows the influence of the string material. The resonance frequencies of a SRN string and a SiN string were measured. Allan deviations of $\sigma(1s) \approx 4.1 \times 10^{-9}$ for the SRN string and $\sigma(1s) \approx 9.4 \times 10^{-8}$ for the SiN string were obtained from the respective measurements. The frequency resolution is determined by taking three times the Allan deviation for an averaging time of 1 second [85]. It is clearly seen that a SRN string has a better frequency resolution than a SiN string as these two strings have similar dimensions. Although a SRN string is affected more by the fluctuation of the readout laser power, a SRN string outmatches a SiN string of similar dimensions due to the better frequency resolution.

The lowest Allan deviation $\sigma(1s) \approx 4.1 \times 10^{-9}$ was obtained from 110 µm long, 1.2 µm wide, and 185 nm thick SRN string, which is the shortest

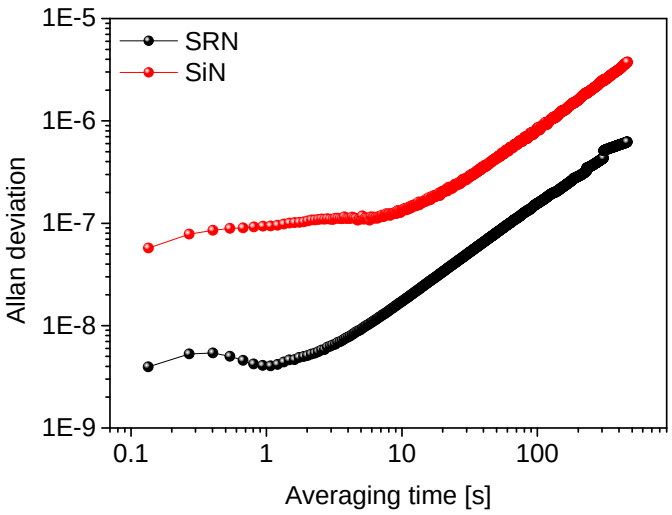

Figure 7.22: Allan deviations showing the influence of the string material. Resonance frequencies of a 110 µm long, 1.2 µm wide, and 185 nm thick SRN string and a 100 µm long, 1.0 µm wide and 100 nm thick SiN string were measured without IR and with a laser power of 200 µW. Allan deviations of $\sigma(1s) \approx 4.1 \times 10^{-9}$ for the SRN string and $\sigma(1s) \approx 9.4 \times 10^{-8}$ for the SiN string were obtained from the respective measurements.

SRN string used in the experiments. While the thermal IR source does not add any noise to the frequency measurement, the QCL modules are obvious noise sources. It is important to use a higher readout laser power to obtain a good reflection for readout when a string width is small. A SRN string has a better frequency resolution than a SiN string which can be important when estimating a detection limit.

7.2.6 Power Resolution

The power resolution of the strings are going to set the lower detection limit for the string-based photothermal spectroscopy and it is defined as the frequency resolution divided by the power sensitivity. The sensitivity of a string is, as described in Eq. 4.15, determined by its resonant mode number, Young's modulus, mass density, build-in tensile stress, thermal expansion coefficient, thermal conductivity, length and cross-sectional area. The frequency resolution is dependent on the quality factor of the string, the methods used to actuate and to readout the resonance frequency, and the method to irradiate the string with IR. We here compare the estimated power resolution of three different strings; short and long strings made of SRN and a short SiN string when thermal IR source is used and a long SRN string when QCL is used. In Table 7.2 string dimensions are listed with the estimated power sensitivity, Allan deviation and power resolution.

We have calculated Allan deviations of frequency versus time measure-

Table 7.2: Dimensions, estimated power (P) sensitivity, Allan deviation and power (P) resolution of the strings.

	SRN long	SRN short	SiN short	SRN (QCL)
Length [μm]	509	110	100	509
Width [μm]	5.4	1.2	1.0	5.4
Thickness [nm]	185	185	100	185
P sensitivity [W^{-1}]	20784	4489	1728	20784
Allan deviation $\sigma(1s)$	1.1×10^{-7}	4.1×10^{-9}	9.4×10^{-8}	1.5×10^{-7}
P resolution [pW]	16	2.7	160	22

ments of bare strings in Section 7.2.5. The relative frequency change per absorbed power of a 509 μm long, 5.4 μm wide, and 185 nm thick SRN string is calculated to be 20784 W^{-1} from the relative frequency shift of 55.7 ppm and the absorbed power of 2.68 nW, which will be discussed later in Section 7.3.1. From the Allan deviation $\sigma(1s) \approx 1.1 \times 10^{-7}$, the detection limit is calculated to be approximately 16 pW for a signal to noise ratio of 3.

Shorter strings give generally smaller Allan deviations as discussed in Section 7.2.5. Here we calculate the power resolution of a 110 μm long SRN string. The resonance frequency of a 110 μm long SRN string is measured to be 1174 kHz. The relative frequency decreases linearly with increasing length of a string as described Eq. 4.14. Accordingly the relative frequency shift is calculated to be 12.0 ppm assuming the following parameters: tensile stress 200 MPa, mass density 3100 kg/m^3, thermal coefficient of expansion 1.23 ppm/K [84], Youngs modulus 250 GPa, and thermal conductivity 2.5 W/(m·K) [100], for SRN. The power resolution of the 110 μm SRN string is calculated to be 2.7 pW for a signal to noise ratio of 3 with the relative frequency change 4489 W^{-1} and the Allan deviation of $\sigma(1s) \approx 4.1 \times 10^{-9}$. Consequently a 110 μm SRN string exhibits one order of magnitude higher power resolution than a 509 μm SRN string thanks to its extraordinary resolution of the frequency measurement.

The resonance frequency of a string is determined by its resonant mode number, length, build-in stress and mass density (Eq. 4.5). The resonance frequency of a 100 μm long SiN string is measured to be 2716 kHz. The resonance frequency of a 100 μm long SRN string is calculated to be 1291 kHz.

Eq. 4.5 can be rewritten as

$$\frac{n}{2f_{SRN}}\sqrt{\frac{\sigma_{SRN}}{\rho}} = \frac{n}{2f_{SiN}}\sqrt{\frac{\sigma_{SiN}}{\rho}}, \tag{7.3}$$

when the length of a SRN string and a SiN string is the same. $\sigma_{SiN} = 4.425\sigma_{SRN}$ is obtained by inserting $f_{SRN} = 1291{\times}10^3$ and $f_{SiN} = 2716{\times}10^3$. As $\sigma_{SRN} = 200 \times 10^6$ has been assumed, $\sigma_{SiN} = 885 \times 10^6$ will be used in the further calculations.

The relative frequency shift of 4.63 ppm for a 100 µm long SiN string is calculated from Eq. 4.14 by inserting $f_{SiN} = 2716 \times 10^3$, $\sigma_{SiN} = 885 \times 10^6$, $L = 100 \times 10^{-6}$, $A = 1.0 \times 10^{-12}$, $P = 2.68 \times 10^{-9}$ and assuming the following parameters for SiN: thermal expansion coefficient 2.0 ppm/K, Young's modulus 250 GPa, thermal conductivity 2.1 W/(m·K). The power resolution of the 100 µm SiN string is calculated to be 160 pW for a signal to noise ratio of 3 with the relative frequency change 1728 W^{-1} and the Allan deviation of $\sigma(1s) \approx 9.4 \times 10^{-8}$.

We measured that our QCL emits an IR power of 780 µW at 1495 cm^{-1} with a duty cycle of 5%. The relative frequency shift of a 509 µm long, 5.4 µm wide and 185 nm thick SRN string was measured to be 1.76×10^{-3} at at 1495 cm^{-1} with a duty cycle of 5% as shown in Fig. 7.10. The absorbed power is calculated to be approximately 84.7 nW using Eq. 4.14 assuming same parameters for other SRN strings. It is generally considered that silicon nitride does not absorb light at 1495 cm^{-1} and it is in a way true that only 9.3 ppb of the radiated IR light is absorbed by silicon nitride. The relative frequency change per absorbed power for this string also has 20784 W^{-1} as two strings that have same dimensions and same material have the same power sensitivity. The power resolution is calculated to be 22 pW for a signal to noise ratio of 3 from the Allan deviation of $\sigma(1s) \approx 1.5 \times 10^{-7}$.

When comparing the estimated power resolution it can be seen that the short SRN string gives the best prerformance which can be attributed to the high frequency resolution. This is one order of magnitude higher than that of more complex bimaterial cantilevers with a typical detection limit of 12 pW for the same signal to noise ratio [134, 135]. A better power resolution is obtained when the thermal source is used as its IR source as QCL adds noise to frequency measurements. The effect of noise from the QCL to the power resolution is, however, smaller than the effect of the length and the material of the string. QCL enables us to obtain both a larger absolute frequency shift and a larger relative frequency shift which are great advantages when the amount of sample needs to be decreased.

7.2.7 Summary - String Characterisation

Results from the analytical expression for photothermal frequency response have been compared to results obtained by FEM simulations. FEM simula-

tions have shown that the frequency shift induced by local heating at the center of a string scales linear with the inverse of the string width, with the inverse of the string thickness, with the string length, with the heating power and with the inverse of the thickness of the gold coating on a silicon nitride string. Based on the comparison, the analytical expression is considered valid for long and thin strings.

As the analytical model and the FEM simulations predicted, the experimental data has shown that the relative frequency shift is increasing linearly with decreasing string width, with decreasing string thickness, with increasing string length, and with increasing heating power. From a practical point of view, it is recommended for a string to have a minimum thickness of 100 nm, a minimum width of 1 μm, and a minimum length of 100 μm with a chip design of strings not too close to each other when reading out optically using the vibrometer and actuating a single frequency using the PLL.

A SiN string exhibits a higher ratio of thermal relaxation compared to its fast frequency shift and it takes a longer time to stabilise than a SRN string. The shorter stabilization time of the SRN string is more desirable for photothermal spectroscopy. A chopper with an appropriate frequency would be helpful for this relaxation issue in order to obtain only the value of the first quick shift.

It is of a great importance to have only the string irradiated and not the support for a faster response time. Using an IR laser allows us to irradiate only the string opposing to the thermal source that also irradiates the support. It has been also shown from calculations that SRN strings have a shorter response time compared to SiN strings of the same length due to the higher thermal conductivity.

Frequency stability of the string resonators were investigated by calculating the Allan deviations. The lowest Allan deviation 4.09×10^{-9} was obtained from 110 μm long, 1.2 μm wide, and 185 nm thick SRN string, which is the shortest SRN string used in the experiments. While the thermal IR source does not add any noise to the frequency measurement, the QCL modules are obvious noise sources. It is important to use a higher readout laser power to obtain a good reflection for readout when a string width is smaller than the diameter of the readout laser. A SRN string has a better frequency resolution than a SiN string which can be important when estimating a detection limit.

A short SRN string gives the best prerformance which can be attributed to the high frequency resolution. A better power resolution is obtained when the thermal source is used as its IR source as the QCL adds noise to the frequency measurements. The best power resolution has been obtained by using the shortest SRN string due to the highest frequency resolution. In the following sections, these silicon nitride strings are applied and applications of photothermal IR spectroscopy are explored.

7.3 Photothermal IR Spectroscopy with Thermal IR Source

Photothermal IR spectroscopy with mechanical string resonators is a sequential examination of resonance frequency as scanning IR is irradiating a string, which is like a dispersive IR spectrometer. In the nanomechanical IR spectroscopy (NAM-IR), a string is used as a sampling filter fibre as well as an IR detector. A sample deposited on the string interacts with the IR when the string is exposed to scanning IR light. The sample absorbs IR light at its vibrational frequency as described in Section 4.4, heating up the string. The frequency shift of the string can be directly related to the amount of absorbed IR light. In this section, photothermal IR spectroscopy with mechanical string resonators is demonstrated.

7.3.1 Silicon Nitride

The sensing material of the photothermal IR spectroscopy, silicon nitride is not entirely transparent for IR light. Thus, at first the photothermal absorption spectrum of a bare SRN resonator is recorded using the thermal IR source. Fig. 7.23(a) shows a photothermal IR spectrum of a bare SRN string, showing a strong and broad absorption peak at 904 cm^{-1}. This peak position has been verified by means of conventional FTIR spectroscopy. Fig. 7.23(b)(c) show the absorption spectra of a silicon wafer and a silicon wafer with a 185 nm thick SRN layer. From these two spectra it can be deduced that the silicon nitride layer has an absorption peak at 895 cm^{-1}. Silicon nitride thin film is known to have an absorption peak at 830 - 1250 cm^{-1}, depending on the thickness of the silicon nitride. The absorption peak is shifted to longer wavelengths when the thickness of the silicon nitride is reduced [136]. This absorption is caused by the stretching of silicon-nitrogen bonds and the peak position is in good agreement with the position determined by photothermal IR spectroscopy. Fig. 7.23(b)(c) also show an absorption peak at 1106 cm^{-1} deriving from silicon. The absorption peaks at 1400 - 1800 cm^{-1} and 3600 - 4000 cm^{-1} derive from water vapor and the absorption peak at 2350 cm^{-1} derives from carbon dioxide since these samples were measured in air.

For the presented measurements, an IR monochromator with a thermal light source has been used. The power of radiated light absorbed by the micromechanical string resonator is estimated from the measurement of the bare SRN string. The absolute frequency shift of the SRN string of 13.1 Hz at 904 cm^{-1} (Fig. 7.23(a)) corresponds to a relative frequency shift of 55.7 ppm. The relative resonance frequency change of a mechanical string resonator (with length L and cross section area A) as a function of the absorbed power P in the string center is given by Eq. 4.14 as discussed in Section 4.2, with Youngs modulus E, thermal expansion coefficient α, tensile prestress

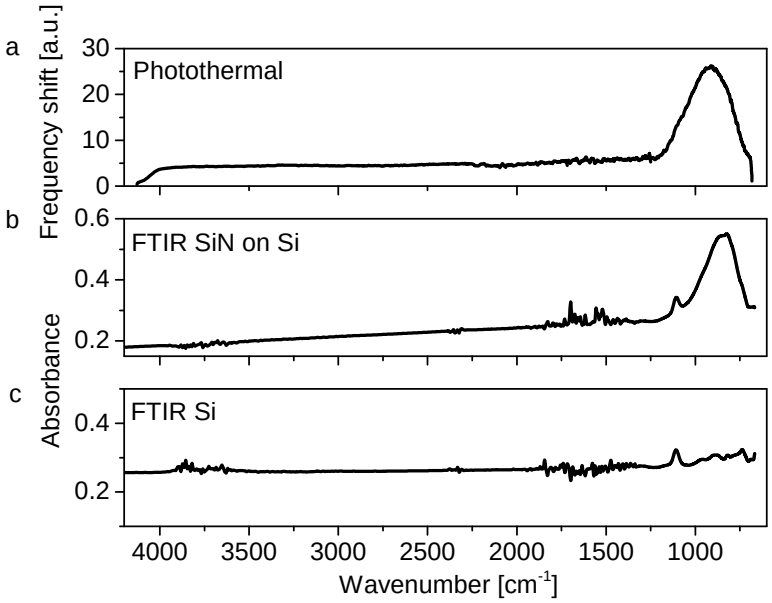

Figure 7.23: (a) Photothermal IR spectrum of a 509 μm long, 5.4 μm wide ad 185 nm thick SRN string, showing a strong and broad absorption peak at 904 cm^{-1}. (b) IR absorption spectrum of a 185 nm thick SRN membrane on a 350 μm thick double side polished silicon wafer, showing an absorption peak at 1106 cm^{-1} deriving from silicon and an absorption peak at 895 cm^{-1} deriving from silicon nitride. (c) IR absorption spectrum of a 350 μm thick double side polished silicon wafer, showing an absorption peak at 1108 cm^{-1}.

σ_0, and thermal conductivity κ, of the string material. From equation 4.14, it is calculated that the measured frequency shift corresponds to approximately 2.68 nW of absorbed heat in the string. The absorbance of silicon nitride can be extracted from the FTIR measurements by subtracting the absorbance of bare silicon (Fig. 7.23(c)) from the absorbance of silicon nitride on a silicon wafer (Fig. 7.23(b)). A differential absorbance of 0.196 can be calculated at 904 cm^{-1}, which results in an IR power radiated on the string of approximately 14 nW. The calculations were done assuming the following parameters: tensile stress 200 MPa, mass density 3100 kg/m^3, thermal coefficient of expansion 1.23 ppm/K [84], Youngs modulus 250 GPa, and thermal conductivity 2.5 W/(m·K) [100].

It seems that the IR light actually heats up both the string and a part of the frame as discussed in Section 7.2.4. The frequency was lowered when the string was irradiated by IR light which means that the tensile stress of the string was lowered when heated. This indicates that the expansion of the Si frame was still negligible as the thermal expansion coefficients of SRN and Si are 1.23 ppm/K and 2.56 ppm/K, respectively. The calculated power of IR light could be larger than 14 nW.

7.3.2 Polyvinylpyrrolidone

Biodegradable polymers are becoming increasingly used [137,138] and there is a large demand for polymer characterization and identification. As a representative of polymer, PVP was nebulized and the resulting aerosol was sampled on a string resonator. The structure of PVP is shwon in Fig. 7.24. In Fig. 7.25(a)(b), photothermal IR spectra of PVP deposited on two different strings show the repeatability of the measurement. It can be seen that the two photothermal IR spectra of PVP from two different strings are highly reproducible. All the four major absorption peaks in the photothermal IR spectra at 1267, 1407, 1651 and 2878 cm^{-1} are in excellent agreement with the reference IR absorption spectrum of PVP measured in air, showing major absorption peaks at 1285, 1422, 1651 and 2951 cm^{-1} (Fig. 7.25(c)). The distinct peak at 1651 cm^{-1} derives from the carbonyl double bonds in PVP. The extra absorption peak at 3428 cm^{-1} of the FTIR measurement derives from water vapor.

An additional mass which is a significant fraction of the resonator mass can be derived by comparing the frequency before and after the mass deposition

$$f_0^2 - f_{\Delta m}^2 = \frac{k}{m} - \frac{k}{m + \Delta m}, \tag{7.4}$$

where f_0 is the resonance frequency, $f_{\Delta m}$ is the resonance frequency with an additional mass, k is the spring constant, m is the mass of the string and

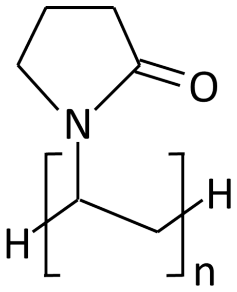

Figure 7.24: Repeat unit for PVP.

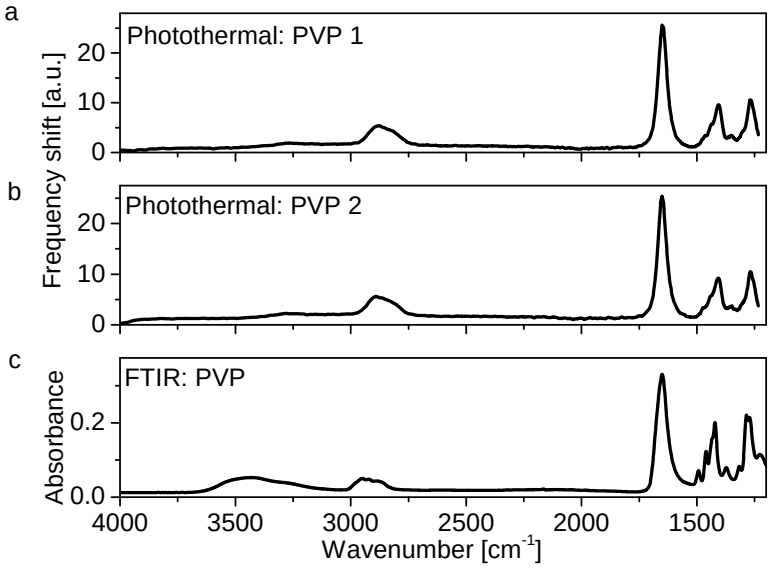

Figure 7.25: PVP analysis. (a) Photothermal IR spectrum of PVP (with a total mass of 1.2 ng) on a SiN string (506 µm long, 3 µm wide and 157 nm thick). (b) Photothermal IR spectrum of PVP on another SiN string of equal dimensions. (c) FTIR absorption spectrum of PVP.

Δm is the additional mass. Eq. 7.4 can be solved for Δm which results in

$$\Delta m = m(1 - (\frac{f_{\Delta m}^2}{f_0^2})^2). \tag{7.5}$$

By inserting $f_{\Delta m} = f_0 - \Delta f$, this can be written as

$$\Delta m = m(1 - (1 - \frac{\Delta f}{f_0})^2), \tag{7.6}$$

which can be used to calculate a deposited mass on a string. The resonance frequencies of the silicon nitride string before and after the PVP deposition were 500 kHz and 268 kHz, respectively. From Eq. 7.6, the deposited mass of PVP on the string is calculated to be 1.2 ng assuming that the mass density of the silicon nitride string and PVP are 3440 kg/m^3 and 1200 kg/m^3, respectively. The mass of the 506 µm long, 3 µm wide and 157 nm thick string is calculated to be 0.81 ng.

It has been observed that SRN strings do not show the string behaviour any more when the PVP mass on on a SRN string is close to or larger than the string mass while SiN strings still show the string behaviour when the PVP mass is larger than the string mass. This could be related to the surface stress generated by the deposited PVP on a string surface due to the interaction between them. As PVP is deposited at a certain humidity level and the measurements are performed in vacuum, it is likely that PVP has experienced shrinkage (volume decrease) with decreasing humidity [139].

7.3.3 Organic Coating of Titanium Dioxide Nanoparticles

Analysis of airborne nanoparticles is a common scenario in the field of environmental and workplace safety. Chemical identification of airborne nanoparticles typically requires an electron microscope featuring an energy-dispersive X-ray spectrometer and is therefore time consuming and expensive [7,140]. The combination of an efficient in-situ sampling and photothermal IR spectroscopy is very attractive for chemical analysis of airborne engineered nanoparticles. The often used organic surface coating of engineered nanoparticles has shown to play a major role in the toxicity of nanoparticles [4]. It is therefore highly desired to be able to detect and distinguish surface coatings of nanoparticles.

Lists of nanomaterial properties that are relevant for their safety assessment are being established, for example by the Organisation for Economic Co-operation and Development (OECD) Working Party on Manufactured Nanomaterials (WPMN). The European commission's Joint Research Centre (JRC) has established the JRC nanomaterials repository for the NM-series of representative test materials in order to assist the testing under the OECD WPMN. The repository contains 24 representative nanomaterials of 8 different chemical compositions: titanium dioxide, zinc oxide, silicon dioxide,

cerium dioxide, silver, gold, multi-walled carbon nanotubes and bentonite (a nanoclay). The NM-series are studied in national, European and global scientific projects [141].

The material used in this study is NM-104, which is titanium dioxide nanoparticles in rutile form with a hydrophilic coating manufactured using thermal hydrolysis. They also reported that NM-104 formed stable suspensions at acidic pH (below pH 5) where the nanomaterials have high positive charge, exceeding 40 mV in its zeta potential [142]. NM-104 has been used as a reference material for systematic comparison and optimisation of extraction methods for titanium dioxide nanoparticles in sunscreen samples [143], in an assessment of genotoxicity of nano-titanium dioxide [144] and aggregation and agglomeration of titanium dioxide nanoparticles including NM-104 have been investegated using TEM [145].

Fig. 7.26 shows the differential photothermal IR spectrum of titanium dioxide nanoparticles with and without a coating. It can be clearly seen that the spectrum of titanium dioxide with a coating has two extra peaks at 1597 and 3389 cm^{-1}. Rasmussen *et al* reported that the organic coating of NM-104 titanium dioxide nanoparticles contained mainly tetramethyl silicate, glycerol, hexadecanoic acid methyl ester and octadecanoic acid [142]. The broad peak at 3389 cm^{-1} is typical from the stretching vibrations of oxygen-hydrogen bonds that are present in the glycerol of the particle coating. The sharp peak at 1597 cm^{-1} could be deriving from the stretching of the double bonds in the two different ester compounds. The resonance frequencies of the silicon nitride string before and after the deposition of the titanium dioxide nanoparticles with an organic coating were 246 kHz and 101 kHz, respectively. From Eq. 7.4, the deposited mass of titanium dioxide nanoparticles with an organic coating on the string is calculated to be 813 pg assuming that the mass density of SRN is 3440 kg/m^3. According to the specifications, the weight of the coating was 2% of the mass of the nanoparticles. This results in a total coating mass of 16 pg for a total titanium dioxide nanoparticle mass of 813 pg.

The minimum detectable sample mass can be estimated from the maximum induced frequency shift of ∼2.6 Hz (see Fig. 7.26) for a mass of 16 pg. This relates to a relative frequency change of roughly 1.6×10^6 g^{-1}, which results in a minimum detectable mass of 68 fg with an Allan deviation of 1.1×10^{-7}. Considering the linear relationship of photothermally induced frequency detuning and radiated light power, the estimated femtogram-scale mass resolution for nW-scale radiation power is well in agreement with the attogram-scale resolution obtained with similar mechanical resonators irradiated with a visible μW-laser [86]. The sensitivity of the presented photothermal IR spectroscopy can be improved by several orders of magnitude by replacing the weak thermal IR source and the monochromator with a more powerful light source. Modern tunable quantum cascade lasers provide IR powers of up to several 100 mW. Additionally, the sensitivity can

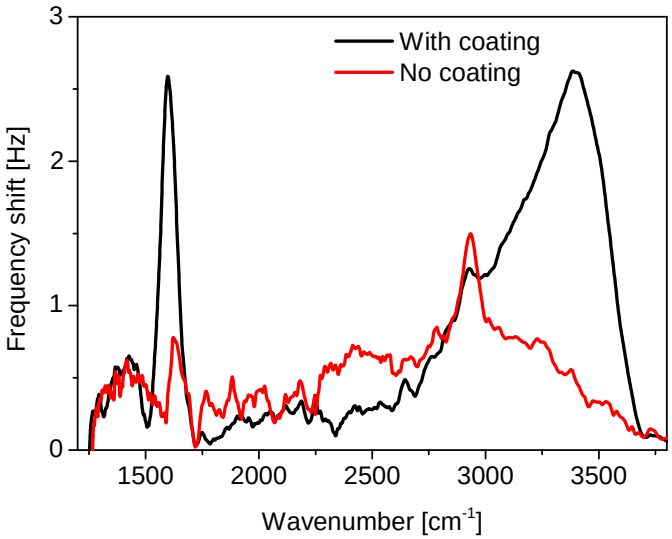

Figure 7.26: Identification of organic coating of nanoparticles. Differential photothermal IR spectra of 20 nm titanium dioxide nanoparticles (with a total mass of 813 pg) with and without an organic coating measured with a 512 µm long, 3.0 µm wide and 185 nm thick SRN string. The coating with a total mass of 16 pg is mainly composed of glycerol, tetramethyl silicate, hexadecanoic acid methyl ester and octadecanoic acid methyl ester.

be enhanced by optimizing the string design and the string material as discussed in Section 7.2 (e.g. 100 µm long, 1 to 5 µm wide and 100 nm thick SRN strings). The combination of an optimized string design and stronger radiation power gives prospect to photothermal IR spectroscopy in the zeptogram-range.

7.3.4 Summary - Photothermal Spectroscopy with Thermal IR Source

This section has been used to present the results obtained by performing the first photothermal IR spectroscopy with mechanical string resonators using a thermal IR source for chemical identification of the string material and airborne PVP. The obtained IR spectra measured by photothermal spectroscopy match the state-of-the-art IR spectra measured by an FTIR spectrometer. Airborne species can directly be collected on the string resonator by means of in-situ non-diffusion limited sampling. Further, we identified the organic coating of airborne titanimu oxide nanoparticles, with a mass of 16 pg.

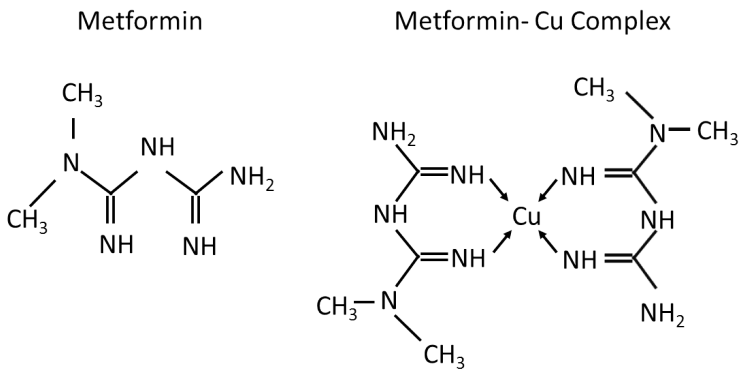

Figure 7.27: Chemical structures of metformin and metformin-copper complex.

7.4 Photothermal IR Spectroscopy with Quantum Cascade Lasers

The magnitude of the relative frequency shift of a photothermal spectrometer increases with increasing absorbed power according to Eq. 4.13. In this section QCLs are used as the IR source to improve the magnitude of the relative frequency shift and to improve the overall performance. Applications of photothermal IR spectroscopy are explored further.

7.4.1 Metformin

Metformin is a widely used antidiabetic drug for the treatment of type 2 diabetes despite the uncertainty over its direct target [146, 147]. The latest theory is that the cellular effects of biguanides depend on their metal-binding properties. An interaction between biguanides and mitochondrial copper ions has been observed and reported to be crucial for the metabolic effects of metformin [148]. Fig. 7.27 shows the chemical structures of metformin and metformin-copper complex. Nanomechanical IR spectroscopy with string resonators has a great possibility to facilitate the study of the interaction between metformin and copper ions since it occurs often that newly developed and synthesized compounds are available in a very small amount for the characterization.

Fig. 7.28(a) shows an IR spectrum of metformin measured on a SiN string by nanomechanical IR spectroscopy. The strong and sharp peak at 1640 cm^{-1} derives from the stretching of carbon-nitrogen double bonds, the peak at 1545 cm^{-1} derives from the stretching of nitrogen-hydrogen bonds, and the broad peak at 1473 cm^{-1} derives from the stretching of carbon-hydrogen bonds [149].

Fig. 7.28(b) shows an IR sepctrum of copper-metformin complex obtained by adding copper nitrate to the metformin solution measured on a

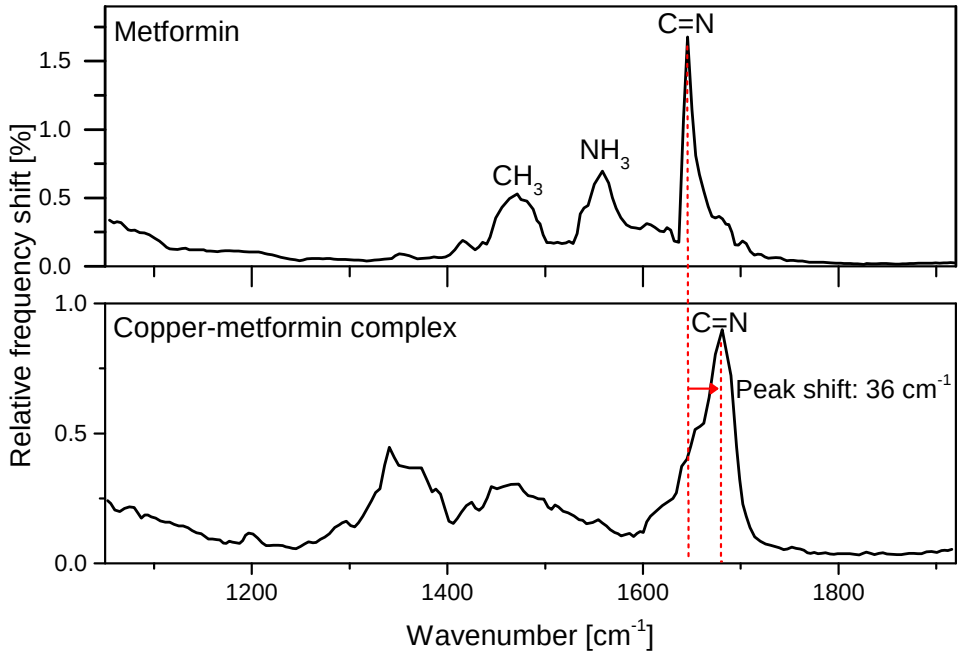

Figure 7.28: Copper chelation with metformin. IR spectrum measured by nanomechanical IR spectroscopy from 1050 cm^{-1} to 1920 cm^{-1} with a wavenumber resolution of 5 cm^{-1}. (a) IR spectrum of metformin with an area density of 205 mg/m^2 measured on a SiN string (100 µm long, 500 nm wide and 100 nm thick) with an IR laser duty cycle of 0.4%. (b) IR spectrum of of copper-metformin complex with an area density of 369 mg/m^2 measured on a SRN string (112 µm long, 5.0 µm wide and 185 nm thick) with an IR laser duty cycle of 0.25%.

SRN string by nanomechanical IR spectroscopy. The strong and sharp peak at 1687 cm^{-1} derives from the stretching of carbon-nitrogen double bonds, which has shifted to higher wavenumbers as a result of copper chelation with metformin. A new peak of medium intensity has appeared at 1329 cm^{-1} and it can be associated with the chelate ring formation by the metformin [150,151]. The observed peaks agree well with literatures [149–151].

The mass of a sample on a string can be calculated from the resonance frequency before sampling and after by Eq. 7.6. Assuming that the sample nanoparticles are uniformly collected on the string surface, the irradiated sample mass can be calculated from the length of the string and the diameter of the IR radiation and the total sample mass on a string. The IR source is equipped with a visible laser for alignment and the diameter of the IR laser foucused on a string is estimated from the size of the visible laser focused on a string which is approximately 25 µm. The total sample mass on the sring, the irradiated sample mass, and the area density for the metformin and for the copper-metformin complex are calculated to be 10 pg, 2.0 pg, 205 mg/m^2, 206 pg, 46 pg, and 369 mg/m^2, respectively. The metformin and copper-metformin complex solutions used to generate nanoparticles are

too dilute to obtain reference FTIR spectra.

7.4.2 Binary Mixtures

Polyvinylpyrrolidone (PVP) is used as a binder in many pharmaceutical tablets [152, 153], is one of the few approved water-soluble polymers, which has been clinically validated as safe, to increase drug solubility and drug stability or to enable targeting of drugs to tumors [154], and is even used to stabilize silica-based nanostructured particle systems [155] and iron-oxide nanoparticles [156] for nanomedicin applications.

Polystyrene (PS) is used as templates for nanoporous materials and filters. For example, a nanoporous membrane, fabricated with polystyrene-block-poly(methyl methacrylate) copolymer (PS-b-PMMA), has been introduced for for virus filtration [157]. Nanoporous membranes can be designed from drug delivery to water filtration [158]. Nanoporous PS fibres have shown 3 to 4 times higher oil sorption capacities than nonwoven polypropylene (PP) fibrous mats, that have been widely used in oil spill cleanup [159].

Fig. 7.29 shows SEM images of nanoparticles of a mixture of PS and PVP. The area where IR laser was irradiated is depicted with a blue circle in Fig. 7.29(a). Fig. 7.29(b) which is taken with a higher magnification shows that the nanoparticles on the right side of the string are arranged in a spacious manner and the nanoparticles on the left side of the string are rearranged in a denser manner where the IR laser was irradiated. It is probably because the heat generated by the sample due to the absorption of IR light does not heat only the string but also it heats the sample itself.

The temperature of the sample reaches its glass transition temperature, which gives a higher mobility to the PS and PVP nanoparticles and then the nanoparticles are fused and glued together. Nelson *et al* reported the PS softening temperature of 120 °C measured by nanoscale local thermal analysis techniques [160]. Glass transition temperature of PVP with its molecular weight of 10 kg/mol is reported to be ≈110 °C [161]. It can be deduced that the temperature of the polymers and the string has reached somewhere between 110 °C and 120 °C which is over the glass transition temperature of PVP and under the glass transition temperature of PS as PVP has behaved as liquid and PS has kept its sphere shape. Assuming that the heat is conducted via the string as the polymer does not cover the string completely, an absorbed power of 7.3 μW is calculated from Eq. 4.10 by inserting $\Delta T = 90$, $L = 99\times10^{-6}$, $A = 4.8\times10^{-13}$, and $\kappa = 2.1$.

This phenomenon was, however, not observed for the sample seen in Fig. 7.30, which had a lower relative sample area density compared to the string material. It can be anticipated that the heat generated by a sample of a smaller relative amount for a string is transferred directly or nearly directly from the substance to the string without heating up the sample itself as much and thus the temperature is kept under the glass transition

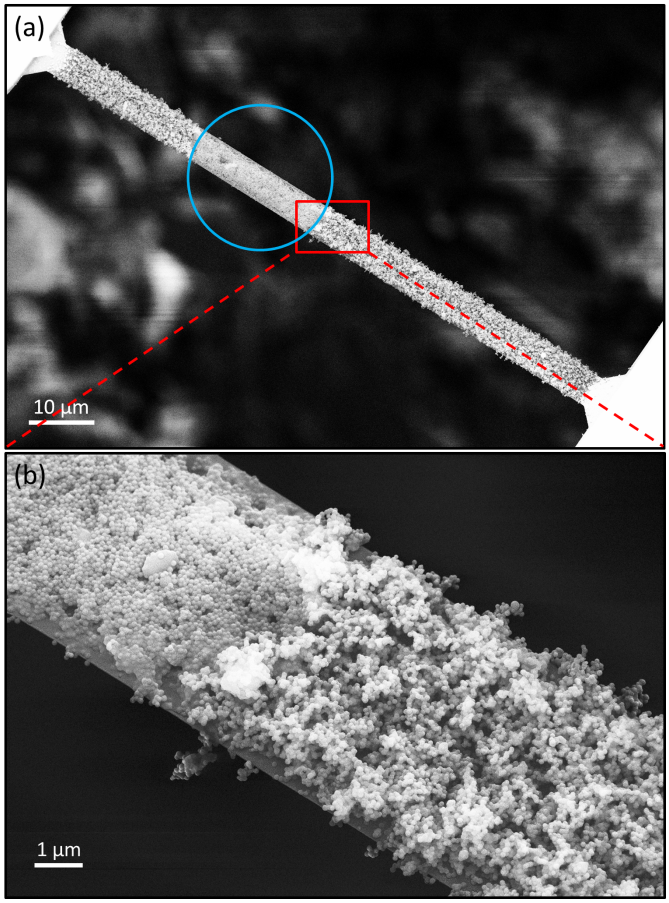

Figure 7.29: SEM images of nanoparticles of a mixture of PS and PVP of the ratio PS/PVP of 2.3 on a SiN string of 99 µm long, 4.8 µm wide and 100 nm thick. (a) The area where IR laser was irradiated is depicted with a blue circle. (b) Close-up of (a), showing nanoparticles deposited in a spacious manner on the right side of the string and nanoparticles rearranged in a denser manner in the IR irradiated area on the left side of the string.

temperature. It is therefore important to consider if a sample is sensitive to heat and not to deposit too much sample on a string when measuring a heat sensitive material. The diameter of the IR laser measured in the SEM image is approximately 20 µm which is in a good agreement with the estimation from the visible laser light.

The resonance frequency of the string shown in Fig. 7.30 before sampling the mixture of PS and PVP was 2.716 MHz and resonance frequency after the sampling was 1.808 MHz. The mass of the string of 100 µm long, 4.9 µm wide and 100 nm thick is calculated to be 152 pg assuming that the mass density of SiN is 3100 kg/m^3. Then the total sample mass on the sring becomes 85 pg. From the ratio of the length of the string and the diameter of the IR light, the irradiated sample mass is calculated to be 17 pg. The

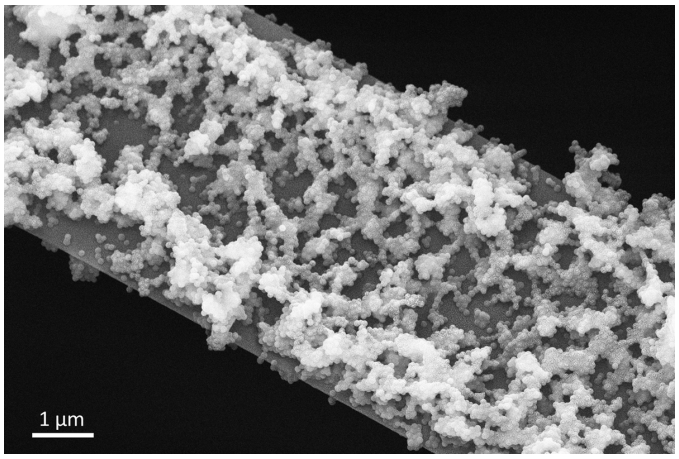

Figure 7.30: SEM image of a SiN string with PS and PVP nanoparticles of a mass ratio PS/PVP of 1.0. It is a 100 µm long, 4.9 µm wide and 100 nm thick SiN string.

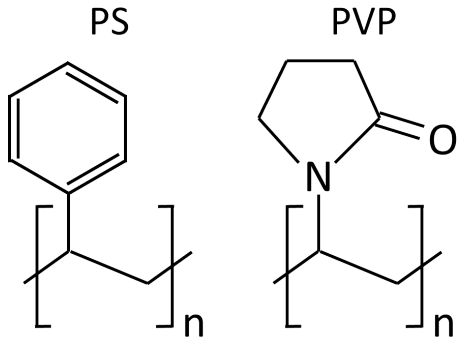

Figure 7.31: Repeat unit for PS (left) and for PVP (right).

sample area density can be calculated to be 173 mg/m^2.

No chemical reaction occurs when PVP is added to PS nanoparticles dispersed in water. Chemical structures of PS and PVP are shown in Fig. 7.31. Fig. 7.32(a) shows IR spectra of mixtures of PS and PVP nanoparticles of different ratios measured by nanomechanical IR spectroscopy in the left column and by FTIR in the right column. A strong and sharp peak at 1445 cm^{-1} caused by the stretching of the carbon-carbon bonds in the aromatic ring, another strong and sharp peak at 1484 cm^{-1} caused by the carbon-hydrogen bonds in the aromatic ring, and a medium peak at 1595 cm^{-1} caused by the the carbon-hydrogen bonds [162,163] are deriving from PS. A broad peak at 1288 cm^{-1} caused by the bending of the carbon-hydrogen bonds, a midium peak 1421 cm^{-1} caused by the carbon-nitrogen bonds, and a strong and broad peak at 1685 cm^{-1} caused by the carbon-oxygen double bonds [164–167] are deriving from PVP.

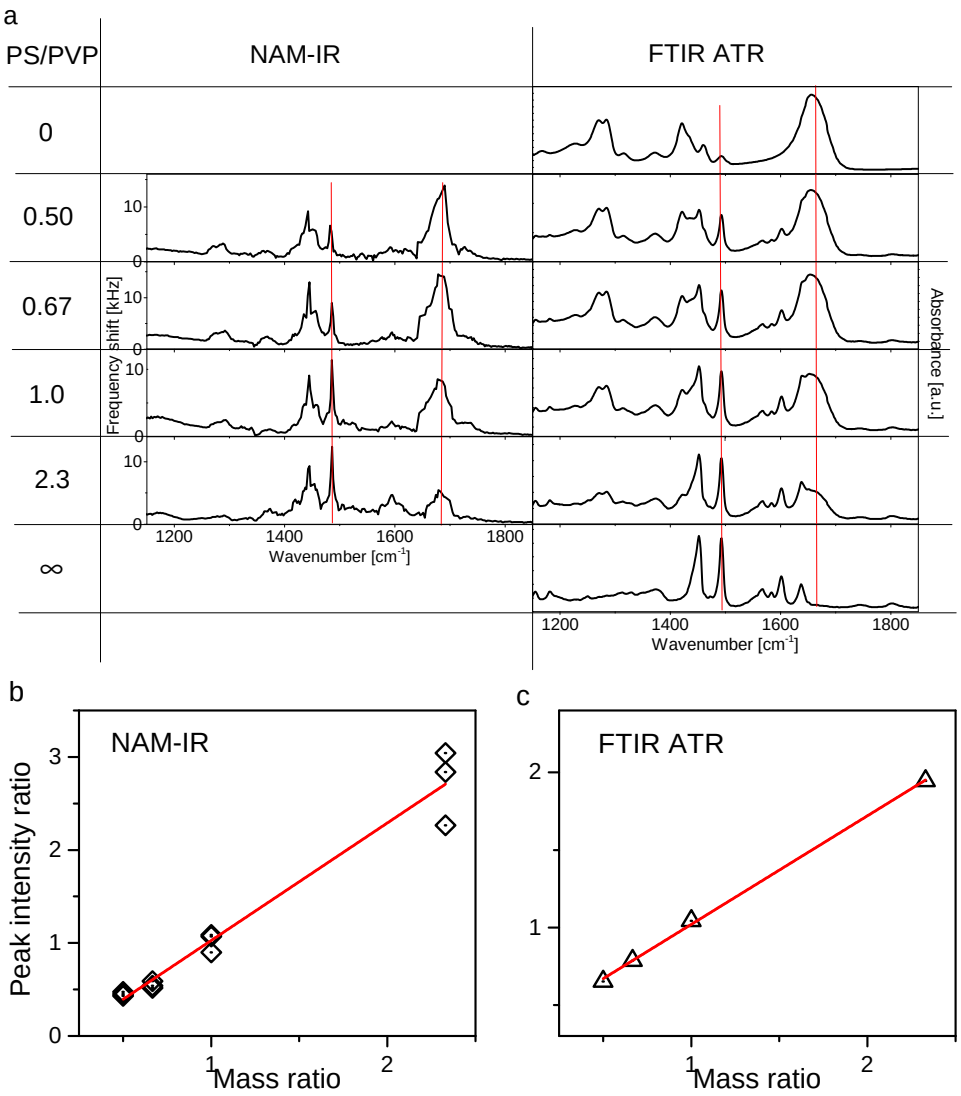

Figure 7.32: Mixtures of PS and PVP. (a) The left column shows the IR spectra of mixtures of PS and PVP with the mass ratios PS/PVP of 0.50, 0.67, 1.0 and 2.3 measured by nanomechanical IR spectroscopy (NAM-IR) using SiN strings. The right column shows the linear superpositions of individual IR spectra of PS and PVP of the ratios PS/PVP of 0, 0.50, 0.67, 1.0, 2.3 and ∞ measured by an FTIR spectrometer using an ATR accessory. All spectra are shown from 1150 to 1850 cm^{-1} as the wavenumbers lower than 1150 cm^{-1} were not scanned to avoid the strong and broad silicon nitride absoption peak at 904 cm^{-1} [122]. The NAM-IR data was obtained using SiN strings with the QCLs scanned from 1150 cm^{-1} to 1850 cm^{-1} with duty cycles of 3.1%, 3.4%, 5.0%, 5.0% for the PS/PVP ratios of 0.50, 0.67, 1.0, and 2.3, respectively. The highest duty cycles are chosen within the range of no saturation in the measured frequency signals. The measurements were conducted with a monochromatic IR light resolution of 1 cm^{-1}. Frequency shifts were extracted from the resonance frequency data and then normalized by the QCL power. The resolution of the NAM-IR spectra is $\sim$3 cm^{-1}. The FTIR ATR data was obtained by linearly superposing individual FTIR spectra of PS and PVP for the PS/PVP ratios of 0.50, 0.67, 1.0 and 2.3. (b)(c) PS/PVP peak intensity ratios as a function of PS/PVP mass ratios calculated from NAM-IR spectra and FTIR ATR spectra, respectively.

It can be seen that the relative peak intensities of the PS peaks against the PVP peaks are gradually increasing with the increasing ratio of PS. These peak positions and the change in the peak intensities in the nanomechanical IR spectra have been verified by means of conventional FTIR spectroscopy. Strong peaks such as the peaks at 1445 cm^{-1}, at 1484 cm^{-1} and at 1685 cm^{-1} appear to be sharper in the nanomechanical IR spectra compared to the FTIR spectra. The reason could be that FTIR collects much smaller intensity changes by a mid-IR detector in a large background which can lead to broader peaks compared to the nanomechanical IR peaks.

The ratios of PS/PVP peak intensity have been calculated from the normalized peak intensity of PS at 1484 cm^{-1} where there is no interference from PVP and the normalized peak intensity of PVP at 1685 cm^{-1} where there is no interference from PS. PS/PVP peak intensity ratios are plotted as a function of PS/PVP mass ratio in Fig. 7.32(b) for nanomechanical IR spectroscopy and (c) for FTIR ATR. The PS/PVP peak intensity ratio is increasing linearly with the increasing PS/PVP mass ratio in the nanomechanical IR analysis as well as in the FTIR ATR analysis. This can be used as a calibration curve for quantitative analysis of a mixture.

In order to calculate the minimum detectable mass of PS using the current experimental setup, we have chosen the IR radiation at 1495 cm^{-1} of 5.0% duty cycle for the further calculations. From Table 7.2, it can be calculated that the usage of the QCL adds 1.36 times as much noise as the usage of the thermal IR source. Thus we add the noise to the Allan deviation of 9.36×10^{-8} for the SiN string and it becomes 1.28×10^{-7}. The absorption peak at 1484 cm^{-1} of the nanomechanical IR spectrum of the mixture of PS/PVP ratio of 2.3 in Fig. 7.32(a) has been used to calculate the minimum detectable sample area density of PS using a SiN string. A sample area density has been adopted in order to be able to compare between strings with different dimensions since a sample mass is a function of string width. The induced frequency shift of 12376 Hz for a sample area density of 149 mg/m^2 relates to a relative frequency change of 4.97×10^{-2} m^2g^{-1} according to the measured resonance frequency of 1.67 MHz, which results in a minimum detectable area density of 7.7 $\mu g/m^2$ with an Allan deviation of $\sigma(1s) \approx 1.28 \times 10^{-7}$ for a signal-to-noise ratio of 3. This corresponds to 154 ag on a 1.0 μm wide string assuming the diameter of the IR laser of 20 μm.

The measurable absolute frequency shift is currently limited by the ability of PLL and we need to lower the duty cycle of the IR laser when an absorption peak has too high intensity for the PLL, which in turn lowers other absorption peaks as well. For qualitative and quantitative analyses of a mixture with an extreme ratio, this issue is to be overcome.

7.4.3 Summary - Photothermal Spectroscopy with QCL

This section has been used to present the results obtained by performing the photothermal IR spectroscopy with mechanical string resonators using QCLs as its IR source to improve the overall performace. Copper-chelation of the anti-diabetic drug metformin has been confirmed by the peak shift of carbon-nitrogen double bond by photothermal IR spectroscopy while it was not possible to obtain reference data with FTIR using the same sample solution. Moreover, photothermal IR spectra of binary mixtures of PS and PVP have shown a linear relationship between the mass ration and the peak intensity ratio of PS and PVP. The minimum detectable PS mass has been estimated to be 154 ag on a 1.0 μm wide SiN string assuming the diameter of the IR laser of 20 μm.

Chapter 8

Conclusion

The aim of this Ph.D. project was to develop new sensors that analyse engineered nanoparticles of different materials. Two different types of sensors have been studied: Toxicity sensor based on electrochemistry and photothermal spectroscopy with string resonators.

The possibility of miniaturization of toxicity sensor for engineered nanoparticles was explored based on the results of the biodurability test with redox activity measurements. First a stable pH was achieved by buffering Gamble's solution. Secondly it was found that platinum was more suitable to be used as a working electrode than gold for open circuit potential-time (OCPT) measurements. Then miniaturized platinum working electrodes were fabricated successfully. Thirdly quasi silver/silver chloride (Ag/AgCl) reference electrodes without potassium chloride (KCl) solution were fabricated to achieve more stable measurements. Lastly Gamble's solution with dispersed iron oxide (Fe_2O_3) nanoparticles showed approximately 20 mV lower potential than the ones without Fe_2O_3 nanoparticles. This result was however not reproducible even when using clean cells and electrodes. It was thus decided to focus on string-based sensors for photothermal spectroscopy.

The theory describing the undamped free vibration and the influence of tensile stress on the eigenfrequency of doubly-clamped beams has been presented. The expression for the eigenfrequency of strings has been modified to include the changes induced by heating the center of a string, including a bimaterial string. The principle of photothermal spectroscopy with mechanical string resonators has been presented. Combined with non-diffusion limited sampling, photothermal IR spectroscopy with mechanical string resonators provides vibrational signatures of analytes by measuring a frequency detuning of a string. Lastly some general theory of infrared spectroscopy has been presented.

The thermal IR source, Foxboro Miran 1A-CVF spectrophotometer, has its highest IR intensity around 2000 cm^{-1} and it ranges from 500 to 7500 cm^{-1}, whose shape of the broadband curve is close to the one for a blackbody at

1100 K. The filter wheel covers the wavelength range from 690 to 4000 cm^{-1} with two overlapping regions that are located from 1250 to 1266 cm^{-1} and from 2222 to 2273 cm^{-1}. The largest shift of 20.6 cm^{-1} was observed at 2222 cm^{-1} against a calibrated FTIR. The thermal IR source was replaced with a widely tunable mid-infrared laser source LaserTune to improve the magnitude of the relative frequency shift. This IR laser source has four modules and covers a wavenumber range of 925 to 1920 cm^{-1}. IR power of up to 3 mW was measured at module 1 and 2. The thermal IR source has a advantage of covering the whole mid-infrared range while the IR laser sourse is a powerful tool when analysing a smaller amount of samples.

Results from the analytical expression for photothermal frequency response have been compared to results obtained by FEM simulations. FEM simulations have shown that the frequency shift induced by local heating at the center of a string scales linearly with the inverse of the string width, with the inverse of the string thickness, with the string length, with the heating power and with the inverse of the thickness of the gold coating on a silicon nitride string. Based on the comparison, the analytical expression is considered valid for long and thin strings.

Silicon-rich silicon nitride (SRN) and stoichiometric silicon nitride (SiN) strings were fabricated successfully while fabrication of aluminium strings had an issue of polymer-like veils at the edges of aluminium strings which could not be removed or avoided with the currently available equipments at DTU Danchip. These silicon nitride strings have been used to demonstrate the sensing principle and that the relative frequency shift can be tailored in accordance to the analytical model. As the analytical model and the FEM simulations predicted, the experimental data has shown that the relative frequency shift is increasing linearly with decreasing string width, with decreasing string thickness, with increasing string length, and with increasing heating power. From a practical point of view, it is recommended for a string to have a minimum thickness of 100 nm, a minimum width of 1 μm, and a minimum length of 100 μm with a chip design of strings not too close to each other when reading out optically using the vibrometer and actuating a single frequency using the phased-locked loop (PLL).

A SiN string exhibits larger stress relaxation relative to its fast frequency shift and it requires a longer time to stabilise than a SRN string. The shorter stabilisation time of a SRN string is more desirable for photothermal spectroscopy. A chopper with an appropriate frequency would be helpful for this relaxation issue in order to obtain only the value of the first quick shift. It is of a great importance to have only the string irradiated and not the support for a faster response time. Using an IR laser allows us to irradiate only the string opposing to the thermal source that has a difficulty to avoid irradiating the support. It has been also shown from calculations that SRN strings have a shorter response time compared to SiN strings of the same length due to the higher thermal conductivity.

Frequency stability of the string resonators were investigated by calculating the Allan deviations. The lowest Allan deviation of $\sigma(1s) \approx 4.09 \times 10^{-9}$ was obtained from 110 μm long, 1.2 μm wide, and 185 nm thick SRN string, which is the shortest SRN string used in the experiments. While the thermal IR source does not add any noise to the frequency measurement, the QCL modules are obvious noise sources. It is important to use a higher readout laser power to obtain a good reflection for readout when a string width is smaller than the diameter of the readout laser. A SRN string has a better frequency resolution than a SiN string which is an important factor when investigating their detection limits. A short SRN string gives the best performance which can be attributed to the high frequency resolution. A better power resolution is obtained when the thermal source is used as its IR source as the QCL adds noise to the frequency measurements. The best power resolution has been obtained by using the shortest SRN string due to the highest frequency resolution.

The first photothermal IR spectroscopy with mechanical string resonators has been presented using a thermal IR source for chemical identification of the string material and airborne polyvinylpyrrolidone (PVP). The obtained IR spectra measured by photothermal spectroscopy match the state-of-the-art IR spectra measured by an FTIR spectrometer. Airborne species can directly be collected on the string resonator by means of in-situ non-diffusion limited sampling. Further we identified the organic coating of airborne titanium dioxide (TiO_2) nanoparticles, with a mass of 16 pg.

Photothermal IR spectroscopy with mechanical string resonators using QCLs as its IR source has been presented to improve the overall performace. Copper-chelation of the anti-diabetic drug metformin has been confirmed by the peak shift of carbon-nitrogen double bond by photothermal IR spectroscopy while it was not possible to obtain reference data with FTIR using the same sample solution due to the too low concentration of metformin. Moreover photothermal IR spectra of binary mixtures of polystyrene (PS) and PVP have shown a linear relationship between the mass ratio and the peak intensity ratio of PS and PVP. The minimum detectable PS mass has been estimated to be 154 ag on a 1.0 μm wide SiN string assuming the diameter of the IR laser of 20 μm.

From this project it can be concluded that photothermal IR spectroscopy with mechancial string resonators can be used to analyze nanoparticles in the air. Besides the primary purpose of work safety, this technique can also be useful for other applications such as pharmaceutical and polymer characterization.

Chapter 9

Outlook

There were many plans that could not be completed during this Ph.D. project. Other groups have also started to investigate different applications using photothermal spectroscopy with strings. Some of them are described below so that they can be kept in mind when exploring further applications.

9.1 pH Influence on Metformin and Analogues

The molecular mechanism of action of metformin is an important research area as metformin was discovered in the era before modern target-based drug discovery [147]. Repiščák *et al* investigated the bindings of metformin and propanediimidamide (PDI), which is structurally closely related to metformin, to copper by calculating the bond distances and angles and concluded that pK_a values (acid dissociation constant) and hydrophilicity of the compounds play a crucial roll in their cellular activity [168].

As it has been described in Section 7.4.1, photothermal spectroscopy with mechanical string resonators is useful to study the interaction between metformin and copper ions because it requires much smaller amount of samples for the analysis compared to the state-of-the-art FTIR technique. We have purchased two metformin analogues: phenformin and PDI and their chemical structures are shown in Fig. 9.1. We would like to investigate the bindings of those compounds to copper at different pH and this new knowledge could lead to development of some new drugs for type 2 diabetes.

9.2 Bio-Molecules on Gold Surface

Adding an extra layer of another material on a string could be significant for functionalizing the surface to attract specific molecules, or to add a material that tailors the optical or thermal properties of the string as discussed in Section 7.2.1. Gold is one of the most common surfaces to immobilize biomolecules.

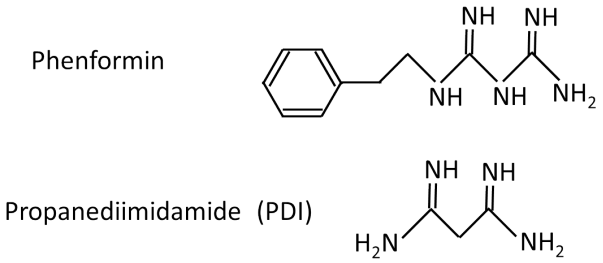

Figure 9.1: Chemical structures of phenformin and propanediimidamide (PDI).

Sensitive and specific sensor systems are necessary to be developed to detect ultra-low level of medical residues in the biosensor industry. For example, the female sexhormone 17β-estradiol is commonly used in contraceptive pills from where it find its way through waste water treatment plants and into the environment. The hormone has been heavily studied and there is a need for sensitive sensors. Selective 17β-estradiol biosensors using aptamer have been demonstrated electrochemically [169], optically [170], calorimetrically with a detection limit of 200 pM using gold nanoparticles [171], and using surface enhanced Raman spectroscopy (SERS) [172].

We have started exploring this application by functionalising gold surface on strings with aptamer. Fig. 9.2 shows a schematic of the functionalisation strategy. Aptamer is physically adsorbed onto the gold surface (a,b). The thiol group of the aptamer binds to the gold surface through incubation (c). Small molecule 6-mercapto-1-hexanol (MCH), which quickly forms self-assembled monolayers (SAMs) on the gold surface, prevents unspecific binding of other molecules (d). Proper folding of the aptamer allows to obtain selective aptamer-target binding (e). The complete protocol is given in Appendix F.

Fig. 9.3 shows one of the first results with aptamer on gold surface. The string was coated with gold by e-beam deposition. The absorption peak at 985 cm^{-1} can be associated with carbon-carbon backbone, the peak at 1025 cm^{-1} with furanose, and the peak at 1215 cm^{-1} with phosphate. [173] It is also possible to coat a string with gold nanoparticles using a nebulizer instead of e-beam deposition. In this way an adhesion layer between the string material and gold layer can be avoided. We believe that monolayer of bio-molecules can be analysed with photothermal spectroscopy with mechanical strings when we can overcome the sensitivity of gold surface to contaminants.

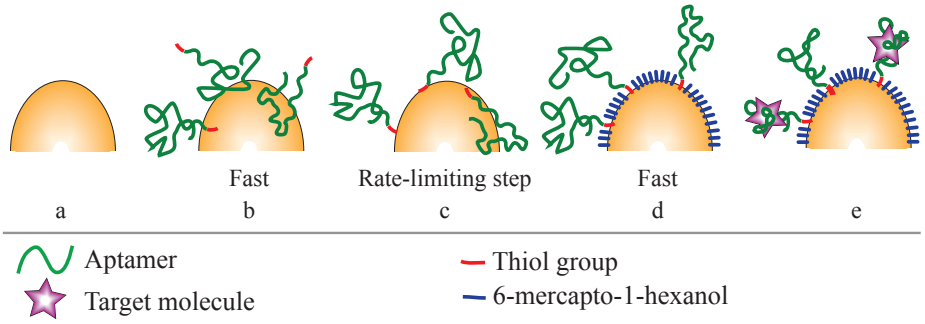

Figure 9.2: Schematic of the functionalisation strategy. Aptamer is physically adsorbed to the gold surface (a,b). Incubation allows the thiol group of the aptamer to bind to the gold surface (c). Unspecific binding is prevented by 6-mercapto-1-hexanol (MCH), which quickly form self-assembled monolayers (SAMs) on the gold surface (d). Aptamer-target capture is achieved by proper folding of the aptamer (e). This figure is provided by Kasper Bayer Frøhling.

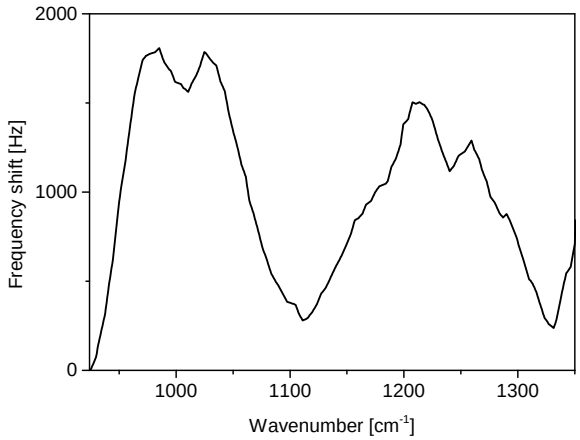

Figure 9.3: Nanomechanical IR spectrum of DNA aptamer on gold surface. The absorption peak at 985 cm^{-1} can be associated with carbon-carbon backbone, the peak at 1025 cm^{-1} with furanose, and the peak at 1215 cm^{-1} with phosphate.

Figure 9.4: Field sampling at Nørreport station in Copenhagen. The sampling box consists of an impactor to remove particles larger than 500 nm, a deposition chamber where a chip with strings is placed, and a battery-driven pump.

9.3 Nanoparticulate in Diesel Exhaust

Many of the InterCity trains in Denmark are currently diesel-powered. Nørreport station, one of the largest stations in Copenhagen, is built underground and one can clearly smell the exhaust at the platform for a long time after InterCity trains have departed. Miller *et al* reported that long-term exposure to air pollution, especially the combustion-derived nanoparticulate in diesel exhaust, increases the risk of death from cardiovascular disease by 76% [174, 175]. Many studies on analysis of diesel nanoparticles have been conducted not only using electron microscopes [176] but also using mass spectrometry [177], volatilization and humidification tandem differential mobility analysis (VH-TDMA) [178], etc.

We have assembled a field sampling box consisting of an impactor to remove particles larger than 500 nm, a deposition chamber where a chip with strings is placed, and a battery-driven pump. A picture of field sampling at Nørreport station is shown in Fig. 9.4. With a sampling time of 3 minutes, too much material was collected on the string and the string did not behave as a string. With a sampling time of 1 minute, the string behaved as a string and thus the amount of collected material was appropriate. As most of the collected material was, however, desorbed at a lower pressure in the measurement chamber. The major component was likely to be nitrogen oxides [179]. Photothermal spectroscopy with string resonators has a potential to become a real-time chemical analysis instrument for diesel exhaust application when portability is realised.

Bibliography

[1] Andrew D. Maynard, David B. Warheit, and Martin A. Philbert. The New Toxicology of Sophisticated Materials: Nanotoxicology and Beyond. *Toxicological Sciences*, page kfq372, December 2010.

[2] Gnter Oberdrster, Eva Oberdrster, and Jan Oberdrster. Nanotoxicology: an emerging discipline evolving from studies of ultrafine particles. *Environmental health perspectives*, pages 823–839, 2005.

[3] Jasmine Jia'en Li, Sindu Muralikrishnan, Cheng-Teng Ng, Lin-Yue Lanry Yung, and Boon-Huat Bay. Nanoparticle-induced pulmonary toxicity. *Experimental biology and medicine*, 235(9):1025–1033, 2010.

[4] A.T. Saber, K.A. Jensen, N.R. Jacobsen, R. Birkedal, L. Mikkelsen, P. Mller, S. Loft, H. Wallin, and U. Vogel. Inflammatory and genotoxic effects of nanoparticles designed for inclusion in paints and lacquers. *Nanotoxicology*, 6:453–471, 2012. 5.

[5] Cristina Buzea, Ivan I Pacheco, and Kevin Robbie. Nanomaterials and nanoparticles: sources and toxicity. *Biointerphases*, 2:MR17–MR71, 2007. 4.

[6] Andrew Maynard, Robert J. Aitken, Tilman Butz, Vicki Colvin, Ken Donaldson, Gnter Oberdrster, Martin A. Philbert, John Ryan, Anthony Seaton, Vicki Stone, and others. Safe handling of nanotechnology. *NATURE-LONDON-*, 444(7117):267, 2006.

[7] T Kuhlbusch, Christof Asbach, Heinz Fissan, Daniel Ghler, and Michael Stintz. Nanoparticle exposure at nanotechnology workplaces: a review. *Part Fibre Toxicol*, 8:22, 2011. 1.

[8] Hermine Nguea, Aymon de Reydellet, Alain Le Faou, Mohamed Zaiou, and Bertrand Rihn. Macrophage Culture as a Suitable Paradigm for Evaluation of Synthetic Vitreous Fibers. *Critical Reviews in Toxicology*, 38(8):675–695, January 2008.

[9] Paige N. Wiecinski, Kevin M. Metz, Andrew N. Mangham, Kurt H. Jacobson, Robert J. Hamers, and Joel A. Pedersen. Gastrointestinal biodurability of engineered nanoparticles: Development of an in vitro assay. *Nanotoxicology*, 3(3):202–214, January 2009.

[10] S. M. Hussain, K. L. Hess, J. M. Gearhart, K. T. Geiss, and J. J. Schlager. In vitro toxicity of nanoparticles in BRL 3a rat liver cells. *Toxicology in Vitro*, 19(7):975–983, October 2005.

[11] L. C. Renwick, K. Donaldson, and A. Clouter. Impairment of Alveolar Macrophage Phagocytosis by Ultrafine Particles. *Toxicology and Applied Pharmacology*, 172(2):119–127, April 2001.

[12] Yuzuki Nakagawa, Shinobu Wakuri, Kyoko Sakamoto, and Noriho Tanaka. The photogenotoxicity of titanium dioxide particles. *Mutation Research/Genetic Toxicology and Environmental Mutagenesis*, 394(13):125–132, November 1997.

[13] Thomas C. Long, Navid Saleh, Robert D. Tilton, Gregory V. Lowry, and Bellina Veronesi. Titanium Dioxide (P25) Produces Reactive Oxygen Species in Immortalized Brain Microglia (BV2): Implications for Nanoparticle Neurotoxicity. *Environmental Science & Technology*, 40(14):4346–4352, July 2006.

[14] Margareth RC Marques, Raimar Loebenberg, and May Almukainzi. Simulated biological fluids with possible application in dissolution testing. *Dissolution Technol*, 18(3):15–28, 2011.

[15] K. Vijayamohanan, A. K. Shukla, and S. Sathyanarayana. Open-circuit potentialtime transients of alkaline porous iron electrodes at various states-of-charge. *Electrochimica Acta*, 36(2):369–380, 1991.

[16] P. Novak, P. A. Christensen, T. Iwasita, and W. Vielstich. Anodic oxidation of propylene carbonate on platinum, glassy carbon and polypyrrole: An in-situ FTIR study. *Journal of Electroanalytical Chemistry and Interfacial Electrochemistry*, 263(1):37–48, May 1989.

[17] Yen Wei, Kesyin F. Hsueh, and Guang-Way Jang. Monitoring the chemical polymerization of aniline by open-circuit-potential measurements. *Polymer*, 35(16):3572–3575, August 1994.

[18] Chuan-Jian Zhong, Nina T. Woods, G. Brent Dawson, and Marc D. Porter. Formation of thiol-based monolayers on gold: implications from open circuit potential measurements. *Electrochemistry Communications*, 1(1):17–21, January 1999.

[19] Arto R. Heiskanen, Christer F. Spgel, Natalie Kostesha, Tautgirdas Ruzgas, and Jenny Emnus. Monitoring of Saccharomyces cerevisiae Cell Proliferation on Thiol-Modified Planar Gold Microelectrodes Using Impedance Spectroscopy. *Langmuir*, 24(16):9066–9073, August 2008.

[20] Jing Kang and Paul A. Rowntree. Gold Film Surface Preparation for Self-Assembled Monolayer Studies. *Langmuir*, 23(2):509–516, January 2007.

[21] Lee M. Fischer, Maria Tenje, Arto R. Heiskanen, Noriyuki Masuda, Jaime Castillo, Anders Bentien, Jenny mneus, Mogens H. Jakobsen, and Anja Boisen. Gold cleaning methods for electrochemical detection applications. *Microelectronic engineering*, 86(4):1282–1285, 2009.

[22] J. C. Hoogvliet, M. Dijksma, B. Kamp, and W. P. Van Bennekom. Electrochemical pretreatment of polycrystalline gold electrodes to produce a reproducible surface roughness for self-assembly: a study in phosphate buffer pH 7.4. *Analytical chemistry*, 72(9):2016–2021, 2000.

[23] Nicholas C. Thomas. The early history of spectroscopy. *Journal of Chemical Education*, 68(8):631, August 1991.

[24] Sir Isaac Newton. *Opticks: Or, a Treatise of the Reflections, Refractions, Inflections, and Colors of Light: Or, a Treatise of the Reflections, Refractions, Inflections, and Colors of Light.* Digireads.com Publishing, September 2011.

[25] William Hyde Wollaston. A Method of Examining Refractive and Dispersive Powers, by Prismatic Reflection. *Philosophical Transactions of the Royal Society of London*, 92:365–380, January 1802.

[26] M.E. Schaepman, R.O. Green, S.G. Ungar, B. Curtiss, J. Boardman, A.J. Plaza, Bo-Cai Gao, S. Ustin, R. Kokaly, J.R. Miller, S. Jacquemoud, E. Ben-Dor, R. Clark, C. Davis, J. Dozier, D.G. Goodenough, D. Roberts, G. Swayze, E.J. Milton, and A. F H Goetz. The Future of Imaging Spectroscopy Prospective Technologies and Applications. In *IEEE International Conference on Geoscience and Remote Sensing Symposium, 2006. IGARSS 2006*, pages 2005–2009, 2006.

[27] Joseph Fraunhofer and J. Ames. Determination of the Refractive and the Dispersive Power of Different Kinds of Glass, with Reference to the Perfecting of Achromatic Telescopes. *Prismatic and Diffraction Spectra (New York: Harper & Brothers, 1898)*, pages 1–10, 1817.

[28] Captain Abney and Lieut-Colonel Festing. On the influence of the atomic grouping in the molecules of organic bodies on their absorption

in the infra-red region of the spectrum. *Philosophical Transactions of the Royal Society of London*, 172:887–918, 1881.

[29] Donald Pavia, Gary Lampman, George Kriz, and James Vyvyan. *Introduction to Spectroscopy*. Cengage Learning, March 2008.

[30] D. N. Sathyanarayana. *Vibrational Spectroscopy: Theory And Applications*. New Age International, January 2007.

[31] Barbara Stuart. Infrared Spectroscopy. In *Kirk-Othmer Encyclopedia of Chemical Technology*. John Wiley & Sons, Inc., 2000.

[32] Paul Muralt. Micromachined infrared detectors based on pyroelectric thin films. *Reports on Progress in Physics*, 64(10):1339, October 2001.

[33] Lisa M. Miller and Randy J. Smith. Synchrotrons versus globars, point-detectors versus focal plane arrays: Selecting the best source and detector for specific infrared microspectroscopy and imaging applications. *Vibrational Spectroscopy*, 38(12):237–240, July 2005.

[34] Matthew J. Baker, Jlio Trevisan, Paul Bassan, Rohit Bhargava, Holly J. Butler, Konrad M. Dorling, Peter R. Fielden, Simon W. Fogarty, Nigel J. Fullwood, Kelly A. Heys, Caryn Hughes, Peter Lasch, Pierre L. Martin-Hirsch, Blessing Obinaju, Ganesh D. Sockalingum, Josep Sul-Suso, Rebecca J. Strong, Michael J. Walsh, Bayden R. Wood, Peter Gardner, and Francis L. Martin. Using Fourier transform IR spectroscopy to analyze biological materials. *Nature Protocols*, 9(8):1771–1791, August 2014.

[35] Peter R. Griffiths and James A. De Haseth. *Fourier Transform Infrared Spectrometry*. John Wiley & Sons, March 2007.

[36] Giuseppe Zerbi, Heinz W. Siesler, Isao Noda, Mitsuo Tasumi, and Samuel Krimm. *Modern Polymer Spectroscopy*. John Wiley & Sons, July 2008.

[37] J. L. Koenig. *Spectroscopy of Polymers*. Elsevier, September 1999.

[38] D. I. Bower. *The Vibrational Spectroscopy of Polymers*. Cambridge University Press, July 1992.

[39] Hans-Ulrich Gremlich and Bing Yan. *Infrared and Raman Spectroscopy of Biological Materials*. CRC Press, September 2000.

[40] Dieter Naumann. Ft-Infrared and Ft-Raman Spectroscopy in Biomedical Research. *Applied Spectroscopy Reviews*, 36(2-3):239–298, June 2001.

[41] Wolfgang Petrich. Mid-Infrared and Raman Spectroscopy for Medical Diagnostics. *Applied Spectroscopy Reviews*, 36(2-3):181–237, June 2001.

[42] Yves Roggo, Pascal Chalus, Lene Maurer, Carmen Lema-Martinez, Aurlie Edmond, and Nadine Jent. A review of near infrared spectroscopy and chemometrics in pharmaceutical technologies. *Journal of Pharmaceutical and Biomedical Analysis*, 44(3):683–700, July 2007.

[43] Brian G. Osborne. Near-Infrared Spectroscopy in Food Analysis. In *Encyclopedia of Analytical Chemistry*. John Wiley & Sons, Ltd, 2006.

[44] Satoru Tsuchikawa. A Review of Recent Near Infrared Research for Wood and Paper. *Applied Spectroscopy Reviews*, 42(1):43–71, February 2007.

[45] S. Prati, E. Joseph, G. Sciutto, and R. Mazzeo. New Advances in the Application of FTIR Microscopy and Spectroscopy for the Characterization of Artistic Materials. *Accounts of Chemical Research*, 43(6):792–801, June 2010.

[46] Cyril Muehlethaler, Genevieve Massonnet, and Pierre Esseiva. The application of chemometrics on Infrared and Raman spectra as a tool for the forensic analysis of paints. *Forensic Science International*, 209(13):173–182, June 2011.

[47] Peter R Solomon and Robert M Carangelo. FTIR analaysis of coal. 1. techniques and determination of hydroxyl concentrations. *Fuel*, 61:663–669, 1982. 7.

[48] Stephen Bialkowski. *Photothermal Spectroscopy Methods for Chemical Analysis*. John Wiley & Sons, 1996.

[49] J. Sell. *Photothermal Investigations of Solids and Fluids*. Elsevier, December 2012.

[50] George H. Brilmyer, Akira Fujishima, K. S. V. Santhanam, and Allen J. Bard. Photothermal spectroscopy. *Analytical Chemistry*, 49(13):2057–2062, November 1977.

[51] George H. Brilmyer and Allen J. Bard. Application of photothermal spectroscopy to in-situ studies of films on metals and electrodes. *Analytical Chemistry*, 52(4):685–691, April 1980.

[52] A. Rosencwaig. Photoacoustic spectroscopy. New tool for investigation of solids. *Analytical Chemistry*, 47(6):592A–604a, May 1975.

[53] W. B. Jackson, N. M. Amer, A. C. Boccara, and D. Fournier. Photothermal deflection spectroscopy and detection. *Applied Optics*, 20(8):1333, April 1981.

[54] J. M. R. Weaver. Optical absorption microscopy and spectroscopy with nanometre resolution. *Nature*, 342(6251):783–785, 1989.

[55] T. Kunii. Temperature dependence of absorption coefficient spectra for mu c-Si films by resonant photothermal bending spectroscopy. *Solar Energy Materials and Solar Cells*, 74(1-4):415–420, 2002.

[56] Minhyuk Yun, Seonghwan Kim, Dongkyu Lee, Namchul Jung, Inseok Chae, Sangmin Jeon, and Thomas Thundat. Photothermal cantilever deflection spectroscopy of a photosensitive polymer. *Applied Physics Letters*, 100:204103–204103–4, 2012. 20.

[57] J. R. Barnes, R. J. Stephenson, M. E. Welland, C. Gerber, and J. K. Gimzewski. Photothermal spectroscopy with femtojoule sensitivity using a micromechanical device. *Nature*, 372:79–81, 1994. 6501.

[58] JR Barnes, RJ Stephenson, CN Woodburn, SJ Oshea, ME Welland, T. Rayment, JK Gimzewski, and C. Gerber. A femtojoule calorimeter using micromechanical sensors. *Review of Scientific Instruments*, 65:3793–3798, 1994. 12.

[59] Guangming Li, Larry W Burggraf, and William P Baker. Photothermal spectroscopy using multilayer cantilever for chemical detection. *Applied Physics Letters*, 76:1122–1124, 2000. 9.

[60] P. G. Datskos, S. Rajic, M. J. Sepaniak, N. Lavrik, C. A. Tipple, L. R. Senesac, and I. Datskou. Chemical detection based on adsorption-induced and photoinduced stresses in microelectromechanical systems devices. *Journal of Vacuum Science & Technology B*, 19(4):1173–1179, July 2001.

[61] P. G Datskos, M. J Sepaniak, C. A Tipple, and N Lavrik. Photomechanical chemical microsensors. *Sensors and Actuators B: Chemical*, 76(13):393–402, June 2001.

[62] E. T. Arakawa, N. V. Lavrik, S. Rajic, and P. G. Datskos. Detection and differentiation of biological species using microcalorimetric spectroscopy. *Ultramicroscopy*, 97:459–466, 2003. 1.

[63] A. R. Krause, C. Van Neste, L. Senesac, T. Thundat, and E. Finot. Trace explosive detection using photothermal deflection spectroscopy. *Journal of Applied Physics*, 103:094906–094906–6, 2008. 9.

[64] Larry Senesac and Thomas G Thundat. Nanosensors for trace explosive detection. *Materials Today*, 11:28–36, 2008. 3.

[65] A. Wig, E. T. Arakawa, A. Passian, T. L. Ferrell, and T. Thundat. Photothermal spectroscopy of Bacillus anthracis and Bacillus cereus with microcantilevers. *Sensors and Actuators B: Chemical*, 114(1):206–211, March 2006.

[66] Seonghwan Kim, Dongkyu Lee, Xunchen Liu, Charles Van Neste, Sangmin Jeon, and Thomas Thundat. Molecular recognition using receptor-free nanomechanical infrared spectroscopy based on a quantum cascade laser. *Scientific Reports*, 3, January 2013.

[67] Dongkyu Lee, Seonghwan Kim, Sangmin Jeon, and Thomas Thundat. Direct Detection and Speciation of Trace Explosives Using a Nanoporous Multifunctional Microcantilever. *Analytical Chemistry*, 86(10):5077–5082, May 2014.

[68] M. Faheem Khan, Seonghwan Kim, Dongkyu Lee, Silvan Schmid, Anja Boisen, and Thomas Thundat. Nanomechanical identification of liquid reagents in a microfluidic channel. *Lab on a Chip*, 14(7):1302–1307, March 2014.

[69] C. W. Van Neste, L. R. Senesac, D. Yi, and T. Thundat. Standoff detection of explosive residues using photothermal microcantilevers. *Applied Physics Letters*, 92(13):134102, March 2008.

[70] L. A. Skvortsov. Application of laser photothermal spectroscopy for standoff detection of trace explosive residues on surfaces. *Quantum Electronics*, 40(7):565–578, 2010.

[71] Minhyuk Yun, Changyong Yim, Namchul Jung, Seonghwan Kim, Thomas Thundat, and Sangmin Jeon. Nanomechanical Thermal Analysis of Photosensitive Polymers. *Macromolecules*, 44(24):9661–9665, December 2011.

[72] Seonghwan Kim, Dongkyu Lee, Minhyuk Yun, Namchul Jung, Sangmin Jeon, and Thomas Thundat. Multi-modal characterization of nanogram amounts of a photosensitive polymer. *Applied Physics Letters*, 102(2):024103, January 2013.

[73] Seonghwan Kim, Dongkyu Lee, and Thomas Thundat. Photothermal cantilever deflection spectroscopy. *EPJ Techniques and Instrumentation*, 1(1):1–12, December 2014.

[74] YT Yang, Carlo Callegari, XL Feng, KL Ekinci, and ML Roukes. Zeptogram-scale nanomechanical mass sensing. *Nano letters*, 6(4):583–586, 2006.

[75] Silvan Schmid, Soren Dohn, and Anja Boisen. Real-Time Particle Mass Spectrometry Based on Resonant Micro Strings. *Sensors (Basel, Switzerland)*, 10(9):8092–8100, August 2010.

[76] Silvan Schmid, Maksymilian Kurek, Jens Q. Adolphsen, and Anja Boisen. Real-time single airborne nanoparticle detection with nanomechanical resonant filter-fiber. *Scientific Reports*, 3, February 2013.

[77] Silvan Schmid, Maksymilian Kurek, and Anja Boisen. Towards airborne nanoparticle mass spectrometry with nanomechanical string resonators. volume 8725, pages 872525–872525–8, 2013.

[78] MS Hanay, S Kelber, AK Naik, D Chi, S Hentz, EC Bullard, E Colinet, L Duraffourg, and ML Roukes. Single-protein nanomechanical mass spectrometry in real time. *Nature nanotechnology*, 7(9):602–608, 2012.

[79] AK Naik, MS Hanay, WK Hiebert, XL Feng, and ML Roukes. Towards single-molecule nanomechanical mass spectrometry. *Nature nanotechnology*, 4(7):445–450, 2009.

[80] Thomas P Burg, Michel Godin, Scott M Knudsen, Wenjiang Shen, Greg Carlson, John S Foster, Ken Babcock, and Scott R Manalis. Weighing of biomolecules, single cells and single nanoparticles in fluid. *Nature*, 446(7139):1066–1069, 2007.

[81] J. Chaste, A. Eichler, J. Moser, G. Ceballos, R. Rurali, and A. Bachtold. A nanomechanical mass sensor with yoctogram resolution. *Nature Nanotechnology*, 7(5):301–304, May 2012.

[82] K Jensen, Kwanpyo Kim, and A Zettl. An atomic-resolution nanomechanical mass sensor. *Nature nanotechnology*, 3(9):533–537, 2008.

[83] Jay W. Grate. Acoustic Wave Microsensor Arrays for Vapor Sensing. *Chemical Reviews*, 100(7):2627–2648, July 2000.

[84] T. Larsen, S. Schmid, L. Grnberg, A. O. Niskanen, J. Hassel, S. Dohn, and A. Boisen. Ultrasensitive string-based temperature sensors. *Applied Physics Letters*, 98(12):121901, March 2011.

[85] T. Larsen, S. Schmid, and A. Boisen. Micro string resonators as temperature sensors. In *AIP Conference Proceedings*, volume 1552, pages 931–936. AIP Publishing, September 2013.

[86] Tom Larsen, Silvan Schmid, Luis G. Villanueva, and Anja Boisen. Photothermal Analysis of Individual Nanoparticulate Samples Using Micromechanical Resonators. *ACS Nano*, 7(7):6188–6193, July 2013.

[87] Anja Boisen, Sren Dohn, Stephan Sylvest Keller, Silvan Schmid, and Maria Tenje. Cantilever-like micromechanical sensors. *Reports on Progress in Physics*, 74(3):036101, March 2011.

[88] Brian C. Smith. *Fundamentals of Fourier Transform Infrared Spectroscopy, Second Edition*. CRC Press, March 2011.

[89] Patty Feist. Infrared Spectroscopy: Theory, 2002. http://orgchem.colorado.edu/Spectroscopy/irtutor/IRtheory.pdf.

[90] S. Timoshenko. VIBRATION PROBLEMS IN ENGINEERING. 1974.

[91] Harrie A. C. Tilmans, Miko Elwenspoek, and Jan H. J. Fluitman. Micro resonant force gauges. *Sensors and Actuators A: Physical*, 30(12):35–53, January 1992.

[92] En-Chiang Lin, Jun Fang, Se-Chul Park, Forrest W Johnson, and Heiko O Jacobs. Effective localized collection and identification of airborne species through electrodynamic precipitation and SERS-based detection. *Nature communications*, 4:1636, 2013.

[93] Paul E. Sheehan and Lloyd J. Whitman. Detection Limits for Nanoscale Biosensors. *Nano Letters*, 5(4):803–807, April 2005.

[94] Todd M. Squires, Robert J. Messinger, and Scott R. Manalis. Making it stick: convection, reaction and diffusion in surface-based biosensors. *Nature Biotechnology*, 26(4):417–426, April 2008.

[95] James M Olson. Analysis of LPCVD process conditions for the deposition of low stress silicon nitride. Part I: preliminary LPCVD experiments. *Materials Science in Semiconductor Processing*, 5(1):51–60, February 2002.

[96] Pasqualina M Sarro. Silicon carbide as a new MEMS technology. *Sensors and Actuators A: Physical*, 82(13):210–218, May 2000.

[97] X. M. H. Huang, X. L. Feng, C. A. Zorman, M. Mehregany, and M. L. Roukes. VHF, UHF and microwave frequency nanomechanical resonators. *New Journal of Physics*, 7(1):247, November 2005.

[98] E.J. Boyd and D. Uttamchandani. Measurement of the Anisotropy of Young's Modulus in Single-Crystal Silicon. *Journal of Microelectromechanical Systems*, 21(1):243–249, February 2012.

[99] M. Stadtmeller. Mechanical Stress of CVDDielectrics. *Journal of The Electrochemical Society*, 139(12):3669–3674, December 1992.

[100] M. T. Alam, M. P. Manoharan, M. A. Haque, C. Muratore, and A. Voevodin. Influence of strain on thermal conductivity of silicon nitride thin films. *Journal of Micromechanics and Microengineering*, 22(4):045001, April 2012.

[101] DTU Danchip. Deposition of stoichiometric nitride using the 6" LPCVD nitride furnace, April 2014. http://labadviser.danchip.dtu.dk/index.php/Specific_Process_Knowledge/Thin_film_deposition/Furnace_LPCVD_Nitride /Deposition_of_stoichiometric_nitride_using_the_6%22_LPCVD_nitride_furnace [Accessed 2014-08-22].

[102] Jovan Matovi and Zoran Jaki. A comparative analyze of fundamental noise in cantilever sensors based on lateral and longitudinal displacement: case of thermal infrared detectors. *Microsystem Technologies*, 16(5):755–763, March 2010.

[103] C. H. Mastrangelo. Thermophysical properties of low-residual stress, silicon-rich, LPCVD silicon nitride films. *Sensors and Actuators a (Physical)*, A23(1-3):856–880, 1990.

[104] A Kaushik, Harold Kahn, and AH. Heuer. Wafer-level mechanical characterization of silicon nitride MEMS. *Journal of Microelectromechanical Systems*, 14(2):359–367, April 2005.

[105] Yasumasa Okada and Yozo Tokumaru. Precise determination of lattice parameter and thermal expansion coefficient of silicon between 300 and 1500 K. *Journal of Applied Physics*, 56(2):314–320, July 1984.

[106] N. Stojanovic, Jongsin Yun, E.B.K. Washington, J.M. Berg, M.W. Holtz, and Henryk Temkin. Thin-Film Thermal Conductivity Measurement Using Microelectrothermal Test Structures and Finite-Element-Model-Based Data Analysis. *Journal of Microelectromechanical Systems*, 16(5):1269–1275, October 2007.

[107] T. F. Retajczyk Jr. and A. K. Sinha. Elastic stiffness and thermal expansion coefficients of various refractory silicides and silicon nitride films. *Thin Solid Films*, 70(2):241–247, August 1980.

[108] Kamili M. Jackson. Fracture strength, elastic modulus and Poisson's ratio of polycrystalline 3c thin-film silicon carbide found by microsample tensile testing. *Sensors and Actuators A: Physical*, 125(1):34–40, October 2005.

[109] Michael E. Levinshtein, Sergey L. Rumyantsev, and Michael S. Shur. *Properties of Advanced Semiconductor Materials: GaN, AIN, InN, BN, SiC, SiGe.* John Wiley & Sons, February 2001.

[110] S. Schmid, K. D. Jensen, K. H. Nielsen, and A. Boisen. Damping mechanisms in high-Q micro and nanomechanical string resonators. *Physical Review B*, 84:165307, 2011. 16.

[111] S. Habermehl. Stress relaxation in Si-rich silicon nitride thin films. *Journal of Applied Physics*, 83(9):4672–4677, May 1998.

[112] Julian S. Taurozzi, Vincent A. Hackley, and Mark R. Wiesner. A standardised approach for the dispersion of titanium dioxide nanoparticles in biological media. *Nanotoxicology*, 7(4):389–401, March 2012.

[113] Komkrit Suttiponparnit, Jingkun Jiang, Manoranjan Sahu, Sirikalaya Suvachittanont, Tawatchai Charinpanitkul, and Pratim Biswas. Role of Surface Area, Primary Particle Size, and Crystal Phase on Titanium Dioxide Nanoparticle Dispersion Properties. *Nanoscale Research Letters*, 6(1):1–8, December 2011.

[114] Thomas Williams. *Thermal Imaging Cameras: Characteristics and Performance*. CRC Press, April 2009.

[115] GATS Inc. Blackbody Spectrum, October 2015. Accessed 10/03/2015.

[116] D Eisenberg and W Kauzmann. *The Structure and Properties of Water*. Oxford University Press, October 2005.

[117] Hind A. Al-Abadleh and V. H. Grassian. FT-IR Study of Water Adsorption on Aluminum Oxide Surfaces. *Langmuir*, 19(2):341–347, January 2003.

[118] Jerome Faist, Federico Capasso, Deborah L. Sivco, Carlo Sirtori, Albert L. Hutchinson, and Alfred Y. Cho. Quantum Cascade Laser. *Science*, 264(5158):553–556, April 1994.

[119] Jrme Faist. *Quantum Cascade Lasers*. Oxford University Press, March 2013.

[120] M. Razeghi. High-power high-wall plug efficiency mid-infrared quantum cascade lasers based on InP/GaInAs/InAlAs material system. volume 7230, pages 723011–723011–8, 2009.

[121] Barbara H. Stuart and David J. Ando. *Biological Applications of Infrared Spectroscopy*. John Wiley & Sons, August 1997.

[122] Shoko Yamada, Silvan Schmid, Tom Larsen, Ole Hansen, and Anja Boisen. Photothermal Infrared Spectroscopy of Airborne Samples with Mechanical String Resonators. *Analytical Chemistry*, 85(21):10531–10535, November 2013.

[123] James F. Shackelford and William Alexander. *CRC Materials Science and Engineering Handbook, Third Edition*. CRC Press, December 2000.

[124] N.M. Ravindra, S. Abedrabbo, Wei Chen, F.M. Tong, A.K. Nanda, and A.C. Speranza. Temperature-dependent emissivity of silicon-related materials and structures. *IEEE Transactions on Semiconductor Manufacturing*, 11(1):30–39, February 1998.

[125] Mo Li, H. X. Tang, and M. L. Roukes. Ultra-sensitive NEMS-based cantilevers for sensing, scanned probe and very high-frequency applications. *Nature Nanotechnology*, 2(2):114–120, February 2007.

[126] William S. Janna. *Engineering Heat Transfer, Second Edition*. CRC Press, December 1999.

[127] Zhibin Huang, Dongmei Zhu, Fa Lou, and Wancheng Zhou. An application of Au thin-film emissivity barrier on Ni alloy. *Applied Surface Science*, 255(5, Part 2):2619–2622, December 2008.

[128] Tom Larsen. *Micro-Mechanical Temperature Sensors*. PhD thesis, September 2012.

[129] J. G. E. Gardeniers, H. a. C. Tilmans, and C. C. G. Visser. LPCVD siliconrich silicon nitride films for applications in micromechanics, studied with statistical experimental design*. *Journal of Vacuum Science & Technology A*, 14(5):2879–2892, September 1996.

[130] Bela G. Liptak. *Instrument Engineers' Handbook, Fourth Edition, Volume One: Process Measurement and Analysis*. CRC Press, June 2003.

[131] Kailiang Ren, M.B. Pisani, Ping Kao, and S. Tadigadapa. Micromachined quartz resonator-based high performance thermal sensors. In *2010 IEEE Sensors*, pages 2197–2201, November 2010.

[132] William J. Riley. *Handbook of frequency stability analysis*. US Department of Commerce, National Institute of Standards and Technology, 2008.

[133] Walter Stockwell. Bias Stability Measurement: Allan Variance, 2004. http://www.moog-crossbow.com/Literature/Application_Notes_Papers/Gyro_Bias_Stability_Measurement_using_Allan_Variance.pdf [Accessed 2015-12-15].

[134] Seid Sadat, Yi Jie Chua, Woochul Lee, Yashar Ganjeh, Katsuo Kurabayashi, Edgar Meyhofer, and Pramod Reddy. Room temperature picowatt-resolution calorimetry. *Applied Physics Letters*, 99:043106–043106–3, 2011. 4.

[135] J. Varesi, J. Lai, T. Perazzo, Z. Shi, and A. Majumdar. Photothermal measurements at picowatt resolution using uncooled microoptomechanical sensors. *Applied physics letters*, 71:306–308, 1997. 3.

[136] D.H.B. Wicaksono, G. Pandraud, P.J. French, and F. Jutzi. Performance of miniaturized LPCVD-SiN-membrane-based 714 m infrared thermal detector: Analytical, modeling, and experimental study. pages 498–501. IEEE, 2008.

[137] Jianjun Guan, Kazuro L Fujimoto, Michael S Sacks, and William R Wagner. Preparation and characterization of highly porous, biodegradable polyurethane scaffolds for soft tissue applications. *Biomaterials*, 26:3961–3971, 2005. 18.

[138] Wendy Amass, Allan Amass, and Brian Tighe. A review of biodegradable polymers: uses, current developments in the synthesis and characterization of biodegradable polyesters, blends of biodegradable polymers and recent advances in biodegradation studies. *Polymer International*, 47:89–144, 1998. 2.

[139] Shinichi Igarashi, Akiko N. Itakura, Masaya Toda, Masahiro Kitajima, Liqiang Chu, Anye N. Chifen, Renate Frch, and Rdiger Berger. Swelling signals of polymer films measured by a combination of micromechanical cantilever sensor and surface plasmon resonance spectroscopy. *Sensors and Actuators B: Chemical*, 117(1):43–49, September 2006.

[140] Bryce J. Marquis, Sara A. Love, Katherine L. Braun, and Christy L. Haynes. Analytical methods to assess nanoparticle toxicity. *The Analyst*, 134(3):425, 2009.

[141] G. Roebben, K. Rasmussen, V. Kestens, T. P. J. Linsinger, H. Rauscher, H. Emons, and H. Stamm. Reference materials and representative test materials: the nanotechnology case. *Journal of Nanoparticle Research*, 15(3):1–13, March 2013.

[142] Kirsten Rasmussen, Jan Mast, and Pieter-Jan De Temmerman. *Titanium dioxide, NM-100, NM-101, NM-102, NM-103, NM-104, NM-105 Characterisation and physico-chemical properties*. EU Bookshop, 2014.

[143] Volker Nischwitz and Heidi Goenaga-Infante. Improved sample preparation and quality control for the characterisation of titanium dioxide

nanoparticles in sunscreens using flow field flow fractionation on-line with inductively coupled plasma mass spectrometry. *Journal of Analytical Atomic Spectrometry*, 27(7):1084, 2012.

[144] Ana M. Tavares, Henriqueta Louro, Susana Antunes, Stephanie Quarr, Sophie Simar, Pieter-Jan De Temmerman, Eveline Verleysen, Jan Mast, Keld A. Jensen, Hannu Norppa, Fabrice Nesslany, and Maria Joo Silva. Genotoxicity evaluation of nanosized titanium dioxide, synthetic amorphous silica and multi-walled carbon nanotubes in human lymphocytes. *Toxicology in Vitro*, 28(1):60–69, February 2014.

[145] E. Verleysen, P. J. De Temmerman, E. Van Doren, M. Abi Daoud Francisco, and J. Mast. Quantitative characterization of aggregated and agglomerated titanium dioxide nanomaterials by transmission electron microscopy. *Powder Technology*, 258:180–188, May 2014.

[146] Ida Pernicova and Mrta Korbonits. Metforminmode of action and clinical implications for diabetes and cancer. *Nature Reviews Endocrinology*, 10(3):143–156, March 2014.

[147] Graham Rena, Ewan R. Pearson, and Kei Sakamoto. Molecular mechanism of action of metformin: old or new insights? *Diabetologia*, 56(9):1898–1906, September 2013.

[148] Lisa Logie, Jean Harthill, Kashyap Patel, Sandra Bacon, D. Lee Hamilton, Katherine Macrae, Gordon McDougall, Huan-Huan Wang, Lin Xue, Hua Jiang, Kei Sakamoto, Alan R. Prescott, and Graham Rena. Cellular Responses to the Metal-Binding Properties of Metformin. *Diabetes*, 61(6):1423–1433, June 2012.

[149] Foziah A. Al-Saif and Moamen S. Refat. Synthesis, spectroscopic, and thermal investigation of transition and non-transition complexes of metformin as potential insulin-mimetic agents. *Journal of Thermal Analysis and Calorimetry*, 111(3):2079–2096, March 2013.

[150] P. V. Babykutty, C. P. Prabhakaran, R. Anantaraman, and C. G. R. Nair. Electronic and infrared spectra of biguanide complexes of the 3d-transition metals. *Journal of Inorganic and Nuclear Chemistry*, 36(12):3685–3688, December 1974.

[151] Rodica Olar, Mihaela Badea, and Dana Marinescu. Thermal study of some new Ni(II) and Cu(II) complexes with ligands derived from N,N-dimethylbiguanide as potential antimicrobials. *Journal of Thermal Analysis and Calorimetry*, 99(3):893–898, March 2010.

[152] Volker Bhler. *Polyvinylpyrrolidone Excipients for Pharmaceuticals: Povidone, Crospovidone and Copovidone*. Springer Science & Business Media, December 2005.

[153] Veeran Gowda Kadajji and Guru V. Betageri. Water Soluble Polymers for Pharmaceutical Applications. *Polymers*, 3(4):1972–2009, November 2011.

[154] Alexander V. Kabanov. Polymer genomics: An insight into pharmacology and toxicology of nanomedicines. *Advanced Drug Delivery Reviews*, 58(15):1597–1621, December 2006.

[155] Yuanzhe Piao, Andrew Burns, Jaeyun Kim, Ulrich Wiesner, and Taeghwan Hyeon. Designed Fabrication of Silica-Based Nanostructured Particle Systems for Nanomedicine Applications. *Advanced Functional Materials*, 18(23):3745–3758, December 2008.

[156] Cyrille Boyer, Michael R. Whittaker, Volga Bulmus, Jingquan Liu, and Thomas P. Davis. The design and utility of polymer-stabilized iron-oxide nanoparticles for nanomedicine applications. *NPG Asia Materials*, 2(1):23–30, January 2010.

[157] Seung Y. Yang, Incheol Ryu, Hwang Y. Kim, Jin K. Kim, Sung K. Jang, and Thomas P. Russell. Nanoporous membranes with ultrahigh selectivity and flux for the filtration of viruses. *Advanced materials*, 18(6):709–712, 2006.

[158] Elizabeth A. Jackson. Nanoporous Membranes Derived from Block Copolymers: From Drug Delivery to Water Filtration. *Acs Nano*, 4(7):3548–3553, 2010.

[159] Jinyou Lin. Nanoporous polystyrene fibers for oil spill cleanup. *Marine Pollution Bulletin*, 64(2):347–352, 2012.

[160] B. A. Nelson and W. P. King. Measuring material softening with nanoscale spatial resolution using heated silicon probes. *Review of Scientific Instruments*, 78(2):023702, February 2007.

[161] F. Haaf, A. Sanner, and F. Straub. Polymers of N-Vinylpyrrolidone: Synthesis, Characterization and Uses. *Polymer Journal*, 17(1):143–152, January 1985.

[162] Brian C. Smith. *Infrared Spectral Interpretation: A Systematic Approach*. CRC Press, December 1998.

[163] Wee Tee Tan, M. M. Radhi, M. Z. Ab Rahman, and A. B. Kassim. Synthesis and characterization of grafted polystyrene with acrylonitrile using gamma-irradiation. *J Appl Sci*, 10:139–144, 2010.

[164] Mohammad Ahmed-Fouad Basha. Magnetic and optical studies on polyvinylpyrrolidone thin films doped with rare earth metal salts. *Polymer Journal*, 42(9):728–734, September 2010.

[165] A. Slistan-Grijalva, R. Herrera-Urbina, J. F. Rivas-Silva, M. valos Borja, F. F. Castilln-Barraza, and A. Posada-Amarillas. Synthesis of silver nanoparticles in a polyvinylpyrrolidone (PVP) paste, and their optical properties in a film and in ethylene glycol. *Materials Research Bulletin*, 43(1):90–96, January 2008.

[166] Chong Peng, Zhiyao Hou, Cuimiao Zhang, Guogang Li, Hongzhou Lian, Ziyong Cheng, and Jun Lin. Synthesis and luminescent properties of CaTiO_3: Prˆ3+ microfibers prepared by electrospinning method. *Optics Express*, 18(7):7543, March 2010.

[167] Hongshui Wang, Xueliang Qiao, Jianguo Chen, Xiaojian Wang, and Shiyuan Ding. Mechanisms of PVP in the preparation of silver nanoparticles. *Materials Chemistry and Physics*, 94(23):449–453, December 2005.

[168] Peter Repik, Stefan Erhardt, Graham Rena, and Martin J. Paterson. Biomolecular Mode of Action of Metformin in Relation to Its Copper Binding Properties. *Biochemistry*, 53(4):787–795, February 2014.

[169] Yeon Seok Kim. Electrochemical detection of 17 beta-estradiol using DNA aptamer immobilized gold electrode chip. *Biosensors and Bioelectronics*, 22(11):2525–2531, 2007.

[170] Omar A. Alsager. Small molecule detection in solution via the size contraction response of aptamer functionalized nanoparticles. *Biosensors and Bioelectronics*, 57(1):262–268, 2014.

[171] Omar A. Alsager, Shalen Kumar, Bicheng Zhu, Jadranka Travas-Sejdic, Kenneth P. McNatty, and Justin M. Hodgkiss. Ultrasensitive Colorimetric Detection of 17-Estradiol: The Effect of Shortening DNA Aptamer Sequences. *Analytical Chemistry*, 87(8):4201–4209, April 2015.

[172] Kasper Bayer Frhling. *Development of a SERS aptasensor for detection of medical residues*. PhD thesis, DTU Nanotech, 2015.

[173] J. A. Taboury, J. Liquier, and E. Taillandier. Characterization of DNA structures by infrared spectroscopy: double helical forms of poly(dG-dC)poly(dG-dC), poly(dD8g-dC)poly(dD8g-dC), and poly(dG-dm5c)poly(dG-dm5c). *Canadian Journal of Chemistry*, 63(7):1904–1909, July 1985.

[174] Nicholas L. Mills, Hkan Trnqvist, Simon D. Robinson, Manuel Gonzalez, Kareen Darnley, William MacNee, Nicholas A. Boon, Ken Donaldson, Anders Blomberg, Thomas Sandstrom, and David E. Newby. Diesel Exhaust Inhalation Causes Vascular Dysfunction and Impaired

Endogenous Fibrinolysis. *Circulation*, 112(25):3930–3936, December 2005.

[175] Nicholas L. Mills, Hkan Trnqvist, Manuel C. Gonzalez, Elen Vink, Simon D. Robinson, Stefan Sderberg, Nicholas A. Boon, Ken Donaldson, Thomas Sandstrm, Anders Blomberg, and David E. Newby. Ischemic and Thrombotic Effects of Dilute Diesel-Exhaust Inhalation in Men with Coronary Heart Disease. *New England Journal of Medicine*, 357(11):1075–1082, September 2007.

[176] U. Mathis. TEM analysis of volatile nanoparticles from particle trap equipped diesel and direct-injection spark-ignition vehicles. *Atmospheric Environment*, 38(26):4347–4355, 2004.

[177] J. Schneider, N. Hock, S. Weimer, S. Borrmann, U. Kirchner, R. Vogt, and V. Scheer. Nucleation Particles in Diesel Exhaust: Composition Inferred from In Situ Mass Spectrometric Analysis. *Environmental Science & Technology*, 39(16):6153–6161, August 2005.

[178] N. K. Meyer and Z. D. Ristovski. Ternary Nucleation as a Mechanism for the Production of Diesel Nanoparticles: Experimental Analysis of the Volatile and Hygroscopic Properties of Diesel Exhaust Using the Volatilization and Humidification Tandem Differential Mobility Analyzer. *Environmental Science & Technology*, 41(21):7309–7314, November 2007.

[179] S. Kureti. Simultaneous conversion of nitrogen oxides and soot into nitrogen and carbon dioxide over iron containing oxide catalysts in diesel exhaust gas. *Applied Catalysis B-environmental*, 43(3):281–291, 2003.

[180] T. S. Biswas, N. Miriyala, C. Doolin, X. Liu, T. Thundat, and J. P. Davis. Femtogram-Scale Photothermal Spectroscopy of Explosive Molecules on Nanostrings. *Analytical Chemistry*, 86(22):11368–11372, November 2014.

Appendix A

Detailed Fabrication Process Sequences

Process:	Pt electrode fabrication	**Affiliation:**	Nanotech / NSE / Nanoprobes
Rev. No.:	Ver. 02	**Batch no.:**	syam-Pt electrode
Date:	2010/09/06	**Substrate:**	Singleside polished 4" Si wafer
Author:	Shoko Yamada		

	Step	Process	Equipment	Recipe / Parameters
Nitride deposition	1	SiN Deposition	SiN LPCVD Furnace	LOWSTR / ~280nm/hour
	2	Inspection	Filmtek	
Electrode mask transfer	3	HMDS	HMDS Oven	Reciple 4 / normal
	4	Spin-coating photoresist	Track 1	PR2_2/2.2um
	5	Mask Exposure	KS Aligner	Hard contact / Exp. Time: 6s
	6	Reversal Bake	Track 1 or Gernardt oven	REV_120S / 120C for 120s
	7	Flood Exposure	KS Aligner	Lamp Test for 35s
	8	Photoresist Development	Developer 1 or 2	Dev. Time: 70s
	9	Inspection	Optical microscope	
Electrode metal deposition	10	Metal Deposition	Alcatel	Ti 10nm, Pt 50nm
	11	Lift Off	Lift Off wet bench	15 minutes with sonication
	12	Inspection	Optical microscope	
Passivation coating	13	SiN Deposition	PECVD3	mfsinls/standard /~12nm/min
Contact hole mask transfer	14	HMDS	HMDS Oven	Reciple 4 / normal
	15	Spin-coating photoresist	Track 1	PR2_2/2.2um
	16	2nd Mask Exposure	KS Aligner	Soft contact / Exp. Time: 6s
	17	Reversal Bake	Track 1	REV_120S / 120C for 120s
	18	Flood Exposure	KS Aligner	Lamp Test for 30s
	19	Photoresist Development	Developer 1 or 2	Dev. Time: 70s
	20	Inspection	Optical microscope	
Contact hole etching	21	SiO2/SiN Etching	RIE2	BGE-Nitr, 10min
	22	Photoresist Removal	Plasma Asher 1	1mbar, O_2=420ml/min, N_2=50ml/min, 1000W, 20min
	23	Inspection	Optical microscope	
Back end & finalization	24	Dicing wafer	Saw	Dicing Si wafer

NOTES: 32 chips / wafer

Figure A.1: Detailed process sequence for the fabrication of Pt chip working electrodes.

Process:	Al strings	**Group:**	Nanotech/NSE/Nanoprobes
Author:	Shoko Yamada	**Batch no.:**	syam-Al strings
Rev. No.:	Ver. 1.1	**Substrate:**	Silicon <100>, Double side
Date:	2011-11-09	polished 4" wafer with a thickness of 350 µm	

Process	Step	Description	Equipment	Parameters/ Recipe	Target
Nitride deposition	1	Silicon rich nitride	LPCVD Nitride	lowstr, 60 min * 2 rounds	550 nm
	2	Inspection	Filmtek		550 nm
KOH etch mask transfer	3	HMDS	HMDS oven	Recipe 4 (normal)	
	4	Spin-coating and baking	SSE spinner	PR2_2	2.2 um
	5	Exposure	KS aligner	7 sec	
	6	Developing	Developer bath	70 sec	
	7	Inspection	Opt microscope		
Hole etching	8	Nitride etch	RIE1	BGE-NITR, Time: 20 min	550 nm
	9	Resist removal	Acetone		
	10	Inspection	Dektak		
	11	KOH etch	KOH2 or KOH3	KOH 28 wt% 80ºC Time: 4 h 30 min	350 µm
	12	Cleaning	7 up thank	Time: 10 min	
Al deposition	13	Al deposition	Wordentec	10 Å/s, 1m40s	100 nm
Al strings mask transfer	14	HMDS	HMDS oven	Recipe 4 (normal)	
	15	Spin-coating	KS spinner	Danchip2_2_4"	2.2 um
	16	Baking	90'C hotplate	60 sec	
	17	Exposure	KS aligner	7 sec	
	18	Developing	Developer bath	110 sec	
	19	Inspection	Opt microscope		
String etching	20	Protection	Wax glue and dummy wafer	Hotplate	
	21	Al etch	ICP metal etcher	syam_Al 30 sec	100 nm
	22	Resist removal	ICP metal etcher	Prstrip 10 min	2.2 um
	23	Inspection	Opt microscope		
	24	Protection removal	Hotplate		
	25	Protection cleaning	Water		
Al annealing	26	Al annealing	Oven 250'C	3 h	
Membrane etching	27	Protection	KS spinner	Danchip1.5um_4"	1.5 um
	28	Baking	90'C hotplate	60 sec	
	29	Nitride Etch	RIE2	BGE-NITR, Time: 30 min	550 nm
	30	Protection removal	Acetone		
	31	Inspection	Opt microscope		
	32	Inspection	Dektak	Measure Al thickness	100 nm

Note: 60 chips from one wafer
Metal coverage is approx. 1 %

Figure A.2: Detailed process sequence for the fabrication of Al strings.

Process:	Low stress SiN strings	Group:	Nanotech/Nanoprobes
Author:	Shoko Yamada	Substrate:	silicon <100>, Double side
Version:	1.1	polished 4" wafer with a thickness of 350µm	

Process	Step	Description	Side	Equipment	Parameters	Target
LPCVD nitride deposition	1	Low stress SiN (SRN)		LPCVD nitride	LOWSTR, 35 min	185 um
	2	Inspection		Ellipsometer		
SiN strings mask transfer	3	HMDS		HMDS oven	Recipe 4 (normal)	
	4	Spin-coating & baking	front	SSE spinner	1.5 um	
	5	Exposure	front	KS aligner	7 sec	
	6	Developing		Developer bath	60 sec	
	7	Inspection		Optical microscope		
String Etch	8	Nitride Etch	front	RIE1	oh_polya, 7 min	185 nm
	9	PR strip		Acetone		
	10	Oxygen Plasma		Plamsa asher	O2: 500 ml, N2: 50 ml, 1000W, 15 min	
Protective SiN	11	PECVD	front	PECVD 3	mfsinls, 38 min	410 nm
KOH etch mask transfer	12	HMDS		HMDS oven	Recipe 4 (normal)	
	13	Spin-coating & baking	back	SSE spinner	1.5 um	
	14	Exposure	back	KS aligner	7 sec	
	15	Developing		Developer bath	55 sec	
	16	Inspection		Optical microscope		
Hole etch	17	Nitride Etch	back	RIE2	oh_polya, 7 min	185 nm
	18	PR strip		Acetone		
	19	Oxygen Plasma		Plamsa asher	O2: 500 ml, N2: 50 ml, 1000W, 15 min	
	20	KOH etch		KOH2 or KOH3	KOH 28 wt% 80ºC Time: 4 h 30 min	all the way
Protective SiN removal	21	BHF		BHF	13 min	
Dry	22	Ethanol bath			70C, 10 min	
Au deposition	23	Au & Ti deposition	front	Wordentec	Ti 10 nm, Au 20 nm	

Figure A.3: Detailed process sequence for the fabrication of low stress silicon nitride strings with a gold coating.

Process:	High stress SiN strings	Group:	Nanotech/Nanoprobes
Author:	Shoko Yamada	Substrate:	silicon <100>, Double side
Version:	1.1	polished 4" wafer with a thickness of 350µm	

Process	Step	Description	Side	Equipment	Parameters	Target
LPCVD nitride deposition	1	High stress SiN		LPCVD nitride new 6"	4NITDAN, 27-32 min	80 nm
	2	Inspection		Ellipsometer		
SiN strings mask transfer	3	HMDS		HMDS oven	Recipe 4 (normal)	
	4	Spin-coating & baking	front	SSE spinner	1.5 um	
	5	Exposure	front	KS aligner	7 sec	
	6	Developing		Developer bath	60 sec	
	7	Inspection		Optical microscope		
String Etch	8	Nitride Etch	front	RIE1	oh_polya, 3 min	80 nm
	9	PR strip		Acetone		
	10	Oxygen Plasma		Plamsa asher	O2: 500 ml, N2: 50 ml, 1000W, 15 min	
Protective SiN	11	PECVD	front	PECVD 3	mfsinls, 38 min	410 nm
KOH etch mask transfer	12	HMDS		HMDS oven	Recipe 4 (normal)	
	13	Spin-coating & baking	back	SSE spinner	1.5 um	
	14	Exposure	back	KS aligner	7 sec	
	15	Developing		Developer bath	55 sec	
	16	Inspection		Optical microscope		
Hole etch	17	Nitride Etch	back	RIE2	oh_polya, 3 min	80 nm
	18	PR strip		Acetone		
	19	Oxygen Plasma		Plamsa asher	O2: 500 ml, N2: 50 ml, 1000W, 15 min	
	20	KOH etch		KOH2 or KOH3	KOH 28 wt% 80ºC Time: 4 h 30 min	all the way
Protective SiN removal	21	BHF		BHF	13 min	
Dry	22	Ethanol bath			70C, 10 min	

Figure A.4: Detailed process sequence for the fabrication of high stress silicon nitride strings.

Appendix B

Dimensions of Vacuum Chamber

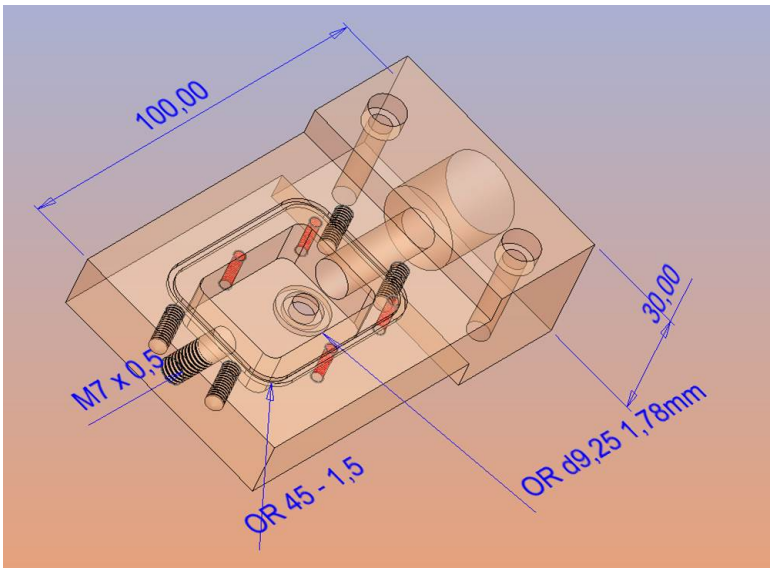

Figure B.1: Dimensions of vacuum chamber (*units in mm*).

Appendix C

Matlab Script for Allan Deviation

The Matlab script used to calculate the Allan deviation of frequency versus time data has been provided by Luis Guillermo Villanueva Torrijo and it is given below.

```
function [tau, allandev] = AllanDev(data)
time=(data(:,1)-data(1,1));
f=data(:,2);
f0=mean(f);
df=f-f0;
Ts=mean(diff(time));
t=[0:Ts:(length(f)-1)*Ts];

H=2*pi*tf([1],[1 0]);
dphi=lsim(H,f,t);

x=dphi/(2*pi*f0);

tau=Ts*[1:floor(length(x))];
sigmay_2=zeros(1,length(tau));

for ii=1:1:length(tau)
    xtemp=x(1:round(tau(ii)/Ts):length(x));
    ybar=diff(xtemp)/tau(ii);
    for j=1:length(ybar)-1
        sigmay_2(ii)=sigmay_2(ii)+(ybar(j+1)-ybar(j))^2;
    end
    sigmay_2(ii)=1/2*1/(length(ybar)-1)*sigmay_2(ii);
end

allandev=sqrt(sigmay_2);

data2(:,1)=tau;
data2(:,2)=allandev;
```

```
30
31 DS=dataset(data2);
32 filename='Allan_Dev.dat';
33 export(DS,'file',filename,'Delimiter','tab','WriteVarNames',false);
```

Appendix D

Matlab Script for Spectra Extraction

The Matlab script used to extract an IR spectrum from raw measurement data when using the thermal IR source has been downloaded from mathworks.com and it is given below.

```
% Find upper and lower envelopes of a given signal
% The idea is from Envelope1.1 by Lei Wang, but here it works ...
    well when the signal contains
% successive equal samples and also includes first and last ...
    samples of the signal in the envelopes.
% inputs:
%   sig: vector of input signal
%   method: method of interpolation (defined as in interp1)
% outputs:
%   upperenv: upper envelope of the input signal
%   lowerenv: lower envelope of the input signal
function [upperenv] = getUpperEnvelope(sig, method)
if nargin == 1
    method = 'linear';
end
upperind = find(diff(sign(diff(sig))) < 0) + 1;
lowerind = find(diff(sign(diff(sig))) > 0) + 1;
f = 1;
l = length(sig);
try
    upperind = [f upperind l];
    lowerind = [f lowerind l];
catch
    upperind = [f; upperind; l];
    lowerind = [f; lowerind; l];
end
xi = f : l;
upperenv = interp1(upperind, sig(upperind), xi, method, 'extrap');
lowerenv = interp1(lowerind, sig(lowerind), xi, method, 'extrap');
```

Appendix D

The Matlab script used to extract an IR spectrum from raw measurement data when using the QCL has been written by Silvan Schmid and it is given below.

```
function [spectrum] = extractDiffEnvelope(pFileNameFreq, ...
    pFreqDataCol, pWavenumberStart, pWavenumberStop, ...
    pWavenumberResolution, pParam1, pParam2, pParam3)
if ischar(pFileNameFreq)
    freqData = csvread(pFileNameFreq);
else
    freqData = pFileNameFreq;
end

freqList = [];

if exist('pParam1') && exist('pParam2')
    if ischar(pParam1)
        syncData = csvread(pParam1);
        figure; plot(syncData(:,1),syncData(:,pParam2));

        syncTriggerLevel = 0.5*median(syncData(:,pParam2));

        syncList = [];
        flag = 0;

        if exist('pParam3')

            for i = 1:length(syncData)
                if (syncData(i,pParam2) < syncTriggerLevel) && ...
                    (flag == 0)
                    fragmentStart = i;
                    flag = 1;
                elseif (syncData(i,pParam2) > ...
                    syncTriggerLevel) && (flag == 1)
                    fragmentStop = i;
                    flag = 0;
                    syncFragment = [fragmentStart fragmentStop];
                    syncList = [syncList ; syncFragment];
                end
            end

        else

            for i = 1:length(syncData)
                if (syncData(i,pParam2) > syncTriggerLevel) && ...
                    (flag == 0)
                    fragmentStart = i;
                    flag = 1;
                elseif (syncData(i,pParam2) < ...
                    syncTriggerLevel) && (flag == 1)
                    fragmentStop = i;
                    flag = 0;
```

```
43                      syncFragment = [fragmentStart fragmentStop];
44                      syncList = [syncList ; syncFragment];
45                  end
46              end
47          end
48          pFreqStart = syncList(1,1);
49          pFreqStop = syncList(length(syncList),2);
50
51          pFreqStartTime = syncData(pFreqStart,1);
52          pFreqStopTime = syncData(pFreqStop,1);
53          [c pFreqStart] = min(abs(freqData(:,1) - pFreqStartTime))
54          [c pFreqStop] = min(abs(freqData(:,1) - pFreqStopTime))
55
56          freqList = freqData(pFreqStart:pFreqStop,pFreqDataCol);
57  figure; plot(freqData(:,1),freqData(:,pFreqDataCol),freqData...
58  (pFreqStart:pFreqStop,1),freqData(pFreqStart:pFreqStop,...
59  pFreqDataCol));
60
61      elseif pParam1 <= length(freqData) && pParam2 > pParam1
62       freqList = freqData(pParam1:pParam2,pFreqDataCol);
63  figure; ...
        plot(1:length(freqData),freqData(:,pFreqDataCol),pParam1:...
64  pParam2,freqData(pParam1:pParam2,pFreqDataCol));
65      end
66
67  else
68      freqList = freqData(:,pFreqDataCol);
69      figure; plot(freqData(:,1),freqData(:,pFreqDataCol));
70  end
71
72  deltaWavenumber = ...
        (pWavenumberStop-pWavenumberStart)/length(freqList);
73  for i = 1:length(freqList)
74      freqList(i,2) = pWavenumberStart + (i-1)*deltaWavenumber + ...
            deltaWavenumber/2;
75  end
76
77  if pWavenumberResolution == 0
78      minPeakdistance = 1;
79  else
80      numberOfPoints = ...
            (pWavenumberStop-pWavenumberStart)/pWavenumberResolution;
81      minPeakdistance = int64(length(freqList)/numberOfPoints);
82  end
83
84  [maxima,maxIndx] = findpeaks(freqList(:,1),'MINPEAKDISTANCE', ...
        minPeakdistance);
85  maxList = freqList(maxIndx,1)
86
87  freqListInv = 1.01*max(freqList(:,1)) - freqList(:,1);
88  [minima,minIndx] = findpeaks(freqListInv,'MINPEAKDISTANCE', ...
        minPeakdistance);
89  minList = freqList(minIndx,1);
90
```

```
91 spectrum = [];
92 maxListScaled = interpft(maxList,length(minList))
93 for i = 1:length(minList)
94     diffFreq = maxListScaled(i) - minList(i);
95     wavenumber = freqList(minIndx(i),2);
96     spectrumPoint = [wavenumber diffFreq];
97     spectrum = [spectrum ; spectrumPoint];
98 end
99 figure; plot(spectrum(:,1),spectrum(:,2));
```

Appendix E

Matlab Script for Power Normalization

The Matlab script used to normalize a spectrum with respect to IR power of the QCL has been written by Silvan Schmid and it is given below.

```
1  function [spectrum] = powerNormalize(pSpectrum)
2
3  powerSpectrum = csvread('power.csv');
4  startScan = 925;
5  stopScan = 1922;
6
7  powerSpectrumN(:,2) = powerSpectrum(:,2)./max(powerSpectrum(:,2));
8
9  startX = powerSpectrum(1,1);
10 stopX = powerSpectrum(length(powerSpectrum),1);
11 resolution = (stopX-startX)/10000;
12
13 interPolPower(:,1) = startX:resolution:stopX;
14 interPolPower(:,2) = ...
       interp1(powerSpectrum(:,1),powerSpectrumN(:,2),...
15 interPolPower(:,1));
16
17 startWavenumber = pSpectrum(1,1);
18 stopWavenumber = pSpectrum(length(pSpectrum),1);
19
20 startIndex = ...
       int64((startWavenumber-startScan)*length(interPolPower)/...
21 (stopScan-startScan));
22 stopIndex  = ...
       int64((stopWavenumber-startScan)*length(interPolPower)/...
23 (stopScan-startScan));
24
25 scaledPowerSpectrum = ...
       interpft(interPolPower(startIndex:stopIndex,2),...
26 length(pSpectrum(:,2)));
27
```

```
28 spectrumY = pSpectrum(:,2)./scaledPowerSpectrum;
29 spectrum = [pSpectrum(:,1) spectrumY];
30
31 figure; plot(spectrum(:,1),spectrum(:,2));
```

Appendix F

Protocol for Estradiol Thiol-Aptamer Functionalisation

The chemicals and protocol used to functionalise gold-coated strings with estradiol thiol-aptamer have been written by Kasper Bayer Frhling and it is given below.

Chemicals

Aptamer: 5-Thiol-C6 S-S-ATACGAGCTTGTTCAATACGAAGGGAT-GCCGTTTGGGCCCAAGTTCGGCATAGTGTGGTGATAGTAAGA-GCAATC-3 75-mer, 23 kDa

Target: 17-estradiol (100 nM, 1 μM in binding buffer)

Substrate: Gold-coated strings

Binding buffer: 2 mM TrisHCl (0.24 mg/ml), 10 mM NaCl (0.58 mg/ml), 0.5 mM KCl (0.037 mg/ml), 0.2 mM $MgCl_2$ (0.019 mg/ml), 0.1 mM $CaCl_2$ (0.011 mg/ml), 5% ethanol

Disulphide reduction: TCEPHCl in pure H_2O. The concentration should at least be 100 times of the aptamer.

Denaturation buffer: 2 M UREA + 7.5 mM EDTA in pure H_2O

Blocking: 10 mM 6-mercapto-1-hexanol (MCH) in pure H_2O

Protocol

Aptamer pre-treatment

1. Prepare 100 µl 5 µM solution of the 5-disulphide modified aptamer in pure water.
2. Prepare 500 µM (143 µg/ml) solution of TCEPHCl in pure H_2O.
3. Mix 100 µl TCEP solution into the aptamer solution and incubate for 60 minutes at room temperature.
4. Add 100 µl 1xPBS immediately before the immersion of the substrate. The final concentration of aptamer is 1.66 µM.

Aptamer functionalisation

1. Immerse the substrate into ethanol for 3 minutes (no vortex).
2. Immerse the substrate into pure water for 3 minutes (no vortex).
3. Immerse the substrate into the aptamer solution.
4. Incubate for 3 hours at room temperature.

Hormone binding

1. Transfer the substrate directly to the MCH solution without washing and incubate for 1 hour at room temperature.
2. Immerse into pure water for 3 minutes (no vortex).
3. Immerse in UREA + EDTA solution for 3 minutes (no vortex) to unfold/denature the aptamer.
4. Immerse into pure water for 3 minutes (no vortex).
5. Prepare estradiol solution in binding buffer (remember to adjust to 5% ethanol).
6. Immerse the substrate into the solution and incubate at room temperature for 1 hour (no vortex).
7. Transfer directly to pure binding buffer for 15 minutes to remove unbound molecules.
8. Dip quickly in pure water for 2 seconds to prevent salt aggregation (no vortex).

Appendix G

Projects Supervised

Title: COMSOL Analysis of Influence of Metal Layers on Silicon Nitride Microstrings
Participants: Paul Morin, Theofanis Spanos
Study level: MSc

Title: Strings for Biosensing Applications
Participants: Hasting Cele, Matthew Capener, Shoko Yamada, Supannee Learkthanakhachon
Study level: PhD

Appendix H

Publications

The following publications were achieved during the PhD project.

1. **Shoko Yamada**, Silvan Schmid and Anja Boisen. Stability of Au and Pt working electrodes and Ag/AgCl reference electrodes in Gambles solution for engineered nanoparticles toxicity characterization. *Conference on Electrochemical Science and Technology*, Kgs. Lyngby, Denmark, 30 September and 1 October 2010. Poster presentation.

2. **Shoko Yamada**, Silvan Schmid and Anja Boisen. MEMS-based aerosol composition sensor. *International Congress on Safety of Engineered Nanoparticles and Nanotechnologies*, Helsinki, Finland, 28-31 October 2012. Poster presentation.

3. **Shoko Yamada**, Silvan Schmid and Anja Boisen. Photothermal IR spectroscopy of picogram samples with microstring resonator. *NMC 2013: 10th International Workshop on Nanomechanical Sensing*, Stanford, US, 1-3 May 2013. Oral presentation.

4. **Shoko Yamada**, Tom Larsen, Silvan Schmid and Anja Boisen. Photothermal IR spectroscopy of picogram samples with microstring resonator. *Transducers 2013 - 17th International Conference on Solid-State Sensors, Actuators and Microsystems*, Barcelona, Spain, 16-20 June 2013. Oral presentation.

5. **Shoko Yamada**, Silvan Schmid, Tom Larsen, Ole Hansen, and Anja Boisen. Photothermal infrared spectroscopy of airborne samples with mechanical string resonators. *Analytical Chemistry*, 85(21):10531-10535, November 2013.

6. Alina Andersen, Pramod Ek, Thomas Andresen, **Shoko Yamada**, Anja Boisen, Silvan Schmid. Nanomechanical IR Spectroscopy for the fast analysis of picogram samples of engineered nanomaterials. *18th*

International Conference on Miniaturized Systems for Chemistry and Life Sciences, San Antonio, US, 26-30 October 2014.

7. Alina Andersen*, **Shoko Yamada***, Pramod Kumar E. K., Thomas L. Andresen, Anja Boisen and Silvan Schmid. Nanomechanical IR spectroscopy for fast analysis of liquid-dispersed engineered nanomaterials. *Sensors & Actuators B: Chemical*, In press. * Contributed equally.

The following patent application has been filed based on the methods described in Sections 6.2 and 6.3 and results described in Sections 7.3.1 and 7.3.3.

1. **S. Yamada**, T. Larsen, S. Schmid and A. Boisen. Photothermal Resonance Spectroscopy for Aerosol Composition Analysis. Publication numbers: WO2014063712A1, EP2912435A1, and US20150293017, Filing date: 25 October, 2013, Publication date: 1 May, 2014.

Appendix I

Paper I: Photothermal Infrared Spectroscopy of Airborne Samples with Mechanical String Resonators

http://pubs.acs.org/doi/abs/10.1021/ac402585e

Appendix J

Paper II: Nanomechanical IR Spectroscopy for Fast Analysis of Liquid-Dispersed Engineered Nanomaterials

http://www.sciencedirect.com/science/article/pii/S0925400516304658

Published by:
DTU Nanotech
Department of Micro- and Nanotechnology
Technical University of Denmark
Ørsteds Plads, building 345C
DK-2800 Kgs. Lyngby

DTU Nanotech
Department of Micro- and Nanotechnology